DRIFT WAVE STUDIES IN A LINEAR

MULTIPLE MIRROR

BY

MICHAEL ANTHONY MAKOWSKI

A thesis submitted in partial fulfillment of the

requirements for the degree of

DOCTOR OF PHILOSOPHY

(Nuclear Engineering)

at the

UNIVERSITY OF WISCONSIN-MADISON

1983

DRIFT WAVE STUDIES IN A LINEAR MULTIPLE MIRROR

Michael A. Makowski

Under the supervision of Professor Gilbert A. Emmert.

A drift wave is observed at low magnetic field strengths in a linear multiple mirror, a steady state plasma device. It is characterized by a frequency which decreases with increasing magnetic field stength, propagation in the direction of the electron diamagnetic current, and an azimuthal mode number of 2. The mode is observed under the condition that the ion cyclotron frequency is less than the ion diamagnetic freqeuncy ($\Omega_i < \omega_{*i}$). The frequency is Doppler shifted by an ExB drift.

Effects of particles trapped in the mirror cells alter the characteristics of the instability. The frequency decreases slightly with increasing mirror ratio and the fluctuation level increases with increasing mirror ratio for M = mirror ratio $\leq$ 1.1, but then levels off at higher mirror ratios.

The drift wave is modeled by a linear kinetic theory which treats finite ion gyroradius, collisions, an electron temperature gradient, and trapped electrons. The theory predicts three unstable modes, only one of which is consistent with all of the above measurements. This instability is a Doppler shifted drift cyclotron instability modified by trapped particle effects.

ACKNOWLEDGEMENTS

I would like to thank Professor Gilbert A. Emmert for his support and guidance throughout the course of this research. His freely given time and advice have been greatly apprciated.

More than special thanks goés to my wife, Betty, for her continued support and encouragement. Without her, this persuit would have been impossible.

To Cliff Strawitch goes thanks for introducing me to the ins and outs of the DC Lab and for his special wit as an officemate. Evan Rose is thanked for many thought provoking discussions. Philip Smith is thanked for many discussions and his constructive criticism of what has become the "droop method."

Professor S.C. Prager is thanked for his continued interest and support in this project. Thanks goes to Professor Hershkowitz for discussions with him on emissive probes.

Finally, thanks must be given to Tom Lovell and Kay Shatrawka, two people who keep the plasma labs going on a day to day basis.

This work was supported by the National Science Foundation.

DEDICATION

This thesis is dedicated to my wife, Betty, and my two children, Margaret and Martha.

TABLE OF CONTENTS

	Page
ABSTRACT	ii
ACKNOWLEDGEMENTS	iii
DEDICATION	iv
TABLE OF CONTENTS	v
I. INTRODUCTION	1
A. Drift Waves	1
B. Drift Cyclotron Instability	3
C. Trapped Particle Instabilities	5
1. History	5
2. Experimental Observations of the Trapped Particle Instability	9
D. Thesis Organization	12
II. APPARATUS	18
A. Magnetic Coils and Power Supplies	18
B. Plasma Source and End Plate	29
C. Vacuum System	36
III. DIAGNOSTICS	40
A. Cold Langmuir Probes	40
B. Emissive Probes	44
1. Theory	45
2. Experiment	62
3. Discussion	69

IV. BASIC THEORY	72
A. Generalized Response for Ions and Circulating Electrons	72
B. Ion Response	80
C. Circulating Electron Response	81
D. Trapped Electron Response	81
E. Trapped Electron Dispersion Relation	88
F. Instabilities Predicted from Theory	92
V. DRIFT CYCLOTRON INSTABILITY	102
A. Introduction and Motivation	102
B. Simplified Theory of the Drift Cyclotron Instability	109
C. Experimental Results	124
1. Uniform Field Results	124
a. Experimental Observations	124
b. Comparison of Experiment to Theory	138
2. Trapped Particle Effects	143
D. Discussion and Conclusions	152
VI. OTHER OBSERVATIONS	157
A. Observation of Drift Waves	158
1. Trapped Electron Drift Wave	158
2. Dissipative Drift Wave	160
B. Observations of the Low Frequency Mode	169
C. Conclusions	185
APPENDIX — NUMERICAL SOLUTION OF THE DISPERSION RELATION	188

I. INTRODUCTION

A. Drift Waves

Drift waves are of interest and importance for several reasons. This is primarily because all laboratory plasmas have spatial gradients of one or more of density, temperature, magnetic field, and electric field. Each of these gives rise to particle drifts which potentially can couple the energy in the drift to a wave and cause instability.

In a word, particle confinement is the essential goal of a great deal of plasma physics. Much time and effort is devoted to the understanding of plasma instabilities in general because instability poses a threat to confinement. Instabilities arise in both of the essential descriptions of a plasma: fluid and kinetic. Of the two, fluid or MHD instabilities are the most serious because they can lead to a catastrophic loss of the whole plasma on a very short time scale. Once configurations are found which are MHD stable there remain the kinetic instabilities to contend with.

Drift waves fall into the category of kinetic instabilities. Although drift waves can be derived from some fluid theories an accurate calculation of the growth rate requires that a kinetic theory be used. For kinetic instabilities in general, confinement is degraded due to the enhanced transport of particles across field lines by the fluctuating fields of the wave. The enhanced transport

may be described by an effective diffusion coefficient which must be added to the other loss mechanisms in the plasma.

Drift waves arise from "kinetic" or particle considerations based on a microscopic description of the plasma, such as the Vlasov equation. (Fluid theory also predicts drift waves but they are always stable in this description.) The degradation of confinement at the microscopic level is in sharp contrast to that on the macroscopic level described by fluid or MHD theory. At the fluid level the stability of the plasma as a whole is at issue. Clearly, this is of more fundamental concern. Once gross stability has been achieved transport, and thus drift waves, becomes the predominant issue.

The theory of drift waves is extensive and well developed[1,2,3] and dates back to 1957.[4] The list of effects which influence drift wave stability is large and diverse and includes magnetic shear, collisions, the presence of trapped particles, plasma impurities, plasma current, particle gyroradius, magnetic field line curvature, and velocity space anisotropies. Most of the theory was developed in the early 1960's but the field still remains active even today.[5]

Experimental work on drift waves has always lagged behind its theoretical development. This is in part due to the difficulty in identifying one particular mode out of the numerous modes predicted by theory. Also, the experimental situation is often complicated by the simultaneous presence of two or more modes in the plasma. Finally, the instability is usually observed in a nonlinearly

saturated state which makes comparisons to linear drift wave theory difficult if not completely dubious at times.

Despite these drawbacks the fundamental physics of drift waves has been experimentally verified. The first systematic study of drift waves was done in Q-machines,[6,7] a linear device containing an alkali metal plasma in which $T_e = T_i = 0.2$ eV and $n = 10^9$-10^{11} cm^{-3}. Other pioneering work in toroidal devices was performed on multipoles[8] and stellarators.[9] Since this early work there have been numerous observations of many types of drift waves over a wide range of parameters.

B. Drift Cyclotron Instability

The drift cyclotron instability was discovered by A.B. Mikhailovskii and A.V. Timofeev.[10] It may be thought of as a coupling between a stable drift oscillation to a stable ion Bernstein mode[11] to yield an unstable oscillation near an ion cyclotron harmonic.[12] The condition for instability requires a "resonance" between the mode frequency, ω, and a multiple of the ion cyclotron frequency, $n\omega_{ci}$. The resonance condition has the added effect of producing rather small growth rates.

With respect to the present experiment the basic theory of Mikhailovskii and Timofeev[10] is relevant with only a few modifications. One feature inherent to the present experiment which was not treated in the above theory is the condition $T_e >> T_i$ but this is easily included in the analysis and causes no difficulties.

Collisions are not negligible in the present experiment and this effect was not included in the original analysis. However, collisions were the subject of a number of later papers.[3,13,14,15] The essential results are that the growth rates are reduced slightly but that instability occurs over a wider range of values of $k_\perp$, the perpendicular wave number. In general, ion-ion collisions are stabilizing. Since the growth rates associated with the drift cyclotron instability are small the induced transport from this instability should also be small. It might then be thought that the drift cyclotron instability is essentially harmless in comparison to most other instabilities. This is by and large true, but this picture is altered when there are velocity space anisotropies present.

Early on it was discovered by R.F. Post and M.N. Rosenbluth[16] that the velocity space anisotropy found in mirror machines provides a source of free energy for the drift cyclotron wave and this drives the mode strongly unstable. The new instablity is called the drift cyclotron loss cone (DCLC) mode. This instability provides strong incentive for studying the drift cyclotron instability.

Another area in which the drift cyclotron instability has surfaced is in the theory of anomalous transport in the late implosion phase of a pinch.[17,18] In addition, the theory of the drift cyclotron instability has been extended to include finite beta effects[17,19,20] and magnetic field line curvature effects.[21,22]

To our knowledge only one previous experimental observation of the drift cyclotron instability has been reported. This was by T. Ohkawa and M. Yoshikawa on the G.A. Octupole.[23] The nature of the device and the experimental parameters under which the instability was observed are significantly different from the present experiment. The octupole is a toroidal device in which magnetic curvature effects are important, in contrast to the present linear device in which the curvature effects can be eliminated. Also, the drift cyclotron instability was observed in the octupole under the condition that $T_e \ll T_i$ whereas the reverse is true ($T_e \gg T_i$) in the present device. The Linear Multiple Mirror thus provides an opportunity to study the drift cyclotron instability in a previously unexplored parameter regime and geometry.

C. Trapped Particle Instabilities

1. History

The trapped particle instabilities have a somewhat interesting history associated with them. The first trapped particle instability was predicted by B.B. Kadomstev[24] as a generalization to tokamaks of the interchange mode found in mirror machines. In tokamaks the "trapped particles" are localized to regions of bad curvature and provide the free energy to drive the instability. The circulating particles form a background dielectric which reduces the growth rate but are not completely stabilizing. Later it was found

that collisions strongly influenced the stability of the mode. Instabilities in which collisions played a role became known as dissipative trapped particle modes.[25] Next it was realized that trapped electrons alone were sufficient to destabilize a drift wave. Destabilization by trapped electrons requires both a temperature gradient and a velocity dependent collision frequency.[26,27] This instability is known as the dissipative trapped electron mode (DTEM).

When more sophisticated analyses (including the effects of magnetic shear, bounce resonances, etc.) of the trapped particle instabilities are performed for the tokamak geometry it is usually found that these devices are unstable to the trapped particle instabilities. Associated with the presence of the trapped particle instabilities is turbulent particle and energy transport above and beyond the neoclassical transport due simply to the presence of trapped particles without any instability. The anomalous transport for this mode can be quite large[28] and led to catastrophic predictions when scaled to future tokamaks and reactors. This spawned an intensive study of the trapped particle modes. Several review articles on the subject quickly appeared.[29]

Soon afterward the next generation of tokamaks was built and tested. These tokamaks operated in a parameter regime in which the DTEM was expected to be unstable. While anomalous electron transport was observed in all the devices, an instability which could be clearly identified as the DTEM was not observed. Instead

of a single mode a broad band spectrum of low level oscillations was observed in the vicinity of the drift frequency. This null result led to a decline in interest in trapped particle instabilities. Instead, theoretical attention turned to an explanation of the tubulent spectrum observed and trapped particle instabilities became only one of a number of possible candidates for the cause of the spectrum.[30] A positive identification of any trapped particle instability on a tokamak has yet to be made although a search was recently made on the TFR tokamak.[31] However, the trapped particle instabilities still remain a good candidate for the ultimate cause of the observed anomalous transport in tokamaks.[32,33]

After about an eight year lull interest in trapped particle modes has been renewed with the advent of the tandem mirror. In this device particles in the central cell are "insulated" from those in the end plugs; electrons are electrostatically confined while ions are confined magnetically by the mirror geometry. Gross MHD stability against ballooning and interchange modes is derived from the average good curvature of the system as a whole. The central cell has neutral curvature. There is a region of bad curvature in the transition from the central cell to the end plugs but the end plugs themselves are minimum-B configurations which provide the bulk of the good curvature required to stabilize the system. The "insulating" effect, while providing good particle confinement in the central cell, also has the effect of limiting communication of central cell particles with those in the end plugs. The central

cell particles never sample the good curvature provided by the end cells and in essence form a class of particles trapped in a region of unfavorable curvature. The result is that certain tandem mirror configurations can suffer from trapped particle instabilities with growth rates comparable to those of unstable MHD interchange modes.[34] This mode occupies a peculiar position in instability theory being somewhere in between a purely kinetic and purely MHD mode. These modes are quite different from those predicted for tokamaks. In tandem mirrors the modes are collisionless and driven by bad curvature. Also, in tandem mirrors there are parallel electric fields to contend with. In tokamaks the most important modes are collisional, the fraction of trapped particles is much smaller, and curvature is not the sole driving mechanism of the instability. It is rather ironic to note that an instability predicted for tokamaks by an analogy to mirror machines has come back to haunt mirror stability.

Overall, the theory of the trapped electron instability is extensive and quite well developed for tokamaks.[35] Even the two dimensional mode structure has been worked out for the toroidal geometry of tokamaks.[36,37,38] As mentioned above, the theory for the tandem mirror is still being developed.[34] Work on trapped particle instabilities has also been reported for the EBT device[39]. With the application of the theory of the trapped particle instability to so many different geometries it would seem that the book on this instability is far from closed.

2. Experimental Observations of the Trapped Particle Instability

Due to the basically simple physics behind the trapped electron mode a simple criteria for instability results, namely[25]

$$\omega_* \leq \nu_{eff} < \omega_{be}$$

where ω_* is the diamagnetic frequency, ν_{eff} is the effective collision frequency for the trapped particles, and ω_{be} is the bounce frequency of the particles trapped in the magnetic well. Experimentally this criteria is relatively easy to achieve. Although trapped electron instabilities are usually discussed in the context of tokamaks, a toroidal device, this type of geometry is not a necessary condition for the instability to occur (as demonstrated by the original derivation of the DTEM in cylindrical geometry by Kadomtsev and Pogutse[25]). Despite this only comparatively few reports of the experimental observation of this mode have been made, but these have been in a variety of different plasma devices (octupole, single cell mirror, and multi- mirror devices).

The earliest report is by Deschamps, Gravier, Renaud, and Samain[40] who in 1973 reported observations of the dissipative trapped electron mode (DTEM) in the ODE device. However, while the instability which they observed has many of the characteristics of the DTEM it was most unstable at $\omega_*/\nu_{eff} \sim 2\text{-}4$ rather than ≤ 0.1 as

predicted by theory. In addition the instability was observed for $\nu_{eff}/\omega_* \sim 0.03$, which put it well into the collisionless regime where one would not expect a dissipative instability.

A collisionless trapped particle mode was reported by Primmerman, Lidskey, and Politzer[41] at MIT. The instability is not excited by the collisional detrapping of electrons, but rather by a resonance between the bounce motion of the trapped electrons and the wave. This bounce resonance mode was theoretically predicted by Coppi[42].

Microwave scattering experiments were done in the FM-1 device and revealed drift-type waves when operated in the trapped electron regime[43]. While the operating parameters of the FM-1 device placed it in the trapped electron regime, a positive identification of the mode never seems to have been made. Only indirect evidence was offered. For example a study of the electron thermal conductivity showed that it was anomalous[44]. Among the drift waves suggested as being responsible for the anomalous losses was the DTEM. Only the DTEM and one other drift wave were found to be unstable for their parameters. A transport model based on the DTEM was found to be consistent with the observed losses. No other evidence for the DTEM was given. In another experiment involving the effects of shear on the DTEM, observations disagreed with a slab model which included the effects of the radial structure[45].

The most definitive study of the DTEM in a toroidal geometry has been performed by Prater, Eijma, and Ohkawa[46] in the General Atomic octupole. Under conditions of extremely low magnetic field (~ 100 G) they observed large scale, extremely coherent oscillations of the plasma. This mode propagates in the direction of the electron diamagnetic drift at a frequency which is approximately that predicted by linear theory (to within the uncertainty associated with the Doppler shift due to the radial electric field). The mode also follows the collisionality scaling predicted by linear theory. Based upon their data they have identified this mode as a DTEM driven by FLR effects.

Prager, Marshall, and Sen[47] at Columbia have reported observations of the DTEM in a linear magnetic mirror device. A solenoid provides a uniform field and two additional coils produce a single mirror cell. A hot cathode discharge generates the plasma. Some of the plasma is trapped in the mirror cell and the rest streams through the end of the device. The fluctuation level was measured as a function of the mirror ratio, the collisionality, and the magnetic field strength. The data are in good agreement with their theoretical predictions. In addition a physical model of the instability mechanism is presented.

The work of Prager was followed by that of Dixon, Marshall, and Sen[48] in an experiment on the same device. In this work feedback stabilization of a trapped electron mode destabilized by finite gyroradius effects was attempted. The growth rate of the DTEM was

measured as a function of the mirror ratio and the collisionality. The gain-phase data from their feedback experiment also confirms the dissipative nature of the instability.

Grubb and Emmert[49] have studied the DTEM in the Linear Multiple Mirror device. Two trapped electron modes were identified: a mode destabilized by the temperature gradient and another destabilized by finite gyroradius effects. The modes were studied as a function of the mirror ratio, magnetic field strength, and the collisionality with the experimental results being in good agreement with theory. Transfer function analysis[50,51] was used to confirm the dissipative nature of the instability.

D. Thesis Organization

The rest of the thesis is organized as follows. Chapter II is a description of the apparatus. Chapter III contains information on the diagnostics used which are predominantly Langmuir probes. A detailed description of a new method to measure the space potential with emissive probes is also presented. Chapter IV develops a dispersion relation in preparation for a comparison to the experimental results of the next chapter. The dispersion relation is general enough to include the drift cyclotron instability and trapped particle effects. Next, Chapter V presents the experimental observations and compares these observations to the predictions of the theory developed in Chapter IV. Finally, Chapter VI describes

the observation of a low frequency instability observed in a helium plasma.

References

1. N.A. Krall, "Drift Waves," in Advances in Plasma Physics, 1, edited by A. Simon and W.B. Thompson, (Interscience Publishers, New York, 1968).
2. A.B. Mikhailovskii, Theory of Plasma Instabilities Vol. 2, Instabilities of an Inhomogenous Plasma, translated by J.B. Barbour, (Consultants Bureau, New York, 1974).
3. A.A. Rukhadze and V.P. Silin, Sov. Phys. USPEKHI 11, 659 (1969).
4. U. Tserkovnikov, Sov. Phys. JETP 5, 58 (1957).
5. A. El-Nadi and H. Hassan, Phys. Fluids 25, 2140 (1982). S. Migliuolo, Phys. Fluids 25, 2289 (1982).
6. H.W. Hendel and T.K. Chu, "Collisional Drift Instabilities," in Methods of Experimental Physics, 9A, edited by R.H. Lovberg and H.R. Griem, (Academic Press, New York, 1970).
7. R.W. Motley, Q-Machines, (Academic Press, New York, 1975).
8. S. Yoshikawa, "Low Frequency Instabilities," in Methods of Experimental Physics, 9A, edited by R.H. Lovberg and H.R. Griem, (Academic Press, New York, 1970).
9. K.M. Young, Phys. Fluids 10, 213 (1967).
10. A.B. Mikhailovskii and A. Timofeev, Sov. Phys. JETP 17, 626 (1963).

11. I.B. Bernstein, Phys. Rev. 109, 10 (1958).

12. S. Ichimaru, Basic Principles of Plasma Physics, (W.A. Benjamin, Inc., Reading, Massachusettes, 1973).

13. O.P. Pogutse, Sov. Phys. JETP 20, 630 (1965).

14. L.S. Bogdankevich and A.A. Rukhadze, Sov. Phys. JETP 24, 418 (1967).

15. P.K. Shukla and M.Y. Yu, Physica 83C, 237 (1976).

16. R.F. Post and M.N. Rosenbluth, Phys. Fluids 9, 730 (1966).

17. N.T. Gladd and J.D. Huba, Phys. Fluids 22, 911 (1979).

18. J.P. Friedberg and R.A. Gerwin, Phys. Fluids 20, 1311 (1977).

19. A.B. Mikhailovsky, Nuc. Fusion 11, 323 (1971).

20. N.K. Bajaj and N.A. Krall, Phys. Fluids 15, 657 (1972).

21. N.A. Krall and T.K. Fowler, Phys. Fluids 10, 1526 (1967).

22. D. Bhadra, Phys. Rev. 161, 126 (1967).

23. T. Ohkawa and M. Yoshikawa, Phys. Rev. Lett. 17, 685 (1966).

24. B.B. Kadomstev, Sov. Phys. Lett. JETP 4, 10 (1966).

25. B.B. Kadomstev and O.P. Pogutse, Sov. Phys. JETP 24, 1172 (1967).

26. B.B. Kadomstev and O.P. Pogutse, Sov. Phys. DOKLADY 14, 470 (1969).

27. S. Prager, Ph.D. thesis, Columbia University, (1975).

28. W.M. Manheimer, "An Introduction to Trapped-Particle Instabilities in Tokamaks," ERDA Critical Review Series, TID-27157 (1977).

29. B.B. Kadomstev and O.P. Pogutse, Nuc. Fusion 11, 67 (1971). M.N. Rosenbluth, D.W. Ross, and D.P. Kostomarov, Nuc. Fusion 12, 3 (1972). B.B. Kadomstev and O.P. Pogutse in Reviews of Plasma Physics, Vol. 5, Chap. 2, edited by M.A. Leontovich, translated by H. Lashinsky, (Consultants Bureau, New York, 1970).

30. U.S. Atomic Energy Commission, "Status and Objectives of Tokamak Systems for Fusion Research," USAEC Report Wash-1295, GPO, 1974.

31. TFR Group, "T.F.R. Experiments on superbanana particle diffusion, small scale turbulence and transport," (IAEA, Brussels), report # IAEA-CN-38/N-5 (1980).

32. S.M. Mahajan, Phys. Fluids 26, 113 (1983).

33. K. Kaw, PPPL-1906, June 1982.

34. M.N. Rosenbluth, "Topics in Plasma Instabilities: Trapped Particle Modes and MHD," IFSR 62, DOE/ET/53088-62. To be published in Sov. J. Plasma Phys. (1982).

35. W.M. Tang, Nuc. Fusion 18, 1089 (1978).

36. P.J. Catto and K.T. Tsang, Phys. Fluids 21, 1381 (1978).

37. G. Rewoldt, W.M. Tang, and E.A. Frieman, Phys. Fluids 21, 1513 (1978).

38. S. Inoue, K. Itoh, and S.K. Wong, "The spatial structure of the trapped particle drift instability," Hiroshima University Report HIFT-13.

39. D.B. Batchelor and C.L. Hedrick, Nuc. Fusion 19, 235 (1979).

40. P. Deschamps, R. Gravier, C. Renaud, and A. Samain, Phys. Rev. Lett. 31, 1457 (1973).

41. C.A. Primmerman, L.M. Lidskey, and P.A. Politzer, Phys. Rev. Lett. 33, 957 (1974).

42. B. Coppi, Phys. Rev. Lett. 16, 1076 (1972).

43. M. Okabayashi and V. Arunasalam, Nucl. Fusion 17, 497 (1977).

44. S. Ejima and M. Okabayashi, Phys. Fluids 18, 904 (1975).

45. N.R. Sauthoff, M. Okabayashi, and J.A. Schmidt, Bull. Am. Phys. Soc. 20, 1289 (1975).

46. P. Prater, S. Eijma, T. Ohkawa, and S.K. Wong, Phys Fluids 21, 434 (1978).

47. S.C. Prager, T.C. Marshall, and A.K. Sen, Plasma Physics 17, 785 (1975).

48. D.P. Dixon, T.C. Marshall, and A.K. Sen, Plasma Physics 20, 189 (1978).

49. D.P. Grubb and G.A. Emmert, Phys. Fluids 22, 770 (1978).

50. R.K. Richards and G.A. Emmert, Nucl. Fusion 17, 205 (1977).

51. D.P. Grubb and G.A. Emmert, Nucl. Fusion 18, 977 (1978).

II. APPARATUS

The Linear Multi-Mirror experiment was designed by Prof. Dale Meade, built by Ray Fonck[1] in 1972, and later modified by Dave Grubb. Figure 2-1 shows the Linear Multiple Mirror in its present form. The Linear Multiple Mirror experiment is a steady-state plasma device consisting of seven consecutive short mirror cells in a 2.1 m length; the total length of the device is 4.0 m. The plasma is generated continuously at one end of the machine by a slow wave antennaa driven by 3.0 GHz microwaves and flows through a differential pumping column into the experimental region containing the multiple magnetic mirrors. A helium or neon plasma in the range $10^{10} - 10^{11}$ cm^{-3}, electron temperature between 5 and 15 eV, and ion temperature about 0.1 eV is typically studied. The mirror ratio, M, of the individual magnetic mirrors is variable between 1 and 3. The average magnetic field, $\bar{B} = (B_{max} + B_{min})/2$, is in the range 50-500 G. Table 2-1 gives a list of typical plasma parameters and other characteristic quantities.

A. Magnetic Coils and Power Supplies

Six distinct types of magnetic coils have at one time or another been used on the Linear Multiple Mirror. Each type is powered by one of four DC power supplies. The tank region of the Linear Multiple Mirror has two sets of coils, the "main field" coils and the "corrector" coils.

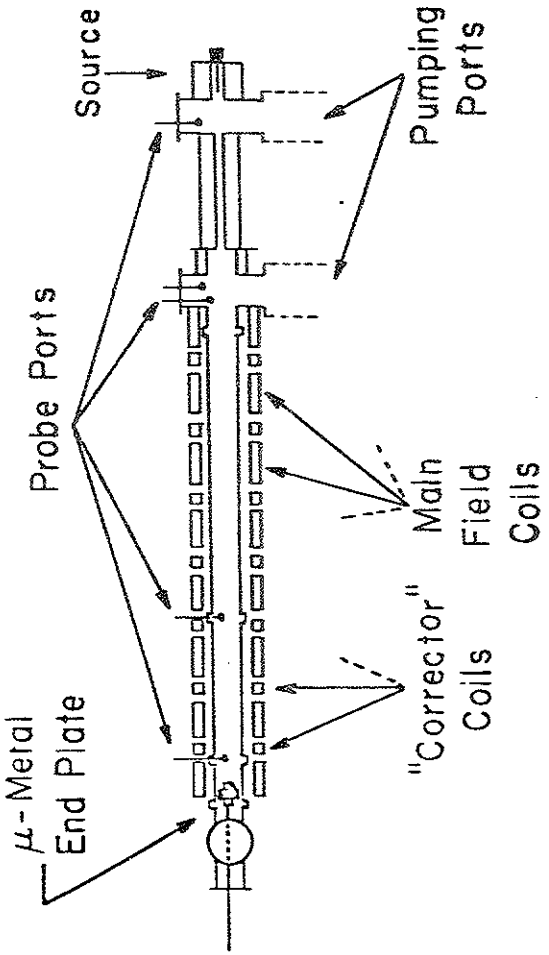

Fig. 2-1. Schematic of the Linear Multiple Mirror device showing the magnetic coil arrangement, probe ports, pumping ports, and the positions of the plasma source and end plug.

Table 2-1. Plasma Characteristic Quantities

$n = 5 \times 10^{10}$ cm^{-3}	$\rho_e = 6 \times 10^{-2}$ cm
$T_e = 10$ eV	$\rho_i = 8 \times 10^{-1}$ cm
$T_i = 0.1$ eV	$\lambda_{De} = 2 \times 10^{-2}$ cm
$B = 100$ Gauss	$\lambda_{Di} = 2 \times 10^{-3}$ cm
$P_n = 5 \times 10^{-4}$ Torr	$L_n = 2.0$ cm
Gas = Neon	$L_T = 3.0$ cm
$\nu_{ee} = 4 \times 10^{4}$ s^{-1}	$\omega_{pe} = 6 \times 10^{9}$ s^{-1}
$\nu_{ei} = 1 \times 10^{4}$ s^{-1}	$\omega_{pi} = 7 \times 10^{7}$ s^{-1}
$\nu_{ii} = 1 \times 10^{4}$ s^{-1}	$\omega_{ce} = 2 \times 10^{9}$ s^{-1}
$\nu_{en} = 1 \times 10^{6}$ s^{-1}	$\omega_{ci} = 5 \times 10^{4}$ s^{-1}
$\nu_{ionize} = 2 \times 10^{4}$ s^{-1}	$\omega_{*e} = 6 \times 10^{6}$ s^{-1}

The main field coils are 8" long and have an 11" ID. In each coil there is a total of 60 turns of 1/4" copper tubing. The tubing is wrapped into two layers and seated in epoxy. Filtered tap water is used to cool the coils. These coils are powered by the Flotrol power supply which is capable of providing up to 400 A at 50 V. However, the full range (0–400 A) is divided into two subranges (0–130 and 220–400 A) by a front panel switch on the Flotrol. In order to obtain currents in the intermediate range the load on the power supply has to be altered. The coil configuration which produces the above range is a parallel combination of two sets of four coils in series. This is shown in Fig. 2-2. If two additional coils are placed in series with the above load it is possible to obtain currents in the ranges 20–80 A and 130–300 A respectively on the Low and High settings of the Flotrol. These coils are individually capable of generating 2.10 G/Amp at the center of the coil. The average axial field produced by these coils alone in the multiple mirror arrangement is 1.19 G/Amp.

The set of eight main field coils is complemented by a set of seven corrector coils. By means of these coils it is possible to change the mirror ratio established by the main field coils. The coils are made of 1/2" copper tubing, are 2" long and have an 11" ID. Each coil is made of four electrically parallel sections of tubing wound into three layers and seated in epoxy. The coils are cooled by filtered tap water. They are wired in series and powered by the Magnaflux power supply. The Magnaflux is capable of

Fig. 2-2. Equivalent circuit of the main field coils. To obtain the desired current it is sometimes necessary to add an extra parallel load resistance.

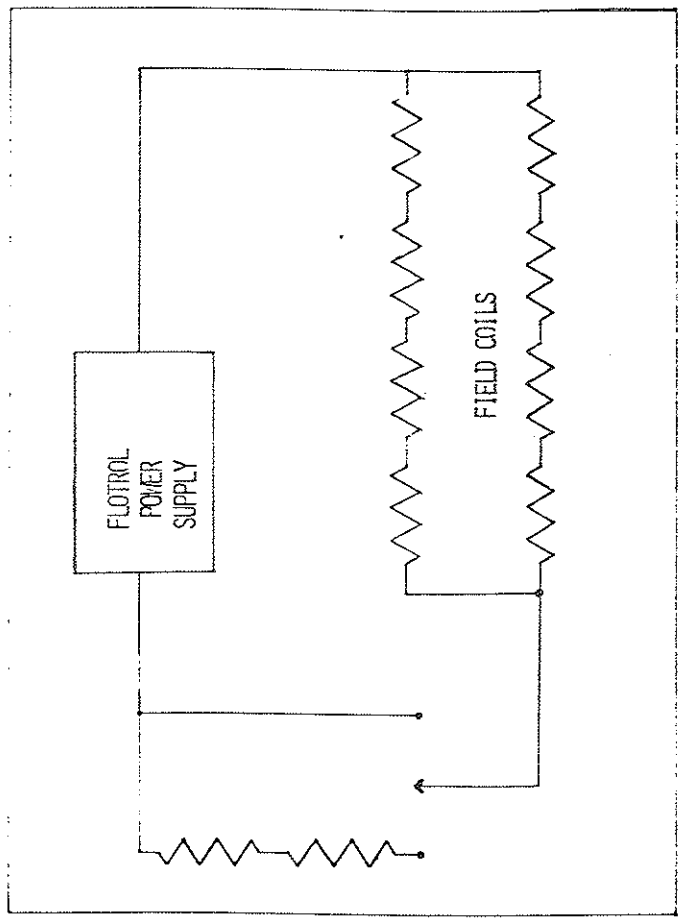

supplying up to 4 kA at 12 V. The direction of current flow into the corrector coils can be changed by switching the leads at the output of the power supply. In this way the field produced by the corrector coils can be made to be parallel or antiparallel to the main field. In the parallel case the corrector coil field reinforces the main field and smoothes it out to produce a low mirror ratio. When the corrector coil field is antiparallel to the main field the result is to further decrease the main coil field at its minimum thus increasing the mirror ratio. Mirror ratios between 1.0 and 3.0 may be obtained in this manner. The corrector coils are individually capable of generating 0.115 G/Amp at the center of the coil. The average axial field produced by these coils alone in the multiple mirror configuration is 0.066 G/Amp.

Figure 2-3 shows the magnetic field-mirror ratio parameter space of the Linear Multiple Mirror. Also shown are lines of constant magnetic field strength, $\bar{B}$, and lines of constant mirror ratio, M. The on-axis field strength and mirror ratio were measured by R. Fonck[1]. He then empirically determined a relationship between the coil currents (I_f and I_m) and the mirror ratio ($M = B_{max}/B_{min}$) and the average field strength ($\bar{B} = (B_{max}+B_{min})/2$). These relationships are

$$\bar{B} = 1.19\ I_f \pm 0.0103\ I_m$$

and

Fig. 2-3. Curves of constant magnetic field strength and constant mirror ratio in I_f - I_m parameter space (the Flotrol and Magnaflux power supply currents).

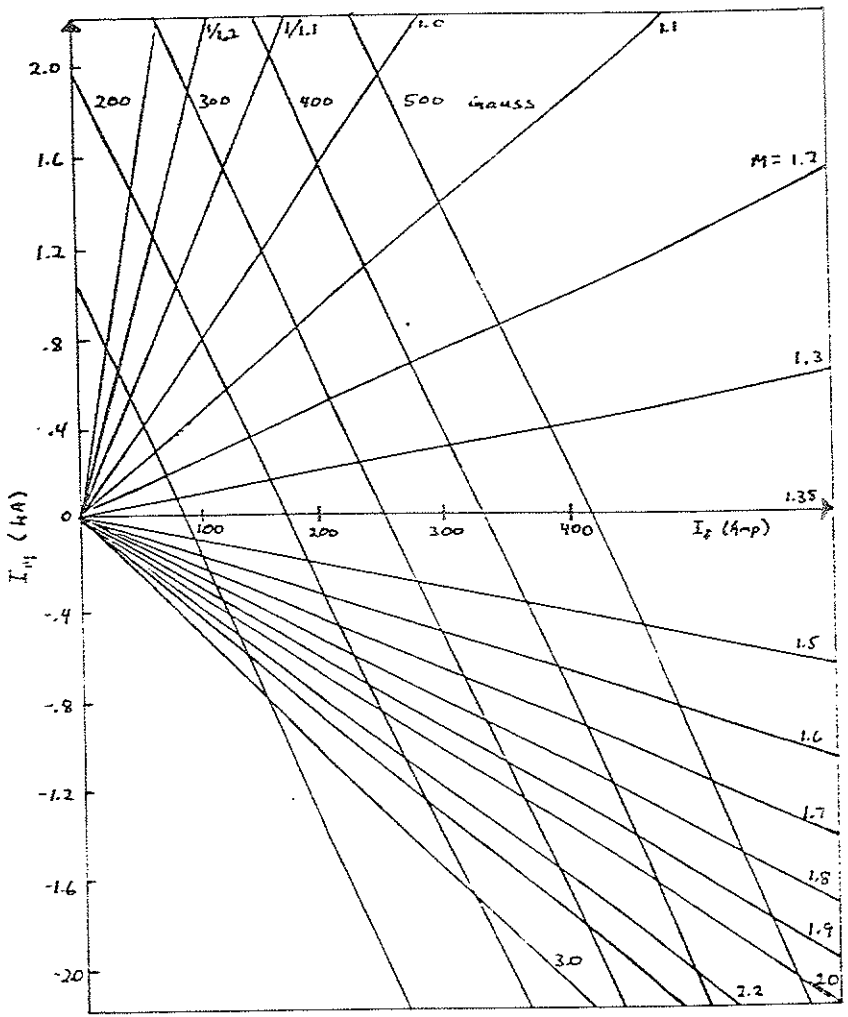

$$M = \frac{1.38\ I_f \pm 0.0785\ I_m}{I_f \pm 0.127\ I_m}$$

in which the plus (+) and minus (-) signs indicate whether the currents in the two sets of coils produce parallel or antiparallel magnetic fields respectively.

To provide the resonant magnetic field required by the plasma source two additional coils are needed. The first of these, the wire coil, is made of 3500 turns of #14 magnet wire wrapped on a copper spool. The core of the spool is a copper tube 3" long with a 2" ID. On each end of the copper tube is a copper annulus 10" in diameter. A heat conducting compound was applied between layers to facilitate cooling of the coil. The wire coil is powered by a filtered DC power supply which provides up to 5 A at 5 V. An on-axis magnetic field of 650 G is produced at 3.8 A.

The second source magnet is similar in design and construction to the main field coils. The coil is 6" long and has an 11" ID. There are three layers of 1/4" copper tubing with 22 turns per layer. The source housing (described below) fits into the spool of the wire coil which in turn fits within this coil. Current for the second source coil comes from the "Cube" power supply which supplies a highly filtered output of up to 350 A at 50 V. An identical coil is situated at the opposite end of the differential pumping column

and is wired in series with the source coil. These coils are able to generate a field of 3.05 G/Amp at the center of the coil.

Due to the nature of the area water a deposit of residue built up in all the coils and in the case of one of the black coils (the one used to generate the field for the plasma source) the deposit was severe enough to completely clog the tubing, rendering the coil useless. The combination of the wire and second source coil was replaced with a newly built coil. To remedy the potential problem of clogging in the other coils, all water cooling lines were purged with an acid solution and a water filtration system was installed to prevent future building up of residue.

The new source coil was fashioned in the spirit of all the other coils on the Linear Multiple Mirror. It consists of 17 turns of 1/4" copper tubing in each of the 8 layers on the 5" length of the coil. The layers are all seated in epoxy and the coil is cooled by filtered tap water. The coil produces a field of 10.7 G/Amp at the center of the coil.

Finally there are the two differential pumping column coils. Each coil is $9\frac{1}{2}$" in length and has a 5" ID. A total of 70 turns of 1/4" copper tubing is wound into two layers and seated in epoxy. The coils are water cooled. An arc welder supply is used to power these coils. It is capable of producing up to 400 A at 30 V. Individually, these coils produce a field of 3.02 G/Amp at the center of the coil.

Figure 2-4 shows the centerline magnetic field strength for two combinations of I_m and I_f which yield mirror ratios of 1.0 and 3.0.

B. Plasma Source and End Plate

Several different plasma sources have been used on the Linear Multiple Mirror since it was first built. Initially an interdigital Lisitano coil[2] was employed. However operation was difficult when helium was employed as the neutral fill gas. Also, only relatively low density plasmas could be obtained. To overcome these problems D. Grubb and T. Lovell[3] developed a helical type of antenna which produced higher density plasmas and worked more reliably in helium. However, this coil also suffered from some difficulties. The coil tended to sag under its own weight after prolonged periods of continuous operation. This coil also produced spatially inhomogeneous plasmas if the antenna was not properly situated in its cavity. Proper orientation was difficult to achieve especially when compounded with the sagging problem. Finally it was observed that a plasma could be generated without any helix at all. Serendipity struck when one day the source was dismantled only to find that the antenna had desoldered itself into two pieces: the helix and the stalk which connected it to the coax vaccuum feedthrough. In an attempt to find out what type of antenna was necessary a simple linear conductor was used in place of the helical antenna. When this was done a spatially homogenous and quiescent plasma was obtained. In addition considerably lower microwave

Fig. 2-4. Centerline axial magnetic field strength for two values of the mirror ratio, a) M = 1.0, and b) M = 3.0.

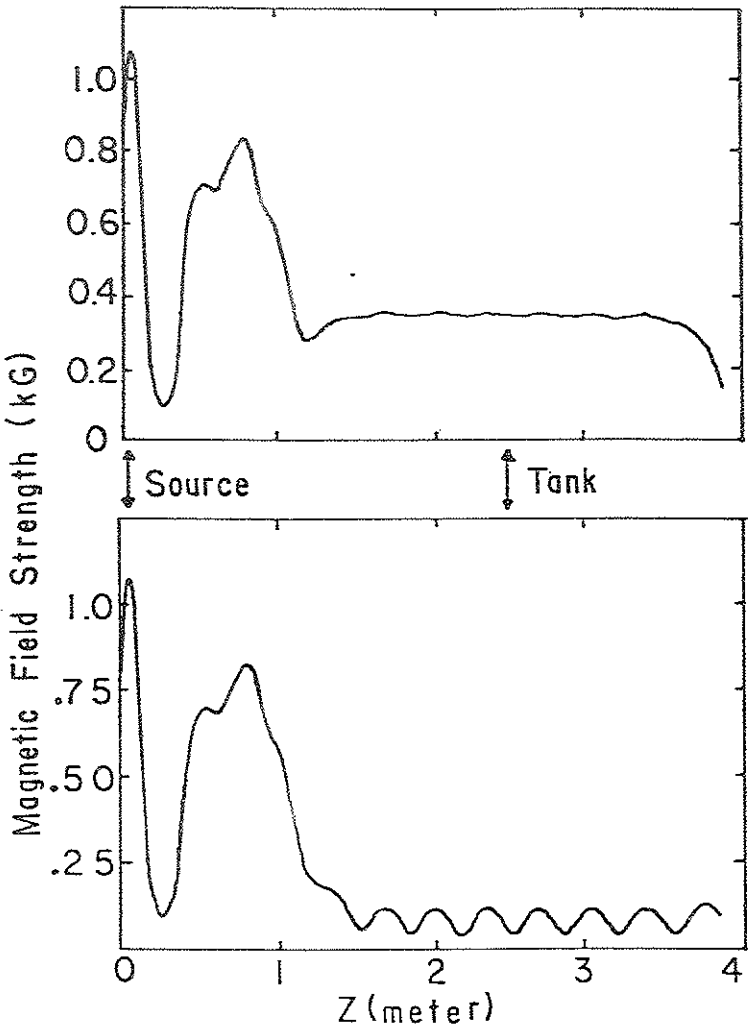

powers were needed to break down the neutral gas than with the helical antenna. When tested further, the new antenna was found to produce plasma with the same temperature and density as the original helical antenna. Due to its simplicity and ease of maintenance the straight antenna has been used ever since.

All three antennae operate by coupling microwave power into the plasma by means of electron cyclotron resonant heating (ECRH). For absorption of microwave power at the upper hybrid frequency the resonant magnetic field is determined from

$$f_a = f_{uh} = [(f_{pe})^2 + (f_{ce})^2]^{1/2}$$

which reduces to

$$f_a = 2.80\ [n(cm^{-3})\ 10^{-11} + B(kG)^2]^{1/2}\ GHz$$

For plasma densities $< 10^{11}$ cm^{-3} this becomes approximately[4] $f_a = f_{ce} = 2.80$ B(kG) GHz. At the applied frequency of 3.0 GHz the required resonant field is B = 1070 G.

Figure 2-5 shows a schematic of the plasma source in its present incarnation. Part a) is the source housing and consists of a brass tube soldered to a copper end piece. A feed hole passes through the end piece and delivers gas to the plenum. The plenum also positions an insulator which in turn holds and positions the linear antenna, part d), on the centerline of the brass tube. The

Fig. 2-5. Schematic of the present source showing a) the source housing, b) the microwave connector, c) the vacuum feedthrough, and d) the linear antenna.

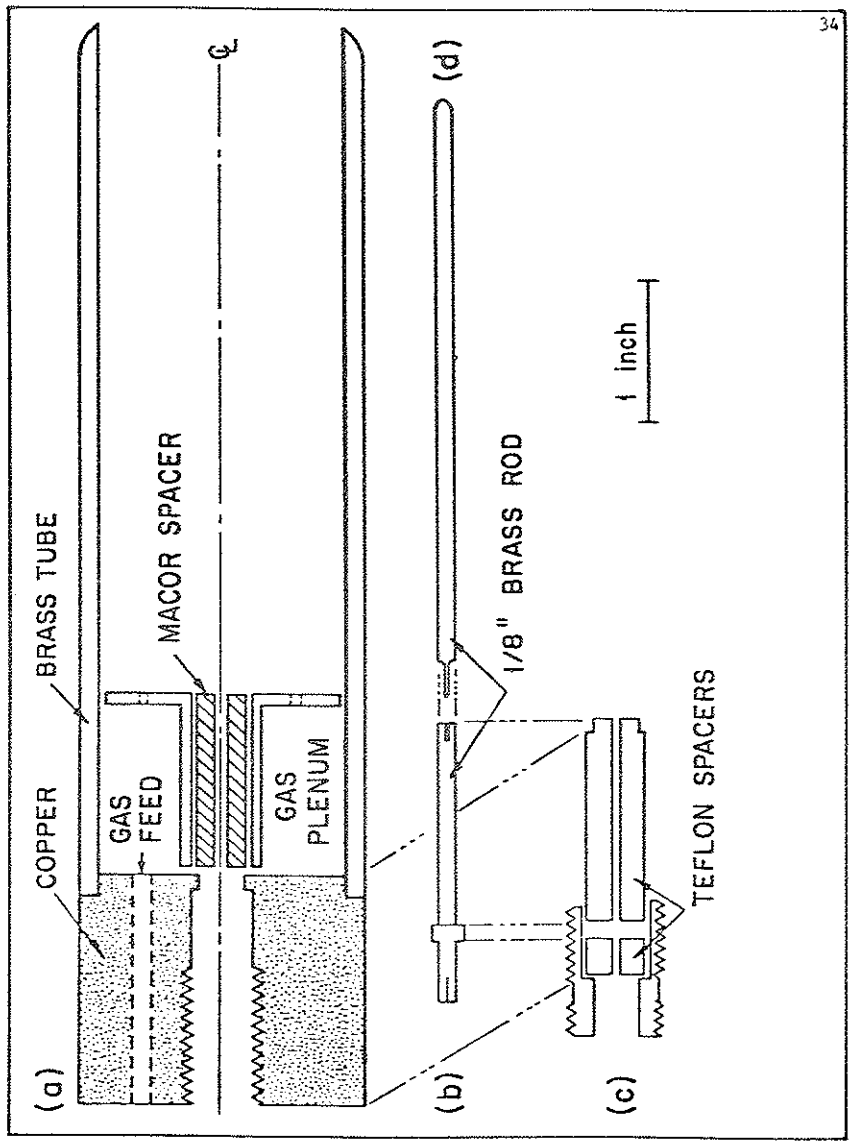

microwave vacuum feedthrough, part c), screws into the end piece. The feedthrough connector, part b), (obtained by cannibalizing a UG-29 B/U coaxial microwave connector) is held in place by two Teflon spacers. When the feedthrough is screwed into the end piece the Teflon spacers are compressed and a vacuum seal is formed at the lip on the vacuum side of the end piece.

The microwave power is supplied by a Raytheon 4J63 magnetron. This tube supplies up to 50 watts of power at a frequency which is adjustable between 2.985 and 3.385 GHz. The tube operates most efficiently at 3.0 GHz so this is the frequency used. To isolate the microwave supply from variations in the reflected power a P & H Laboratories model B1-526317 circulator was inserted into the microwave line and provides 20 db of isolation. A General Radio model 874-LK10L line stretcher is also inserted into the line to improve the impedance match between the power supply and the plasma source.

A mu-metal cylinder is located in the main tank of the Linear Multiple Mirror under the last main field coil and is used as an end plate. The cylinder is 3.8 cm in diameter, 14 cm long, and encased in glass to avoid contact with the plasma. The magnetic field at the face of the mu-metal cylinder is 2.5 to 3 times the field strength inside the other coils. This provides an end mirror which is approximately equal in magnitude to the magnetic field at the other end of the tank.

C. Vacuum System

The Linear Multiple Mirror device itself is composed of a number of sections of 6" Pyrex Conical glass pipe. The sections are joined with either an O-ring or a Teflon gasket.

Two oil diffusion pumps are used to achieve the base pressure of $\sim 1X10^{-6}$ torr. A 6" diffusion pump is used to evacuate the source region of the Linear Multiple Mirror device. This pump is separated from the source region by a 6" gate valve and a 6" refrigerated chevron baffle. The gate valve is used to adjust the neutral gas pressure in the source region and the baffle is used to prevent backstreaming of oil into the vacuum chamber.

The 10" diffusion pump serves to evacuate the tank region of the device. It too is fitted with a chevron baffle and a gate valve. However this gate valve is water cooled and not refrigerated.

Each diffusion pump is backed by a 500 l/s mechanical pump (Welch model 1397) and a foreline trap. The system is roughed down from atmospheric pressure with a Leybold-Hereaus model DK-45 pump which has a pumping speed of 650 l/min.

The tank and source regions of the machine are separated by an 18" length of 1.5" ID Pyrex glass pipe. This allows the machine to be differentially pumped. Differential pumping is sometimes necessary when the high neutral gas pressure requirement for breakdown in the source region conflicts with the low neutral gas pressure requirement of the tank region (needed to achieve a low

electron-neutral collision frequency). Pressure ratios between the source and tank regions as high as 100 can be obtained.

Three Veeco model DV-1M thermocouple gauges are used to monitor the vacuum pressure in the range 1 atm to 1 micron of the two forelines and the main tank. The gauges are powered by a Veeco TG 70 TC Gauge Controller. Two Bayard-Alpert ionization gauge tubes (Varian 563) are used to monitor the pressure in the range 10^{-3} to 10^{-7} torr in the source and tank regions of the device.

A Molytek quadrupole mass spectrometer (Spectromass 80) is used to measure the residual gas content of the vacuum system. Masses between 0 and 80 amu are detectable down to a partial pressure of 10^{-9} torr. Water has been found to be the major impurity in the system followed by a number of high-mass hydrocarbons. The hydrocarbons result from cracked diffusion pump oil which has backstreamed into the system. Figure 2-6 shows a typical plot of partial gas pressure versus mass as measured with the Spectromass 80. The peaks are labeled with likely molecular species which give rise to them[5].

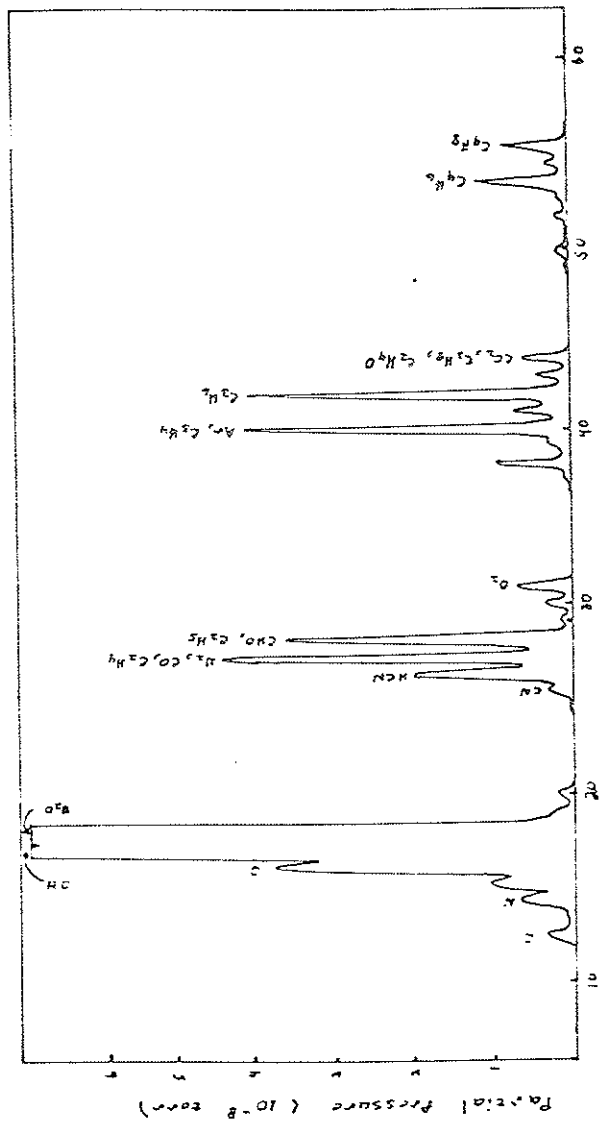

Fig. 2-6. Plot of partial pressure of contaminant gases versus atomic mass. Water is the main contaminant of the system. The hydrocarbon peaks result from cracked diffusion pump oil which has backstreamed into the system.

References

1. R.J. Fonck, Wisconsin Plasma Physics Report PLP 585 (1974).

2. G. Lisitano, I.G. Brown, and J.G. Gorman Princeton Plasma Physics Report Matt-629 (1968).

3. D.P. Grubb and T. Lovell, Rev. Sci. Instrum. 49, 77 (1978).

4. R. Prater, Ph.D. Thesis, Wisconsin Plasma Physics Report PLP 452 (1972).

5. Operating manual for the Spectromass 80.

III. DIAGNOSTICS

Langmuir probes, both cold and emissive, are the basic diagnostic used on the Linear Multiple Mirror. They serve to measure the plasma density, electron temperature, floating potential, and the plasma potential. In addition, the probes are used to measure plasma wave properties such as density and potential fluctuations. Wavelengths may also be measured by comparing the relative phase differences of signals from an array of probes. This method is used to measure both parallel and perpendicular wavelengths of the instabilities discussed below.

A. Cold Langmuir Probes

Electron temperature and density are determined from probe current-voltage (I-V) characteristics by a semi-empirical method developed by Brown, Compher, and Kunkel[1] Their method was developed for Lisitano coil generated plasmas in a strong magnetic field which is precisely the situation encountered in the Linear Multiple Mirror.

A typical I-V trace is shown in Fig. 3-1. Note that true ion saturation (zero slope) is not achieved even at large negative applied voltages. Rather, the magnitude of the ion current increases linearly with large negative applied voltages. The linear portion of the curve is extrapolated to positive voltages and serves as a baseline from which to deduce T_e from the exponentiating

Fig. 3-1. Typical current-voltage trace of a Langmuir probe used on the Linear Multiple Mirror.

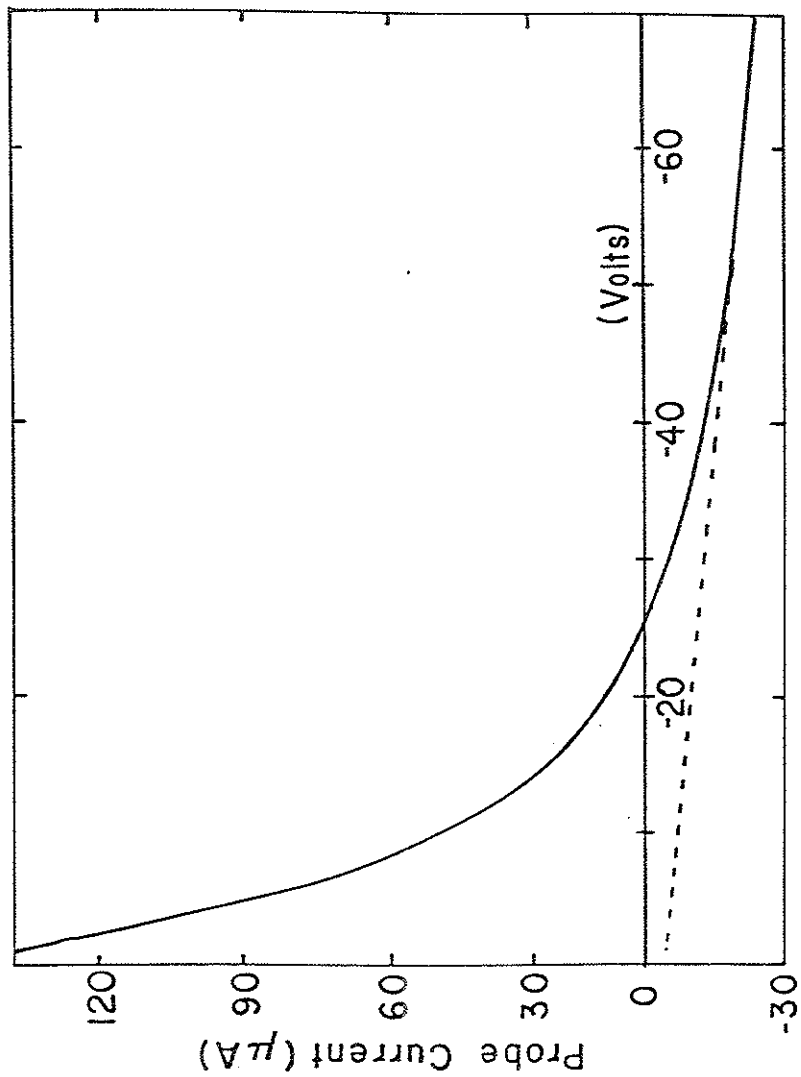

portion of the curve. The value of the ion saturation current used to deduce the density is chosen as the current $6kT_e/e$ below the floating potential. Brown, Compher, and Kunkel[1] have shown that the value of density and temperature derived by the above procedure agrees well with the density obtained from a microwave interferometer and temperature obtained from an electrostatic energy analyzer.

The ion saturation current, I^C_{oi}, for a plasma in which $T_e > T_i$ is given by

$$I^C_{oi} = \frac{1}{4}nev^*A_p = \frac{1}{4}ne\left(\frac{8kT_e}{\pi m_i}\right)^{1/2}A_p \tag{3.1}$$

where n is the plasma density, e is the electron charge, k is Boltzmann's constant, T_e is the electron temperature, A_p is the probe area, and m_i is the ion mass.

If there are no temperature fluctuations, the perturbed or fluctuating ion saturation current is

$$\delta I^C_{oi} = \frac{1}{4}\delta nev^*A_p = \frac{\delta n}{n} I^C_{oi} A_p \tag{3.2}$$

so that the density fluctuation level may be derived from a measure of the ratio of the fluctuating ion saturation current to its DC component

$$\frac{\delta n}{n} = \frac{\delta I^C_{oi}}{I^C_{oi}}. \tag{3.3}$$

B. Emissive Probes

Emissive probes are Langmuir probes with the capacity to emit electrons. Emission is usually accomplished by heating the probe to incandesence. This mode of operation was initially suggested by Langmuir himself[2].

Emissive probes are particularly useful for measuring the plasma (space) potential. This is possible since the probe emits an electron current which can be made to cancel the collected electron current. The floating potential then rises to a value close to the plasma potential.

The negative gradient of the plasma potential yields the electric field in the plasma. Standard techniques of measuring the space potential can give rise to spurious values of the electric field. For example, as an emissive probe is heated the floating potential rises and ultimately saturates at high enough probe temperatures. This saturated value of the floating potential of an emissive probe is often used for the value of plasma potential. However, the saturated value of floating potential depends on the plasma density and temperature. Thus, even if the plasma potential is constant in space, gradients in density and temperature will

cause the saturated floating potential to vary and this will give rise to a spurious electric field.

It was our good fortune to be able to develop a new method of measuring the space potential which avoided this pitfall. The new method is based on what happens to the floating potential of an emissive probe as the probe is allowed to cool slightly. This is called the "droop" method since cooling of the probe always leads to a decrease in the floating potential or, stated differently, to a voltage droop.

1. Theory

The work below was motivated by an effort to explain why the floating potential changed with time during the period that there was no heating of the filament. Figure 3-2b shows a typical scope trace made while measuring the space potential. Upon examination it is seen that the voltage "droops" during the time the heating current is off (straight line portion of the trace).

A simple explanation for this is possible if one attributes the droop to changes in the filament temperature. The decrease in temperature of the filament causes a decrease in emission. The collected electron current also drops because the probe is floating. The Langmuir characteristic requires the sheath voltage to increase. This causes the floating potential to drop. Thus the temperature drop of the filament has led to a drop in the floating potential.

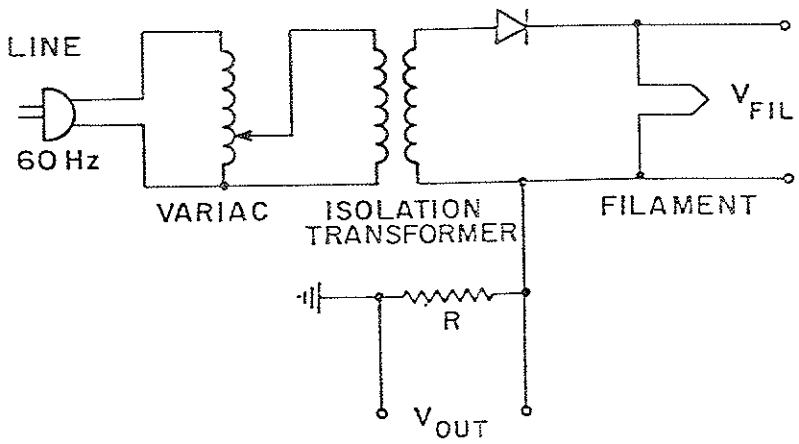

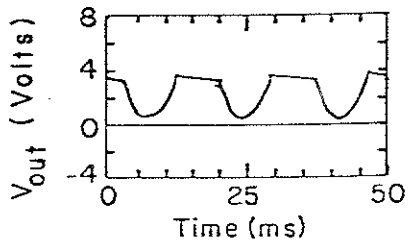

Fig. 3-2. a) Basic emissive probe circuit and b) typical scope trace of the output voltage of a floating emissive probe.

This may be made more quantitative under the simplifying condition that there are no space-charge effects present. In this case the following simple probe equations may be used (valid for cylindrical geometry). The collected electron current takes the form

$$I_e^C = \begin{cases} I_{eo}^C \exp(\eta_e), & V < V_s \\ I_{eo}^C f_e, & V > V_s. \end{cases} \tag{3.4}$$

The emitted electron current is given by

$$I_e^E = \begin{cases} I_{eo}^E, & V < V_s \\ I_{eo}^E f_w \exp(-\eta_w), & V > V_s. \end{cases} \tag{3.5}$$

Finally, for the collected ion current

$$I_i^C = \begin{cases} I_{io}^C f_i, & V < V_s \\ I_{io}^C \exp(-\eta_i), & V > V_s \end{cases} \tag{3.6}$$

where $\eta_j = e(V-V_s)/kT_j$, $(j = i,e,w)$, I_{eo}^C and I_{eo}^E are the collected and emitted electron saturation currents respectively, I_{io}^C is the collected ion saturation current, $f_e = f(\eta_e)$, $f_w = f(\eta_w)$, and $f_i = f(-\eta_i)$. The function f takes into account orbital effects involved in the collection and emission of particles from a cylindrical probe. It was first computed by H.M. Mott-Smith and I. Langmuir[3] and is given by

$$f(\eta) = 2\left(\frac{\eta}{\pi}\right)^{1/2} + \exp(\eta)\operatorname{erfc}(\eta^{1/2}) \tag{3.7}$$

where erfc is the complimentary error function.[4]

The saturated emitted electron current, I_{eo}^E, is a function of T_w and is assumed to obey the Richardson emission law[5] given by

$$I_{eo}^E = AT_w^2 \exp(-\eta_o) \tag{3.8}$$

where $\eta_o = eW/kT_w$, W is the work function of the metal and A may be regarded as a constant dependent on the properties of the metal from which the probe is made. Theoretically, A is a universal constant, but the theoretical and measured values of A are rarely the same, often deviating from one another by as much as a factor of ten.[6]

The condition that the probe float (it is assumed that each current is taken positive) is

$$0 = I_e^E - I_e^C + I_i^C. \tag{3.9}$$

Since I_e^E is a function of the wire temperature the floating

potential will also be a function of T_w. This is demonstrated in Fig. 3-3 which shows the calculated floating potential as a function of T_w for several values of the electron temperature. Here, simple forms for the collected electron and ion saturation currents have been used. The cold floating potential is obtained when the filament temperatures lies below 2000°K. When the system is perturbed by a change in the temperature and floating potential we have

$$0 = dI_e^E - dI_e^C + dI_i^C. \tag{3.10}$$

From Eqns. (3.4), (3.5), and (3.6) the differentials dI_e^E, dI_e^C, and dI_i^C may be computed as

$$\frac{dI_e^E}{I_e^E} = -[1-L(\eta_w)]\left(\frac{edV_f}{kT_w}\right) + \{\eta_1+\eta_w[1-L(\eta_w)]\}\frac{dT_w}{T_w}, \tag{3.11}$$

$$\frac{dI_e^C}{I_e^C} = L(\eta_e)\left(\frac{edV_f}{kT_e}\right), \tag{3.12}$$

$$\frac{dI_i^C}{I_i^C} = -L(-\eta_i)\left(\frac{edV_f}{kT_i}\right), \tag{3.13}$$

where $\eta_1 = 2+\eta_o$ and

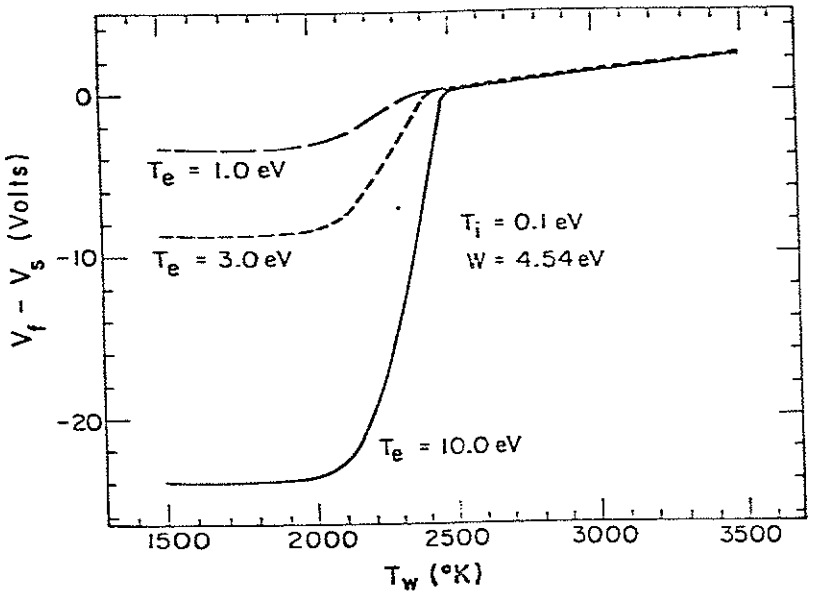

Fig. 3-3. Floating potential as a function of wire temperature calculated from Eqn. (3.9). The floating potential is a strong function of T_e when the probe floats below the V_s (= 0 Volts) but is nearly independent of T_e above V_s.

$$L(\eta) = \begin{cases} 1, & V_f < V_s \\ \dfrac{\operatorname{erfc}(\eta^{1/2})}{2\left(\frac{\eta}{\pi}\right)^{1/2}\exp(-\eta)+\operatorname{erfc}(\eta^{1/2})}, & V_f > V_s. \end{cases} \tag{3.14}$$

The definition of $L(\eta)$ is such that the expressions for the perturbed currents are valid for all voltages above and below space potential. The break in the form of the individual currents at V_s expressed in Eqns. (3.4), (3.5), and (3.6) is absorbed into $L(\eta)$, simplifying the final results. A plot of the function $L(\eta)$ is given in Fig. 3-4. Substitution of Eqns. (3.11), (3.12), and (3.13) in (3.10) and use of (3.9) yields

$$\left(\frac{edV_f}{kT_w}\right)[\tau_e L_e+(1-L_w)+\alpha M(\tau_i L_i+\tau_e L_e)] = \left(\frac{dT_w}{T_w}\right)[\eta_1+\eta_w(1-L_w)], \tag{3.15}$$

where $L_e = L(\eta_e)$, $L_w = L(\eta_w)$, $L_i = L(-\eta_i)$, $\tau_e = T_w/T_e$, $\tau_i = T_w/T_i$, and $\alpha = I^C_{io}/I^E_{eo}$. The function $M = M(\eta_w,\tau_i)$ is given by

Fig. 3-4. The L function defined in Eqn. (3.14) is constant when the floating potential is less than the space potential ($\eta < 0$) and decrease rapidly once the floating potential exceeds the space potential ($\eta > 0$).

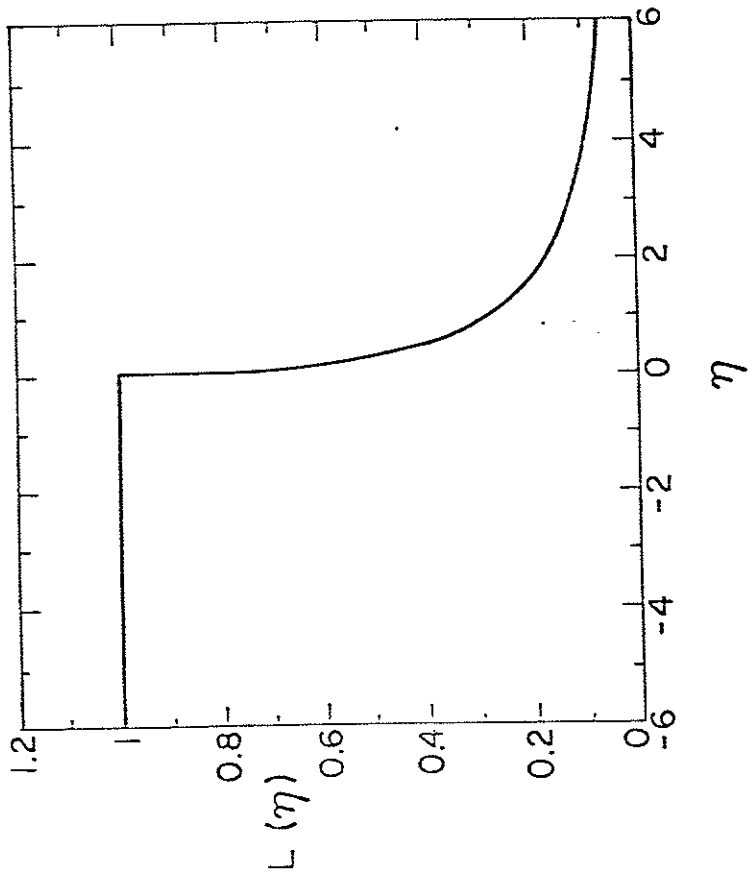

$$M = \begin{cases} 2\left(\frac{-\tau_i \eta_w}{\pi}\right)^{1/2} + \exp(-\tau_i \eta_w)\,\mathrm{erfc}\left((-\tau_i \eta_w)^{1/2}\right), & V_f < V_s \\ \dfrac{\exp[\eta_w(1-\tau_i)]}{2\left(\frac{\eta_w}{\pi}\right)^{1/2} + \exp(\eta_w)\,\mathrm{erfc}\left((\eta_w)^{1/2}\right)}, & V_f > V_s. \end{cases} \tag{3.16}$$

Plots of M versus η_w are shown in Fig. 3-5 for both $T_i > T_w$ and $T_i < T_w$. The quantity αM results from not being able to eliminate all three currents from the set of equations. The parameter α specifies the magnitude of the ratio of collected ion to emitted electron saturation currents, while M contains the voltage dependent part of these currents. It should be clear from the form of M that for $V_f > V_s$, M will either grow for $\tau_i < 1$ or tend to zero for $\tau_i > 1$.

Thus the "droop" which is the change in floating potential, dV_f, due to a change in the filament temperature, dT_w, is given by

$$\left(\frac{edV_f}{kdT_w}\right) = \frac{\eta_1 + \eta_w(1-L_w)}{\tau_e L_e + (1-L_w) + \alpha M(\tau_i L_i + \tau_e L_e)} \tag{3.17}$$

A plot of edV_f/kdT_w versus η_w is given in Fig. 3-6 for various values of α with $T_i > T_w$. This figure shows a very rapid change in edV_f/kdT_w about $V_f = V_s$ ($\eta_w = 0$) for all values of α except $\alpha = 1$.

Fig. 3-5. A plot of the M function defined in Eqn. (3.16) for several values of τ_i. Note that for $\eta_w > 0$, M either decreases exponentially to zero for $\tau_i > 1$ or increases exponentially for $\tau_i < 1$.

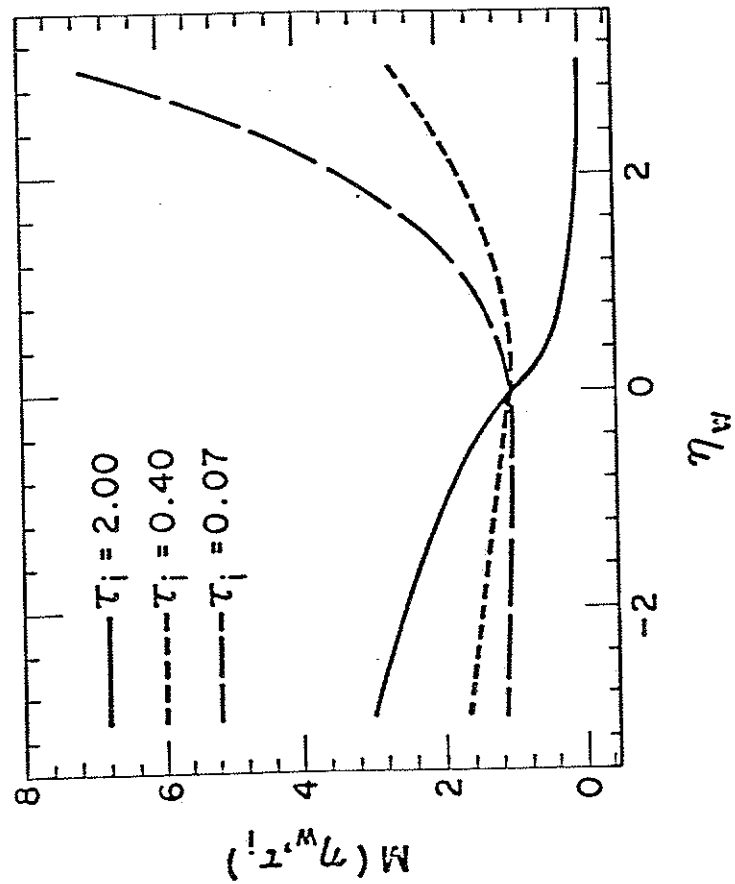

Equation (3.17) is now examined in various limits. Below V_s it is found that

$$\frac{edV_f}{kdT_w} = \frac{\eta_1/\tau_e}{1+2\alpha\left(\frac{-\eta_i}{\pi}\right)^{1/2}}, \qquad V_f < V_s. \tag{3.18}$$

When $V_f = V_s$ Eqn. (3.17) reduces to

$$\frac{edV_f}{kdT_w} = \frac{\eta_1/\tau_e}{1+\alpha(1+T_e/T_i)}, \qquad V_f = V_s \tag{3.19}$$

and when $V_f > V_s$

$$\frac{edV_f}{kdT_w} = \frac{\eta_1}{1+\frac{\alpha\tau_i}{2}\left(\frac{\pi}{\eta_w}\right)^{1/2}\exp(\eta_w-\eta_i)}, \qquad V_f > V_s. \tag{3.20}$$

Physically, one would expect α to be small when the probe floats near V_s. This is because there must be a balance between the emitted and collected electron currents, i.e. $I_e^C = I_e^E$. But $I_e^C \propto v_{te}$, the electron thermal speed while $I_i^C \propto v_{ic}$, the ion acoustic speed (when $T_e > T_i$). Hence, $\alpha = I_{io}^C/I_{eo}^E \propto (m_e/m_i)^{1/2} \ll 1$ for any probe floating near the space potential.

When $T_i = T_w$, then I_i^C changes on the same scale as I_e^E since $\eta_i = \eta_w$. Changes in the floating potential will lead to significant changes in both I_i^C and I_e^E even though the ratio of the two, α, may be small. Note that I_i^C depends on η_i both above and below V_s while I_e^E is constant below V_s and depends on η_w only above V_s. When $T_i = T_w$ the voltage dependence of the emitted electrons is effectively extended below V_s by means of the ions. The result of this is to wash out the sharp transition obtained when $\alpha = 0$ as shown in Fig. 3-6.

If instead $\tau_i = T_w/T_i \ll 1$ then $d\eta_i = \tau_i d\eta_w \ll d\eta_w$. Thus a significant change in potential with respect to the emitted electrons produces only a small change in potential with respect to the ions. The two species react differently to potential changes and the sharp transition from below to above V_s is largely restored. This may be seen in Fig. 3-7 which shows edV_f/kdT_w versus T_w for several values of T_i.

The same reasoning applies to the collected electrons and results in the condition $\tau_e \ll 1$. However, this condition is essential to distinguish between the two classes of electrons. If $T_w = T_e$ the voltage dependence of the emitted electrons is effectively extended below V_s by the collected electrons rather than the ions. There is no electron parameter corresponding to α as there was for ions to further distinguish between collected and emitted electrons. A reasonably sharp transition from below to

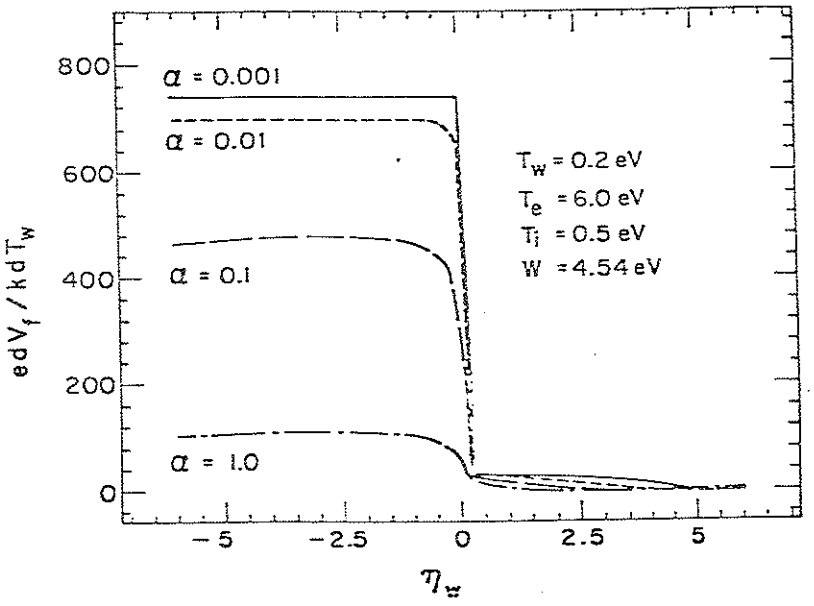

Fig. 3-6. Plots of edV_f/kdT_w versus η_w for various values of $\alpha = I^C_{io}/I^E_{eo}$ with $T_i > T_w$. The magnitude of the droop depends strongly on whether the probe floats below ($\eta_w < 0$) or above ($\eta_w > 0$) space potential.

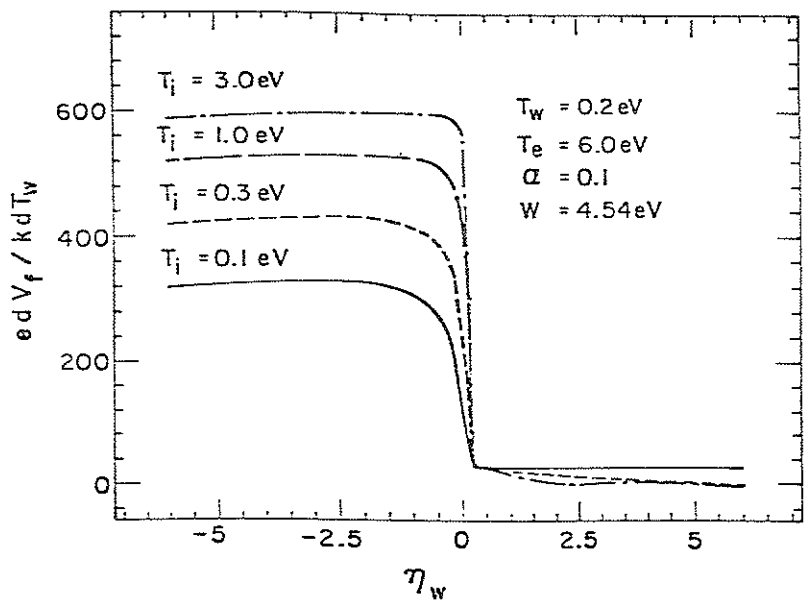

Fig. 3-7. Plots of edV_f/kdT_w versus η_w for several values of T_i. The two asymptotic values of droop are evident for $\eta_w > 3$.

above V_s will occur for any T_i, but it is necessary to have $T_e >> T_w$ for any transition to occur at all.

The effects mentioned above are most prominant at $V_f = V_s$ when they all come into play. This is seen in Eqn. (3.19). Ions reduce the droop by the factor $[1+\alpha(1+T_e/T_i)]^{-1}$. Typical parameters for our experiment are T_e = 6.0 eV, T_i = 0.1 eV, and α = 0.01 which makes $1+\alpha(1+T_e/T_i) = 1.61$ (= 1 when $\alpha = 0$). The effects of the ions are seen to be significant despite the fact that α is small.

Equation (3.20) is interesting in that the droop is asymptotic to one of two values depending on the relative values of T_w and T_i (i.e. on τ_i). If $\tau_i < 1$ then $\eta_w > \eta_i$ and the exponential factor grows with increasing potential which drives the term to zero. Conversely, if $\tau_i > 1$ the exponential term vanishes and the droop approaches η_i. The behaviour reflects the competition between the collected ion current and the emitted electron current both of which diminish above V_s with increasing η. This competition is evident in the expression for M, Eqn. (3.16), and in the plots of M shown in Fig. 3-5. The two asymptotic values may also be seen in Fig. 3-7.

From Eqns. (3.18) and (3.20) the ratio of the droop below space potential to that above (with $\alpha = 0$) is approximately

$$\frac{(dV_f/dT_w)_{V_f < V_s}}{(dV_f/dT_w)_{V_f > V_s}} \approx \frac{1}{\tau_e} \qquad (3.21)$$

The ratio is large since $\tau_e = T_w/T_e << 1$, and will be reduced somewhat by finite τ_i and α.

2. Experiment

The above analysis provides a new method with which to measure the space potential, V_s. With a warm probe floating below space potential a large droop should be observed on the voltage signal. As the probe is heated the difference between the floating potential and space potential should decrease until the difference becomes zero. At this point a sharp change in the magnitude of the droop should be observed.

These expectations are confirmed by experiment. Figure 3-8 shows a sequence of scope traces in which the floating potential is displayed as the filament temperature is varied by changing the voltage, V_{fil}, across the filament. Traces (a) and (b) show the probe just starting to heat up. The heating cycle is just becoming evident and the floating potential is slowly increasing. In (c) the heating cycle is clearly evident and a droop in the signal is becoming discernible. As the probe is heated further a droop is clearly established (d) and increases to a large value (e) while the floating potential starts to increase rapidly. Traces (f) through (i) show the transition from large to small droop as the floating potential crosses from below to above space potential. In (f) the droop is still large. A small increase in V_{fil} produces a small flattop on the signal just visible at the end of a heating cycle in

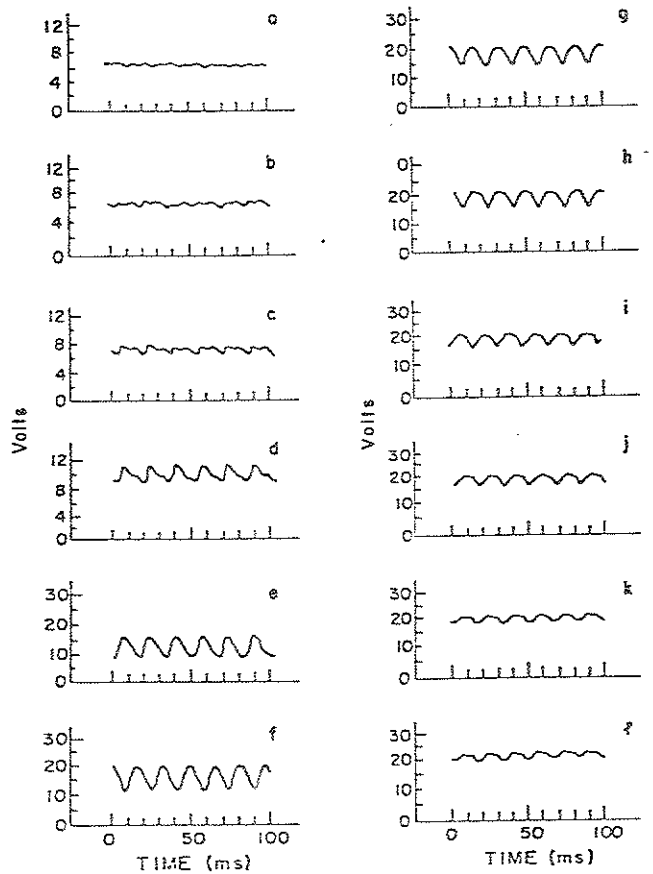

Fig. 3-8. Sequence of emissive probe traces as V_{fil} (and thus T_w) is increased. Traces a-d show the voltage droop increasing from a small to large value; e-h shows the crossing from below to above space potential; i-l shows the saturation of the voltage droop.

(g) and (h). This flattop heralds the crossing of V_s. A further increase in V_{fil} yields a complete flattop as seen in (i). The final three traces show the saturation of the floating potential. The droop appears to have saturated at this point also. These observations are in qualitative agreement with the predictions of the theory made above.

Figure 3-9 shows the measured floating potential as a function of V_{fil}. The points corresponding to the traces of Fig. 3-8 are labeled (a) through (l). The value of V_s inferred from the droop method is also labeled. Here again the results of experiment are in qualitative agreement with theory as may be seen by comparing Fig. 3-9 to Fig. 3-3.

A more quantitative comparison can be made. To do so requires that a temperature scale for the wire be established. No direct measurements of the wire temperature could be made, but a scale may still be constructed as follows. Figure 3-3 shows that the two knees in the curve of V_{float} versus T_w correspond roughly to 2000°K and 2500°K (for a tungsten filament). These temperatures will be assigned to points (c) and (h) of Fig. 3-9 and are labeled accordingly. In the spirit of this approximation the temperature will be taken as a linear function of V_{fil}. This establishes a link between the measurable quantity V_{fil} and the essential variable of the theory, T_w. The true relation between V_{fil} and T_w is certainly nonlinear in reality since changes in T_w affect the wire resistance, radiated power, and conduction losses. The approximation made here

Fig. 3-9. Measured floating potential as a function of V_{fil}. Points a-l correspond to the traces shown in Fig. 3-8. Also shown is the value of V_s obtained by means of the droop method. The points labeled 2000°K and 2500°K are inferred from Fig. 3-3.

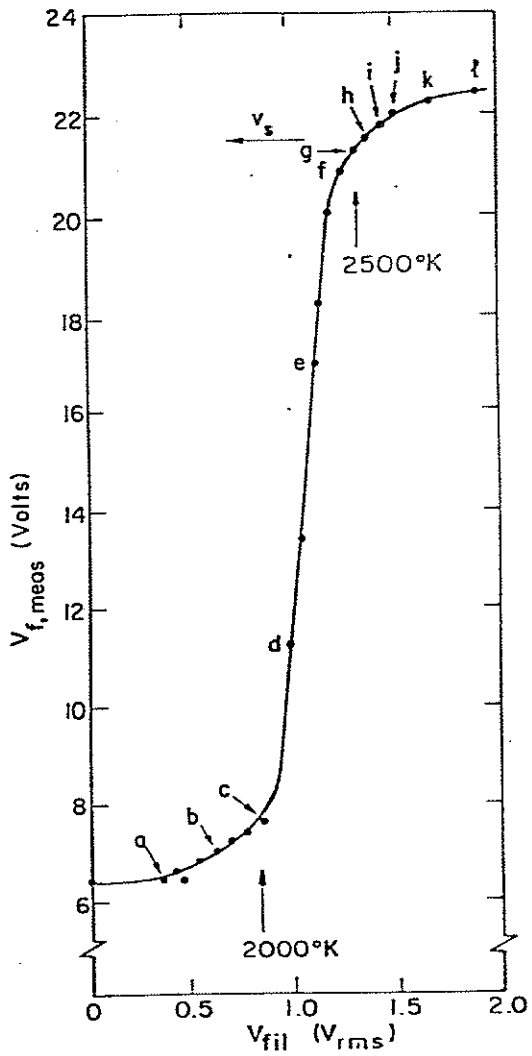

amounts to a linearization of the $V_{fil}(T_w)$ curve in the range 2000 to 2500°K.

Having constructed a temperature scale for the filament the quantity η_w can be computed for each experimental point of Fig. 3-9. This is done as follows. An approximate value of T_w has been determined for each experimental point. Also, for each experimental point the floating potential is known. Using the inferred value of V_s the quantity $\eta_{w,expt} = e(V_{f,meas} - V_{s,meas})/kT_w$ can be computed for each point. The theoretical value of the droop is then be computed from Eqn. (3.17) for each value of $\eta_{w,expt}$. This theoretical value of the droop is what the droop should be whenever the normalized floating potential is $\eta_{w,expt}$. This value may then be compared directly to the voltage droop measured from the emissive probe signals. The result of this procedure is shown in Fig. 3-10. The upper curve is the measured value of the droop normalized to dT_w = 1°K. The experimental value of the droop used was the voltage drop from the end of one heating cycle to the beginning of the next, disregarding any dip or minimum in between.

The ratio of the two values of the droop yields dT_w = 100°K. Using T_w = 2500°K as an average value we find dT_w/T_w = 3-5%, a very reasonable result. This ratio increases with increasing T_w. It is not clear whether this is due to the assumptions made about the variation of T_w with V_{fil} or reflects increasing radiation losses with increasing temperature, although the latter must contribute to the effect to some extent.

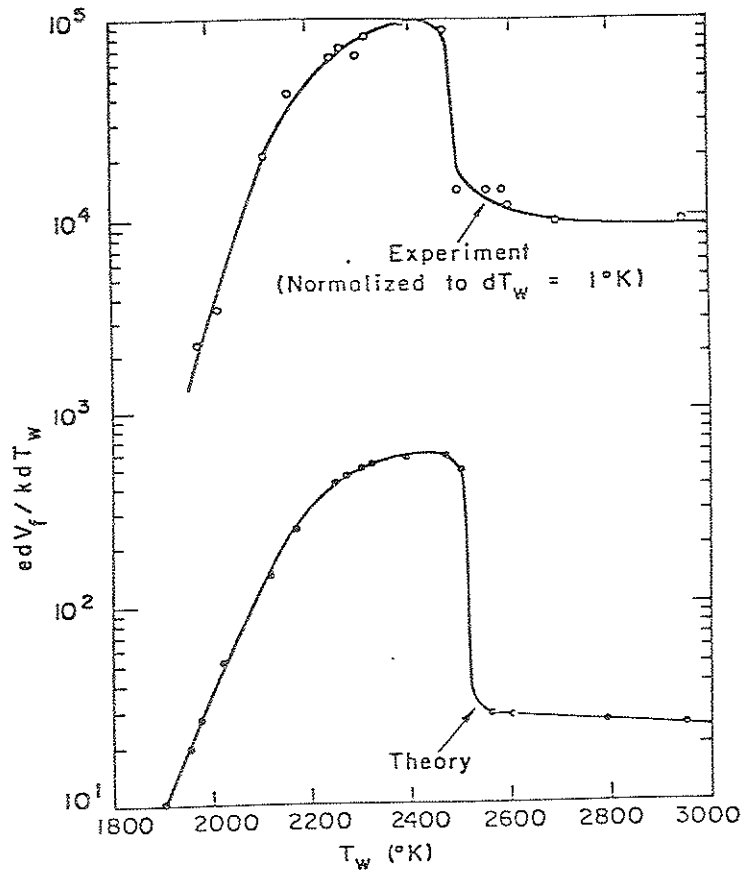

Fig. 3-10. Comparison of experimentally measured voltage droop normalized to dT_w = 1°K and the theoretical value of the droop, both as a function of T_w.

Another comparison can be made and that is the ratio of the peak droop to the saturated value of the droop ($\eta_w \gg 1$). For the lower curve this ratio is 22 and for the upper curve it is 11, experiment being a factor of two lower than the theory, but still in reasonable agreement.

Finally, it is noted that the value of V_s is always in good agreement with the value of V_s obtained from the inflection point of a Langmuir trace.

3. Discussion

The droop, edV_f/kdT_w, is simply the derivative of the floating potential with respect to the wire temperature, i.e. it is essentially the derivative of the curve shown in Fig. 3-3. From this point of view it is evident that unless $T_e \gg T_w$ there will be no knee in the curve. The greatly different slopes on either side of the knee give rise to the different values of the droop above and below space potential which is what the entire droop method is based on.

For this method to work the filament must cool during some short time interval. The filament cools by either conduction or radiation. If the filament is thin enough radiation should dominate over axial conduction. However, if one waits long enough both processes will contribute to the cooling of the filament. Thin filaments ($\lesssim$ 1 mil) are preferable, offering a large surface to volume ratio. Small volume reduces the thermal mass while a large

surface maximizes the radiative losses. Thin filaments also reduce the axial heat losses which create a nonuniform temperature distribution along the length of the filament and thus nonuniform emission; a situation which should be avoided if possible.

The fact that the droop for $V > V_s$ has two asymptotic values depending on whether T_i is greater of less than T_w might at first sight be thought to give some information about T_i. In practice this does not prove to be the case. In most plasmas of interest it is already known that $T_i > T_w$. The droop method in this case establishes a lower bound on T_i which is so low as to be next to useless ($T_w \approx 0.3$ eV at most). If $T_w > T_i$ the droop method then establishes an upper bound on T_i. However, to establish this fact one must observe the droop attain a small but finite value. Experimentally, this situation is extremely difficult to distinguish from the case $T_i > T_w$ in which the droop is initially small and finite but slowly approaching zero. This is illustrated by the sequence of data shown in Fig. 3-8. In the final frame of data it is still unclear whether the droop has saturated at a small but finite value or is whether it is still decreasing toward zero slope.

REFERENCES

1. I.G. Brown, A.B. Compher, and W.B. Kunkel, Phys. Fluids 14, 1377 (1971).
2. I. Langmuir and K.T. Compton, Rev. Mod. Phys. 3, 191 (1931).
3. H.M. Mott-Smith and I. Langmuir, Phys. Rev. 28, 727 (1926).
4. Handbook of Mathematical Functions, edited by M. Abramowitz and I. Stegun, U.S. Department of Commerce, National Bureau of Standards Applied Math Series 55, (1972).
5. O.W. Richardson, Emission of Electricity from Hot Bodies, (Logmans, Green and Co., London, 1916).
6. V.S. Fomenko and G.W. Samsonov, Handbook of Thermionic Properties, (Plenum Press, New York, 1966).

IV. BASIC THEORY

In this chapter a general dispersion relation for drift waves is derived which incorporates the main physical effects relevant to the present experiment. The relevant effects are finite ion gyroradius, collisions, electron temperature gradient, ExB drift producing a Doppler shift of the mode frequency in the laboratory frame of reference, and the presence of trapped electrons. The trapped electrons require a different treatment from that used for the ions and untrapped or circulating electrons. An effect peculiar to the trapped electrons alone is that of a curvature drift and this will be included in the theory for this species.

A. General Response for Ions and Circulating Electrons

A slab geometry is used with a magnetic field in the z-direction and density and temperature gradients in the x-direction. The diamagnetic current is then in the y-direction. To account for ∇B, curvature, and ExB drifts an effective force is assumed in the x-direction which results in a particle drift in the y-direction. The correspondence between the slab model of the theory and the cylindrical geometry of the experiment is $(x,y,z) \rightarrow (r,\theta,z)$. In the experiment the particle drifts are then in the azimuthal direction.

The starting point of the derivation is the Boltzmann equation with a Krook type collision operator

$$\frac{\partial F}{\partial t} + \vec{v}\cdot\frac{\partial F}{\partial \vec{x}} + \vec{a}\cdot\frac{\partial F}{\partial \vec{v}} = -\nu(F - F_o), \tag{4.1}$$

where F is the total distribution function, F_o is a Maxwellian distribution to which F relaxes by means of collisions, ν is the collision frequency, $\vec{v}$ is the particle velocity, n_o is the zero order density and is given by

$$n_o = \int F_o \, d^3v, \tag{4.2}$$

and $\vec{a}$ is the acceleration of a particle by the Lorentz force

$$\vec{a} = \frac{q}{m}(\vec{E} + \frac{1}{c}\vec{v} \times \vec{B}). \tag{4.3}$$

The distribution function, F, and the acceleration, $\vec{a}$, are expanded as follows

$$F = F_o + \varepsilon F_1 + \ldots, \tag{4.4a}$$

$$\vec{a} = \vec{a}_o + \varepsilon\vec{a}_1 + \ldots, \tag{4.4b}$$

where the zero and first order accelerations are specifically

$$\vec{a}_o = \frac{q}{mc}\vec{v} \times \vec{B}, \tag{4.5a}$$

$$\vec{a}_1 = \frac{q}{m}\vec{E}_1 = -\frac{q}{m}\nabla\phi, \tag{4.5b}$$

where ϕ is the electrostatic potential and ε is an expansion parameter. The last expression assumes the modes are electrostatic which is the case for the instabilities considered. A zero order electric field is not included in Eqn. (4.5a) even though ultimately the ExB drift which it causes will be considered. In the present derivation the particle drifts will enter through an effective force term in the orbit equations rather than through the $\vec{E}$ and $\vec{B}$ fields which cause the drifts in the first place.

Equations (4.4a,b) are now substituted into Eqn. (4.1) and terms of order ε^0 and ε^1 are collected to yield the following equations

$$\varepsilon^0\text{:}\quad \frac{dF_o}{dt} = \frac{\partial F_o}{\partial t} + \vec{v}\cdot\frac{\partial F_o}{\partial \vec{x}} + \vec{a}_o\cdot\frac{\partial F_o}{\partial \vec{v}} = 0, \tag{4.6a}$$

$$\varepsilon^1\text{:}\quad \frac{dF_1}{dt} + \nu F_1 = -\vec{a}_1\cdot\frac{\partial F_o}{\partial \vec{v}}. \tag{4.6b}$$

Equation (4.6a) simply states that F_o is a function of the constants of the motion which is to say that F_o is a Vlasov equilibrium. The

constants of the motion are v^2 and $\bar{X} = x + v_y/\Omega$, where $\Omega = qB/mc$ is the signed cyclotron frequency. Equation (4.6a) then yields

$$F_o = F_o(v^2,\bar{X}) = F_o(v^2,x) + \frac{v_y}{\Omega}\frac{\partial}{\partial \bar{X}}F_o(v^2,\bar{X})\Big|_{\bar{X}=x} + \cdots . \qquad (4.7)$$

Equation (4.6b) may be solved for F_1 with the introduction of an integrating factor and yields the result

$$F_1 = -e^{-\nu t}\int_{-\infty}^{t} dt' \, e^{\nu t'} \, \hat{a}_1' \cdot \frac{\partial F_o}{\partial \vec{v}'}, \qquad (4.8)$$

where a primed quantity denotes a dependence on the variable of integration, t'. The perturbed quantities n_1' and ϕ' are assumed to vary as

$$(n_1', \phi') = (\hat{n}_1, \hat{\phi})\exp[i(k_y y' + k_z z' - \omega t')], \qquad (4.9)$$

where k_y and k_z are respectively wavenumbers of the instability perpendicular and parallel to the magnetic field and ω is the frequency of the instability.

A standard calculation yields the intermediate result

$$\hat{a}_1' \cdot \frac{\partial F_o}{\partial \vec{v}'} = -\frac{q}{m}[2(\frac{d\phi'}{dt'} + i\omega\phi')\frac{\partial F_o}{\partial v^2} + \frac{ik_y\phi'}{\Omega}\frac{\partial F_o}{\partial \bar{X}}]. \qquad (4.10)$$

Substitution of Eqn. (4.10) in Eqn. (4.8) and an integration by parts to eliminate the total derivative $d\phi'/dt'$ yields

$$F_1 = 2\frac{q\phi}{m}\frac{\partial F_o}{\partial v^2} + \frac{iq\phi}{T}[2\frac{\partial F_o}{\partial v^2}(\omega+i\nu) + \frac{k_y}{\Omega}\frac{\partial F_o}{\partial \bar{X}}]\cdot I \qquad (4.11)$$

where

$$I = \int_{-\infty}^{t} dt' \exp\{i[k_y(y'-y) + k_z(z'-z) - (\omega+i\nu)(t'-t)]\} \qquad (4.12)$$

is the orbit integral along the unperturbed trajectory of the particle.

The particle trajectory including a force, F^*, in the x-direction is given by

$$y(t')-y(t) = \frac{v_\perp}{\Omega}[\cos(\Omega\tau+\theta)-\cos(\theta)] + \frac{v_D}{\Omega}\sin(\Omega\tau) - v_D\tau, \qquad (4.13a)$$

$$z(t')-z(t) = -v_z\tau, \qquad (4.13b)$$

where $\tau = t-t'$, $v_\perp$ and v_z are respectively the components of the particle velocity perpendicular and parallel to the magnetic field, $v_D = -F^*/m\Omega$ is the drift velocity, and θ is the gyro-angle. The orbit integral can be computed explicitly in terms of Bessel functions of the first kind, J_n, as

$$I = \sum_{m,n,p} i^{m+3n} \frac{J_n(\mu)J_m(\mu)J_p(\sigma)e^{i\theta(n-m)}}{-i[(\tilde{\omega}+iv) - (m-p)\Omega - k_z v_z]}, \tag{4.14}$$

where $\mu = k_y v_\perp/\Omega$, $\sigma = k_y v_D/\Omega$, $\tilde{\omega} = \omega - \vec{k}\cdot\vec{v}_D$, and $\vec{v}_D = v_D\hat{y}$.

The next step is to integrate F_1 over velocity space to obtain the perturbed density, n_1. A differential element of velocity space is $d^3v = (dv_\perp)(v_\perp d\theta)(dv_z)$. The θ integration is easily carried out since the only place which θ occurs in the expression for F_1 is in the orbit integral of Eqn. (4.14). The result is

$$\int_0^{2\pi} F_1 d\theta = 4\pi\frac{q\phi}{m}\frac{\partial F_o}{\partial v^2} - \frac{q\phi}{m}[2\frac{\partial F_o}{\partial v^2}(\omega+iv) + \frac{k_y}{\Omega}\frac{\partial F_o}{\partial X}]$$

$$\cdot 2\pi \sum_{n,p} \frac{J_n^2(\mu)J_p(\sigma)}{(\tilde{\omega}+iv) - (n-p)\Omega - k_z v_z}. \tag{4.15}$$

To carry out the $v_\perp$ and v_z integrations it is necessary to evaluate the derivative of F_o with respect to v^2. The derivative with respect to X is a spatial derivative to first order ($X = x + v_y/\Omega = x$). F_o will be taken as a Maxwellian with a density and temperature which depend on X

$$F_o = \frac{n_o(X)}{[\pi v_t^2(X)]^{3/2}} \exp\{-v^2/v_t^2(X)\} \tag{4.16}$$

where $v_t^2 = 2T(X)/m$, so that

$$\frac{\partial F_o}{\partial v^2} = -\frac{F_o}{v_t^2} = -\frac{m}{2T}F_o. \tag{4.17}$$

Hence, the perturbed density takes the form

$$n_1 = -2\pi\frac{q\phi}{T}I_1 + 2\pi\frac{q\phi}{T}[(\omega+iv) - \frac{Tk_y}{m\Omega}\frac{\partial}{\partial x}]\sum_{n,p} I_2 \tag{4.18}$$

where

$$I_1 = \int_{-\infty}^{\infty} dv_z \int_0^{\infty} dv_\perp v_\perp F_o = \frac{n_o}{2\pi}, \tag{4.19}$$

$$I_2 = \int_{-\infty}^{\infty} dv_z \int_0^{\infty} dv_\perp v_\perp \frac{F_o J_n^2(\mu)J_p(\sigma)}{(\tilde{\omega}+iv) - (n-p)\Omega - k_z v_z}. \tag{4.20}$$

To evaluate I_2 analytically it is necessary to assume that F^* is independent of velocity. This is true for the ExB drift which is the drift experimentally observed and thus the drift most relevant to the present analysis. In addition, the assumption that $\sigma \ll 1$ reduces the complexity of the final result. Generally, the condition $\sigma \ll 1$ is physically reasonable[1]. Taking the limit $\sigma \ll 1$, the sum indexed by p collapses to the $p = 0$ term with $J_o(\sigma) = 1$. Under the above approximations Eqn. (4.20) reduces to

$$I_2 = \int_{-\infty}^{\infty} dv_z \int_0^{\infty} dv_\perp v_\perp \frac{F_o J_n^2(\mu)}{(\tilde{\omega}+iv) - n\Omega - k_z v_z}$$

$$= -\frac{n_o}{2\pi k_z v_z} Z\left(\frac{\tilde{\omega} + iv - n\Omega}{k_z v_t}\right) I_n(b) e^{-b} \qquad (4.21)$$

where $b = (k_y v_t/\Omega)^2/2$, I_n is the modified Bessel function of order n and Z is the plasma dispersion function[2] defined as

$$Z(u) = \frac{1}{\pi^{1/2}} \int_{-\infty}^{\infty} \frac{e^{-x^2} dx}{x - u}. \qquad (4.22)$$

Substitution of Eqns. (4.19) and (4.21) in (4.18) yields

$$\frac{n_1}{n_o} = -\frac{q\phi}{T} - \frac{q\phi}{T}\left[(\omega+iv) - \frac{Tk_y}{m\Omega}\frac{\partial}{\partial x}\right] \frac{1}{k_z v_t} \sum_n S_n(b) Z(\xi_n) \qquad (4.23)$$

where $S_n(b) = e^{-b} I_n(b)$ and $\xi_n = (\tilde{\omega}+iv-n\Omega)/k_z v_t$.

The derivative, $\partial/\partial x$, operates on both n_o and v_t since both are functions of x in the distribution function F_o of Eqn. (4.16). Carrying out the required differentiation, the following expression is obtained for the perturbed density

$$\frac{n_1}{n_o} = -\frac{q\phi}{T}\left\{1 + \left(\frac{\omega + iv - \omega_*^T}{k_z v_t}\right) \sum_n S_n Z(\xi_n) \right.$$

$$\left. - \eta\left(\frac{\omega_*}{k_z v_t}\right) \sum_n \left[bS_n' Z(\xi_n) - \tfrac{1}{2}\xi_n S_n Z'(\xi_n)\right]\right\} \qquad (4.24)$$

where $\omega_* = k_y T/m\Omega L_n$, $\omega_*^T = \omega_*(1-\eta/2)$, $\eta = L_n/L_T$, L_n and L_T are signed density and temperature gradient scale lengths respectively, $S_n' = dS_n(b)/db$, and $Z'(u) = dZ(u)/du$.

Equation (4.24) is a general expression for the perturbed density valid for both ions and circulating electrons. It contains finite gyroradius effects through the parameter b, effects of cyclotron harmonics in the sum over n of ξ_n, the effects of a density gradient through ω_* and of a temperature gradient through η. Collisions enter explicitly through ν, the collision frequency. The effect of a drift velocity is to Doppler shift the frequency from ω to $\tilde{\omega} = \omega - \vec{k}\cdot\vec{v}_D$, which enters through the argument of the plasma dispersion function.

B. Ion Response

For ions the temperature gradient is negligible. With $L_T = 0$ Eqn. (4.24), when specialized to ions, reduces to

$$\frac{n_{1i}}{n_o} = -\frac{e\phi}{T_i}\left\{1 + \left(\frac{\omega+iv_{ii}-\omega_{*i}}{k_z v_{ti}}\right) \sum_n S_n Z(\xi_{ni})\right\}, \qquad (4.25)$$

where $\xi_{ni} = (\tilde{\omega}+iv_{ii}-n\Omega_i)/k_z v_{ti}$. The collision frequency for the ions has been taken as the ion-ion collision frequency, v_{ii}.

C. Circulating Electron Response

In the case of the electrons the temperature gradient must not be neglected. However, a simplification is possible since the gyroradius is small. If b is small the only non-negligible term in the sum over Bessel functions is the n = 0 term, and in the limit b << 1 it is found that $S_o = 1$. The sum over n disappears and Eqn. (4.24), when specialized to electrons, becomes

$$\frac{n_1^C}{n_o} = \frac{e\phi}{T_e}\left\{1 + \left(\frac{\omega+iv_e-\omega_*^T}{k_z v_{te}}\right)Z(\xi_e) + \frac{\eta\omega_{*e}}{2k_z v_{te}}\xi_e Z'(\xi_e)\right\}, \qquad (4.26)$$

where $\xi_e = (\tilde{\omega}+iv_e)/k_z v_{te}$. For circulating electrons the appropriate collision frequency is the sum of the electron-neutral, electron-electron, and electron-ion collision frequencies, i.e. $v_e = v_{en}+v_{ee}+v_{ei}$.

D. Trapped Electron Response

The character of the trapped electron orbit is what distinguishes it from the ions and circulating electrons. A trapped electron undergoes a periodic, or "bounce" motion along a magnetic field line. The analysis for the trapped electrons is analogous to that performed above but now a different set of unperturbed orbit equations is used. This completely changes the nature of the

response function. However, the general method of deriving the trapped electron response remains essentially the same and many intermediate results carry over with no change. The major difference between the two responses is largely contained in the different orbit integral of the trapped particles.

Collisions are included in the analysis explicitly through a collision frequency, $\hat{\nu}$, which is assumed to be velocity dependent. The curvature drift is modeled by an effective force, F^*, in the particle equation of motion. When the equation of motion is solved for the particle orbit a drift term results from the effective force. Temperature and density gradients enter the analysis through the spatial derivative of the distribution function which is assumed to be a Maxwellian with a spatially dependent density and temperature.

The above derivation holds with no changes up to Eqn. (4.11), which serves as the starting point for the present calculation

$$F_1 = 2\frac{q\phi}{m}\frac{\partial F_o}{\partial v^2} + \frac{iq\phi}{T}\left[2\frac{\partial F_o}{\partial v^2}(\omega+i\hat{\nu}) + \frac{k_y}{\Omega}\frac{\partial F_o}{\partial X}\right]\cdot I, \qquad (4.27)$$

where I is given by Eqn. (4.12) with ν replaced by $\hat{\nu}$.

The unperturbed particle orbits are now given by

$$y(t')-y(t) = \frac{v_\perp}{\Omega}[\cos(\Omega\tau+\theta)-\cos(\theta)] + \frac{v_D}{\Omega}\sin(\Omega\tau) - v_D\tau, \qquad (4.28a)$$

$$z(t')-z(t) = \frac{L_c}{\pi} \sin^{-1}[g\,sn(\omega_b\tau)], \tag{4.28b}$$

where $v_D = -(F^*/m\Omega)\hat{y}$ is the particle drift velocity, $\tau = t-t'$, ω_b is the bounce frequency, L_c is the mirror cell length, $g = v_z/v_\perp(2\varepsilon)^{1/2}$ is a measure of how well a particle is trapped ($g \ll 1$ corresponds to a deeply trapped particle), and sn(u) is a Jacobian elliptic function. Equation (4.28b) distinguishes the trapped particles from the streaming ones (compare to Eqn. (4.13b)) and is partially reponsible for the different type of reponse.

If one tried to proceed as above and substitute Eqns. (4.28a,b) in Eqn. (4.27) one would encounter a rather intractible definite integral. The way around this is to "bounce average" Eqn. (4.27). Formally, this involves computing

$$\langle F_1\rangle_b = \frac{1}{\tau_b}\int_0^{\tau_b} F_1 dt, \tag{4.29}$$

where $\tau_b = 2\pi/\omega_b$. Physically, this averaging removes time scales which are equal to or greater than the bounce time. The details involved in rigorously carrying out the bounce average are quite complicated[3] and will not be done here. Instead, a less rigorous route will be followed which produces the same final result. Note that only ϕ and the particle orbits contain the variable, τ, to be averaged. The procedure is to bounce average these quantities

independently. Bounce averaging the particle orbits of Eqns. (4.28a,b) yields

$$\langle y(t')-y(t)\rangle_b = -\langle v_D\rangle_b\tau - \frac{v_\perp}{\Omega}\cos(\theta), \tag{4.30a}$$

$$\langle z(t')-z(t)\rangle_b = 0. \tag{4.30b}$$

The orbit equations are seen to be substantially simplified. This is because the terms containing the very large cyclotron frequency bounce average to zero.

The bounce averaged trapped particle drift velocity, $\langle v_D\rangle_b$, contains, in addition to the ExB drift, the ∇B and curvature drifts. The last two drifts arise since the trapped electrons are localized to the bottom of a magnetic well. The trapped electrons continually sample the curvature of only a small portion of the field line and a drift results. In contrast, circulating particles are free to sample the curvature of the entire field line so that the curvature drift averages to nearly zero. It can be shown that for a magnetic field of the form $B = B_o[1 - \varepsilon\cos(k_B z)]$, the resulting curvature drift is of the form

$$\langle v_D\rangle_b = -\frac{v_\perp^2}{\Omega}\frac{\partial\varepsilon}{\partial r}\left[\frac{E(g)}{K(g)} - \frac{1}{2}\right] \tag{4.31}$$

where E and K are complete elliptic integrals of the first and

second kind respectively. In the limit $g \to 0$ (deeply trapped particles) this reduces to

$$\langle v_D \rangle_b = - \frac{v_\perp^2}{2\Omega} \frac{\partial \varepsilon}{\partial r}, \tag{4.32}$$

which is the usual form of the curvature drift when $\partial\varepsilon/\partial r$ is taken as the inverse of the magnetic field gradient scale length. Since the curvature drift always occurs in conjunction with the ∇B drift an additional term must be tacked on to Eqn. (4.32) by changing $v_\perp^2 \to v_\perp^2 + v_\parallel^2$. Note that for a trapped particle $v_\parallel^2 \leq 2\varepsilon v_\perp^2$ so that the drift is predominantly due to the curvature effect alone. Hence, Eqn. (4.32) is accurate for trapped particles as it stands.[4]

Technically, the wave potential, ϕ, must also be bounce averaged. But ϕ is assumed to vary slowly on the bounce frequency time scale and is very nearly a constant during a single bounce. The result of this is that $\langle\phi\rangle_b$ and ϕ differ very little. This combined with the fact that in order to derive a manageable dispersion relation requires that ϕ and its bounce average be taken as equal.

Evaluation of the orbit integral yields

$$I = \frac{\exp[-i\mu \cos(\theta)]}{-i(\omega - \langle k_y v_D \rangle_b + i\hat{\nu})}, \tag{4.33}$$

where $\mu = k_y v_\perp/\Omega$. Note that $\mu = (2b)^{1/2} v_\perp/v_t$ where $v_t = (2T/m)^{1/2}$ is the thermal velocity and $b = (k_y v_t/\Omega)^2/2$ is the gyroradius parameter. For electrons b is typically quite small even, at low magnetic fields. This makes μ a small parameter. The exponential in Eqn. (4.33) may be expanded in μ as

$$\exp[-i\mu \cos(\theta)] \approx 1 - i\mu \cos(\theta) - \frac{\mu^2}{2} \cos^2(\theta) + \ldots, \tag{4.34}$$

and is well approximated by unity. This results not only because μ is small but also because once the θ portion of the velocity space integration is carried out the linear term in μ will vanish. Thus in the limit that $b \ll 1$ Eqn. (4.33) becomes

$$I = \frac{i}{\omega - \langle k_y v_D \rangle_b + i\hat{\nu}}. \tag{4.35}$$

The derivative of F_o with respect to v^2 is given by Eqn. (4.17). There remains to compute the derivative with respect to X. From Eqn. (4.16) this is

$$\frac{\partial F_o}{\partial X} = \frac{F_o}{L_n} \left[1 + \eta\left(\frac{v^2}{v_t^2} - \frac{3}{2}\right)\right], \tag{4.36}$$

$$n_1^T = -n_o^T \frac{q\phi}{T} + n_o^T \frac{q\phi}{T} \left\langle \frac{\omega + i\hat{\nu} - \omega_{*T}}{\omega - \langle k_y v_D \rangle_b + i\hat{\nu}} \right\rangle, \tag{4.39}$$

where the bracket < > indicates a Maxwellian average defined by

$$\left\langle A(v) \right\rangle = \frac{4}{\sqrt{\pi}} \int_o^\infty \exp(-v^2/v_t^2) A(v) v^2 dv. \tag{4.40}$$

The fraction of trapped electrons is approximately $(2\varepsilon)^{1/2}$ where $\varepsilon = (M-1)/(M+1)$ and M = mirror ratio $= B_{max}/B_{min}$. Hence, $n_o^T = (2\varepsilon)^{1/2} n_o$ so that the expression for the perturbed density of trapped electrons is

$$\frac{n_1^T}{n_o} = (2\varepsilon)^{1/2} \frac{e\phi}{T_e} \left[1 - \left\langle \frac{\omega + i\hat{\nu} - \omega_{*T}}{\omega - \langle k_y v_D \rangle_b + i\hat{\nu}} \right\rangle \right]. \tag{4.41}$$

E. Trapped Electron Dispersion Relation

The results of sections B, C, and D are now combined in the expression for quasineutrality

$$n_{1i} - n_1^T - n_1^C = 0 \tag{4.42}$$

which yields the following dispersion relation for the trapped electron instability

where $\eta = L_n/L_T$ and L_n and L_T are respectively signed density and temperature gradient scale lengths.

Substitution of Eqns. (4.35) and (4.36) into Eqn. (4.27) yields

$$F_1 = \frac{q\phi}{T} + \frac{q\phi}{T}(\omega + i\hat{\nu} - \omega_{*T}) \frac{F_o}{\omega - \langle k_y v_D \rangle_b + i\hat{\nu}}, \tag{4.37}$$

where $\omega_* = k_y T/mQL_n$ and $\omega_{*T} = \omega_*[1 + \eta(\frac{v^2}{v_t^2} - \frac{3}{2})]$.

Yet to be performed is the velocity space integration which yields the perturbed density. This integration leads to the result

$$n_1^T = -n_o^T \frac{q\phi}{T} + 2\pi \frac{q\phi}{T} \int_{-\infty}^{\infty} dv_z \int_o^\infty dv_\perp v_\perp F_o \frac{\omega + i\hat{\nu} - \omega_{*T}}{\omega - \langle k_y v_D \rangle_b + i\hat{\nu}}. \tag{4.38}$$

It is possible to reduce the double integral over $v_\perp$ and v_z to a single integral over $v = (v_\perp^2 + v_z^2)^{1/2}$ if one assumes that v_D is a function of v^2 only. This is true for the ExB as this drift is independent of velocity. For the curvature drift it requires that $v_\perp^2 = v^2$, which is a good approximation for trapped particles.[4] The Coulomb and electron neutral collision frequencies are functions of v as are ω_{*T} and F_o. The entire integrand is then a function of v only. The reduction to a single integral is accomplished by the transformation $2\pi v_\perp dv_\perp dv_z = 4\pi v^2 dv$. Equation (4.14) becomes

$$0 = \tau \left\{1 + \left(\frac{\omega+i\nu_{ii}-\omega_{*i}}{k_z v_{ti}} \right) \sum_n S_n Z(\xi_{ni})\right\}$$

$$+ (2\varepsilon)^{1/2} \left\{1 - \left\langle \frac{\omega + i\hat{\nu} - \omega_{*T}}{\omega - \langle k_y v_D \rangle_b + i\hat{\nu}} \right\rangle\right\} \qquad (4.43)$$

$$+ [1-(2\varepsilon)^{1/2}] \left\{1 + \left(\frac{\omega+i\nu_e-\omega_*^T}{k_z v_{te}} \right) Z(\xi_e) + \frac{\eta\omega_{*e}}{2k_z v_{te}} \xi_e Z^-(\xi_e)\right\}.$$

A summary of the symbols used in Eqn. (4.43) is given in Table 4-1.

The trapped electron collision frequency, $\hat{\nu}$, is given by

$$\hat{\nu} = \nu_{en} + (\nu_{ee} + \nu_{ei})/2\varepsilon. \qquad (4.44)$$

The Coulomb collision frequency, $\nu = \nu_{ee} + \nu_{ei}$, is enhanced by a factor of $1/2\varepsilon$. The enhancement results because the relevant collision frequency is that for detrapping form the magnetic mirror, rather than the 90^o scattering time, ν_e. An electron is detrapped by scattering into the loss cone of the magnetic mirror. The loss cone boundary in velocity space is given by $2\varepsilon = (v_\parallel/v_\perp)^2$ and determines the critical pitch angle between trapped and untrapped particles. The required scattering angle must then be corrected by the factor $1/2\varepsilon$.

Table 4-1

$b = (k_y v_{ti}/\Omega_i)^2/2$ = gyroradius parameter

B = magnetic field strength

I_n = modified Bessel function of order n

k_y = perpendicular wavenumber

k_z = parallel wavenumber

L_n = density gradient scale length

L_T = temperature gradient scale length

m_e = electron mass

m_i = ion mass

M = mirror ratio

$S_n = e^{-b} I_n(b)$

T_e = electron temperature

T_i = ion temperature

$v_{te} = (2T_e/m_e)^{1/2}$ = electron thermal velocity

$v_{ti} = (2T_i/m_i)^{1/2}$ = ion thermal velocity

Z = plasma dispersion function, Eqn. (4.22)

Z^- = $dZ(u)/du$ = derivative of the plasma dispersion function

$\varepsilon = (M-1)/(M+1)$

$(2\varepsilon)^{1/2}$ = trapped fraction

$\nu_e = \nu_{en}+\nu_{ee}+\nu_{ei}$ = total circulating electron collision frequency

ν_{ee} = electron-electron collision frequency

ν_{ei} = electron-ion collision frequency

ν_{en} = electron-neutral collision frequency

Table 4-1 (Continued)

ν_{ii} = ion-ion collision frequency

$\hat{\nu}$ = $\nu_{en}+(\nu_{ee}+\nu_{ei})/2\varepsilon$ = total trapped electron collision frequency

τ = T_e/T_i

ω_{De} = circulating electron drift frequency

$\langle k_y v_D \rangle_b$ = bounce averaged trapped electron drift frequency

ω_{Di} = ion drift frequency

ω_{*e} = $k_y T_e/m_e \Omega_e L_n$ = electron diamagnetic frequency

ω_{*i} = $k_y T_i/m_i \Omega_i L_n$ = $-\omega_{*i}/\tau$ = ion diamagnetic frequency

ω_*^T = $\omega_{*e}(1-\eta/2)$

ω_{*T} = $\omega_{*e}[1 + \eta(\frac{v^2}{v_t^2} - \frac{3}{2})]$

Ω_e = $-eB/m_e c$ = electron cyclotron frequency

Ω_i = $eB/m_i c$ = ion cyclotron frequency

ξ_e = $(\omega+i\nu_e-\omega_{De})/k_z v_{te}$

ξ_{ni} = $(\omega+i\nu_{ii}-\omega_{Di}-n\Omega_i)/k_z v_{ti}$

η = L_n/L_T

Equation (4.43) is the desired result. The dispersion relation is composed of three terms, one for each "fluid:" ions, circulating electrons, and trapped electrons. In the limit $\varepsilon \to 0$, the dispersion relation reduces to the two "fluid" result usually encountered in drift wave theory. The ion response predominantly determines the real frequency of the instability. Circulating electrons basically influence the growth rate, as do the trapped electrons when present. Equation (4.43) forms the basis for all future comparisons of theory to experiment.

F. Instabilities Predicted from Theory

The dispersion relation given by Eqn. (4.43) determines the normal modes of the plasma. However, no insight is gained by a simple inspection of the result. Two approaches are available to extract information from Eqn. (4.43). The first is the use of approximations to arrive at an analytic result. This approach is taken in the next chapter. The other method is to "simply" write a program and solve Eqn. (4.43) numerically. This path is followed below.

To obtain an overview of the instabilities predicted by Eqn. (4.43) a program was written to numerically solve the dispersion relation. The program is listed with a brief description in the Appendix. The program solves for the complex frequency, ω. The wavenumbers, k_r and k_i, are taken as positive quantities. The phase velocity of the wave is then determined by the sign of the real part

of ω, $Re(\omega)$. If $Re(\omega) > 0$, then the phase velocity is also positive and the wave propagates in the direction of the electron diamagnetic current and opposite to it if $Re(\omega) < 0$. Growth or stability is determined by the sign of the imaginary part of ω, $Im(\omega)$, with $Im(\omega) > 0$ implying instability.

If n_B is the index at which the ion Bessel function sum is truncated, then Eqn. (4.43) predicts $2n_B + 1$ modes. The single mode is the standard electron drift wave and is all that remains when $n_B = 0$. The other $2n_B$ modes are cyclotron waves, n_B of which rotate in the direction of the electron diamagnetic current and n_B of which rotate in the opposite sense. (The Bessel function sum extends from $+n_B$ to $-n_B$, giving $2n_B + 1$ terms, each of which gives rise to a mode). In general, the higher the harmonic the smaller the growth rate. For simplicity the case $n_B = 1$ and $\varepsilon = 0$ will be considered. Taking $n_B > 1$ does not substantially alter the growth rate or frequency of the modes found with $n_B = 1$. When $\varepsilon = 0$ no trapped particle effects are included. Trapped particles primarily affect the growth rate and not the frequency of the mode, nor do they change the number of modes predicted.

Figures 4-1, 4-2, and 4-3 show the frequency and growth rate as a function of magnetic field strength for the three modes found with $n_B = 1$. The mode shown in Fig. 4-1 will be refered to as the $+\Omega_i$ mode. Its frequency is given approximately by $\omega = +\Omega_i$ and is found to be unstable ($\gamma > 0$) over a wide range of magnetic field strengths. The second mode, shown in Fig. 4-2, will be refered to

Fig. 4-1. The a) frequency and b) growth rate of the $+\Omega_i$ mode as a function of the magnetic field strength. The frequency is given approximately by $\omega = +\Omega_i$ and is unstable ($\gamma > 0$) over a wide range of magnetic field strengths.

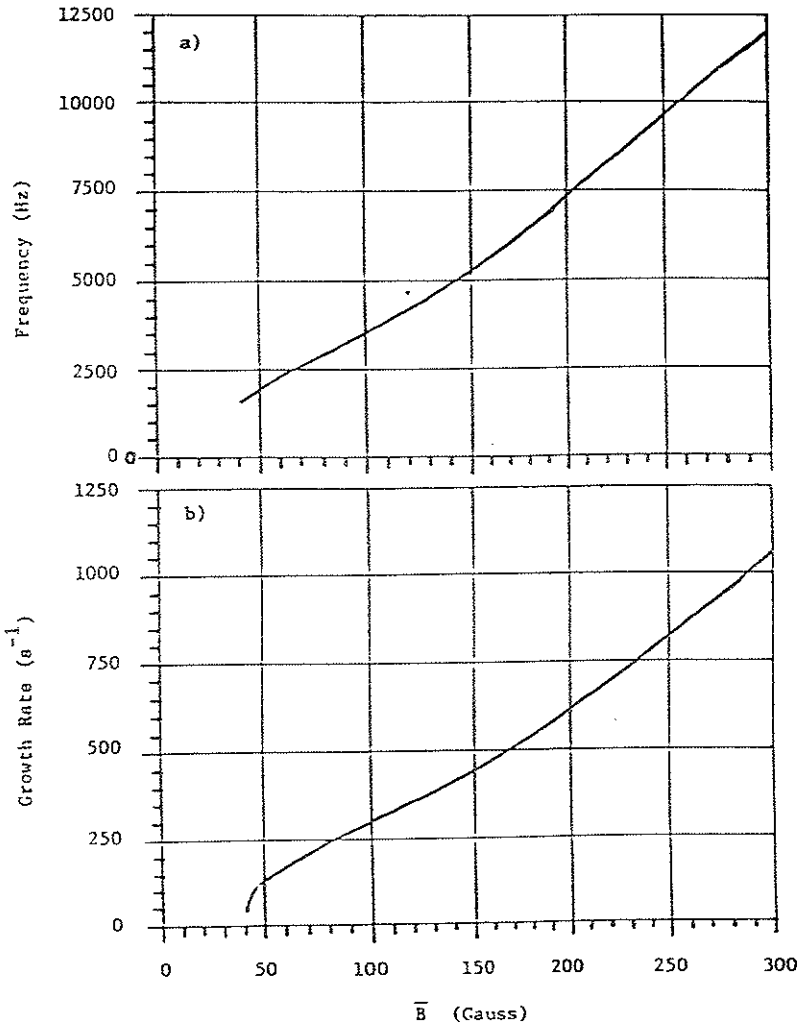

Fig. 4-2. The a) frequency and b) growth rate of the $-\Omega_i$ mode as a function of the magnetic field strength. The frequency is given approximately by $\omega \approx -\Omega_i$. There is a critical magnetic field at which the mode is marginally stable ($\gamma = 0$) and below which the mode is unstable.

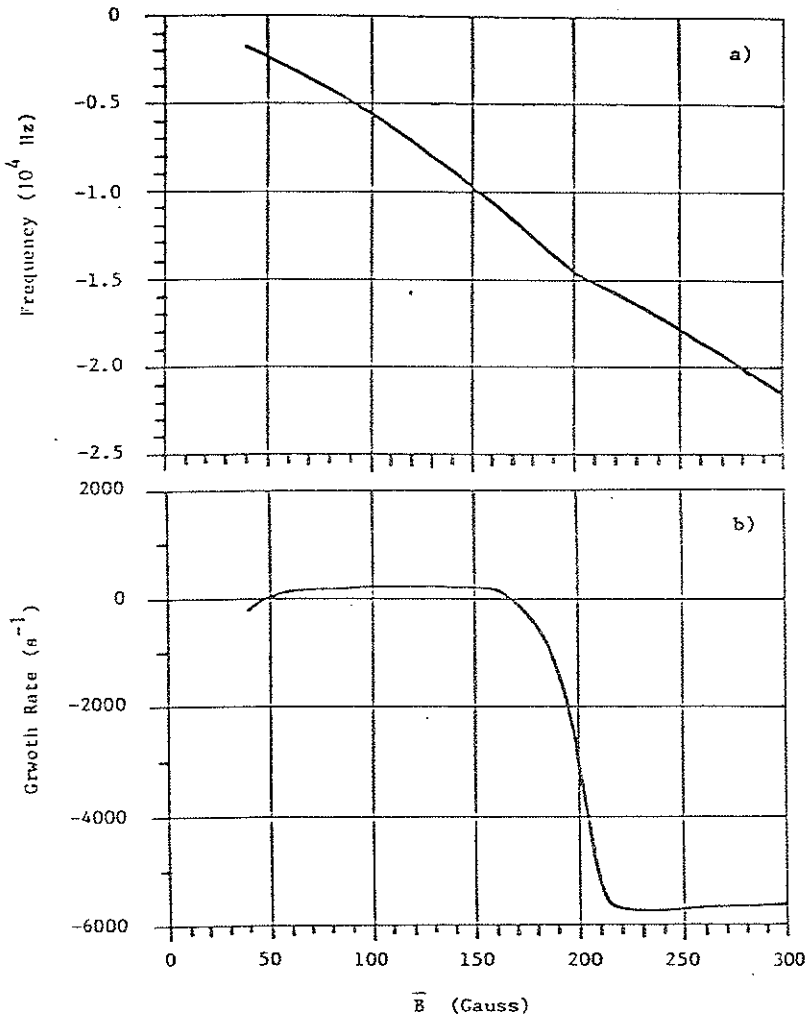

Fig. 4-3. The a) frequency and b) growth rate of the electron drift wave as a function of the magnetic field strength. The mode is unstable over a wide range of magnetic field strengths.

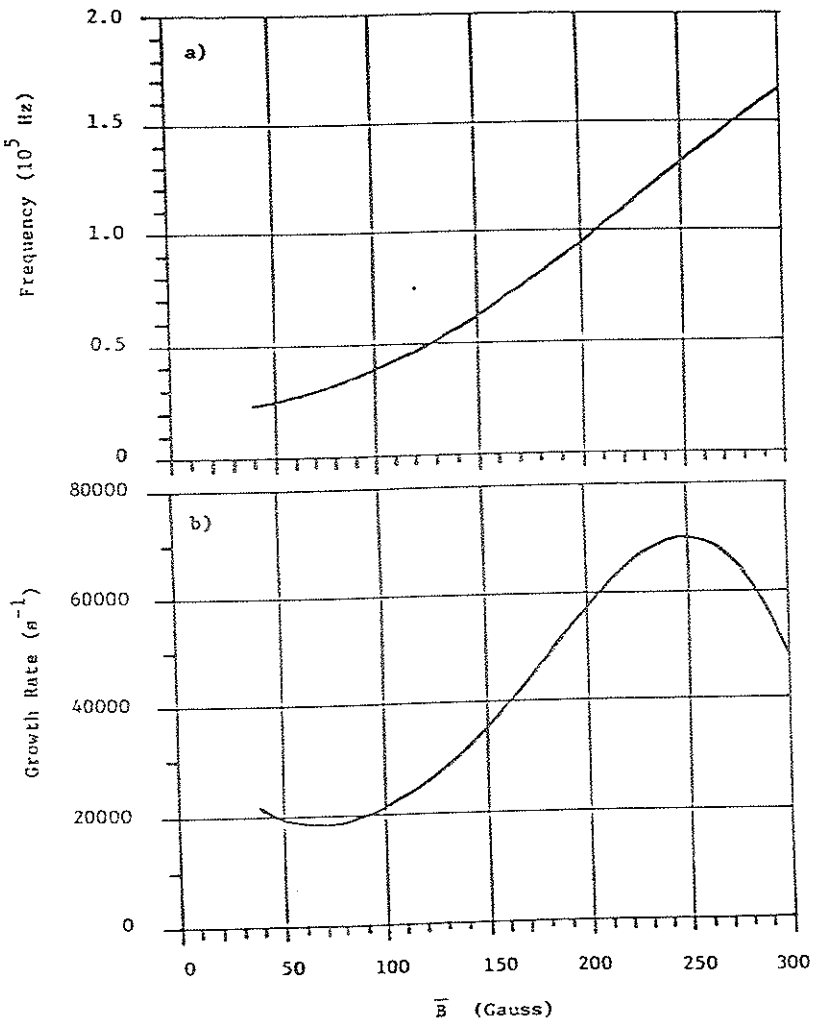

as the $-\Omega_i$ mode. Its frequency is approximately given by $\omega = \Omega_i$. Since the frequency is negative, propagation is the direction of the ion diamagnetic current. There is seen to be a critical magnetic field at which the mode is predicted to be marginally stable ($\gamma = 0$). Below the critical magnetic field the mode is unstable. The third predicted mode is the standard electron drift wave. Its frequency and growth rate are shown in Fig. 4-3.

The frequencies and growth rates of the two cyclotron waves are comparable and small compared to that of the electron drift wave. All three modes are predicted to be unstable over some range of magnetic field strengths. For the electron drift wave the unstable window of magnetic field strengths is determined by the condition $\omega < \omega_{*e}$. The $-\Omega_i$ mode is unstable for $\omega = -\Omega_i < -\omega_{*i}$. This criteria is a consequence of the mode being driven by the ion diamagnetic current. In a similar way the $+\Omega_i$ is unstable for $\omega = +\Omega_i < \omega_{*e}$. This mode appears to be driven unstable by coupling to the electron diamagnetic current and so is unstable over a wider range of magnetic fields since $T_e \gg T_i$ in the present experiment.

The above discussion is based on the numerical solution to the dispersion relation. The next chapter derives approximate expressions which put the above results on a more accessible level, than just being the results of a computer program.

References

1. N.A. Krall and M.N. Rosenbluth, Phys. Fluids 5, 1435 (1962).

2. B.D. Fried and S.D. Conte, The Plasma Dispersion Function (Academic Press, New York, 1961).

3. W.M. Tang, Nuclear Fusion 18, 1089 (1978).

4. J.C. Adam, W.M. Tang, and P.H. Rutherford, Phys. Fluids 19, 56 (1976).

V. DRIFT CYCLOTRON INSTABILITY

A. Introduction and Motivation

One of the goals of the work performed on the Linear Multiple Mirror is the investigation of trapped particle instabilities. At first glance, the drift cyclotron instability does not fit into this category. An explanation of the rationale for its study and its relation to trapped particle instabilities is therefore in order.

Trapped particle instabilities were first identified in the Linear Multiple Mirror by Grubb and Emmert[1]. These studies were performed in a helium plasma. As it turned out the trapped particle modes were very difficult to observe in isolation, i.e. without the presence of other instabilities in the plasma under conditions favorable to the observation of the trapped particle mode. Often these other instabilities coupled nonlinearly with the trapped particle mode and produced effects which, while quite interesting in themselves, were not conducive to the study of the trapped particle instability. This may be seen in Fig. 5-1 which shows an oscilloscope trace and frequency spectrum of the ion saturation fluctuations observed in a helium plasma. A frequency spectrum shows that three modes are present: two are located very close together in frequency (in the 20 kHz range) and the third has an extremely low frequency (less than 1 kHz). While some observations of this very interesting phenomena were reported[2,3] it is clear that

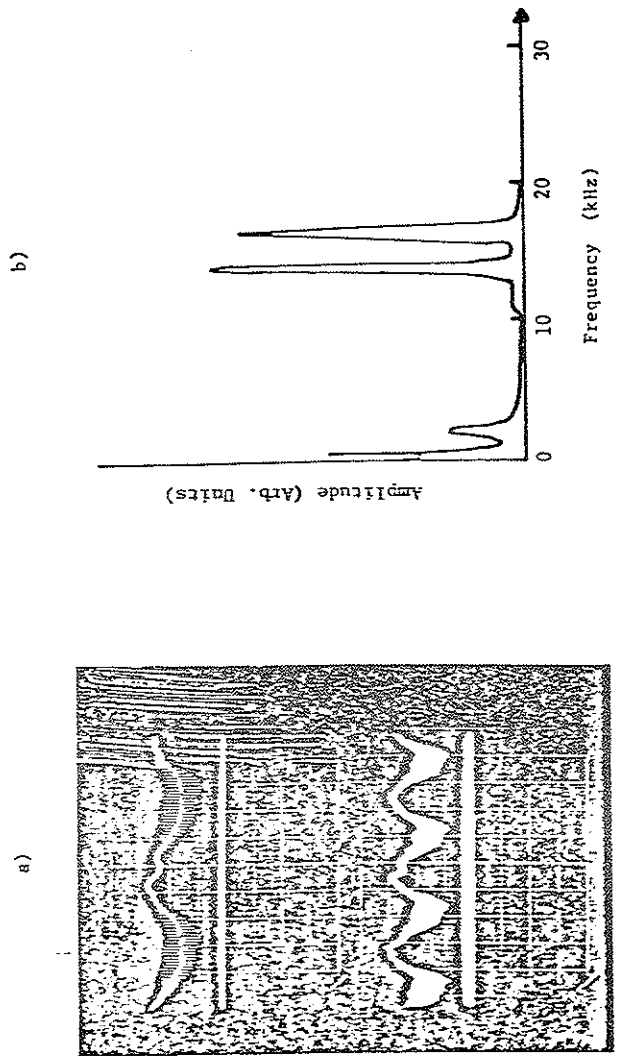

Fig. 5-1. a) An oscilloscope trace of ion saturation fluctuations in a helium plasma showing a nonlinear low frequency modulation of two higher frequency instabilities. The sweep speeds of the upper and lower traces are 1 ms/div and 2 ms/div respectively while the vertical scale for both traces is 0.05 v/div. b) The frequency spectrum of the signals shown in a).

this is not an ideal situation to study the trapped particle instability.

In the midst of the experiments and troubles in helium plasmas, work was begun with neon plasmas in order to achieve the condition $\beta > m_e/m_i$, where $\beta = nT_e/B^2/8\pi$ is the plasma beta. (When the above inequality is satisfied the wave character passes from purely electrostatic to partly electromagnetic). Later it was noted that the electron-neutral collision frequency of neon was very similar to that of helium. This may be seen in Fig. 5-2 which shows the electron neutral collision rate for helium, neon, and argon as a function electron temperature. Also, since the electron-ion collision frequency is independent of the mass the Coulomb collision frequency would be comparable in both types of plasma as long as the electron temperatures were similar. In addition, the difficulties which arose in helium plasmas in many cases did not occur at all in a neon plasma (for instance, nonlinear mode coupling), or were at least much less severe. The reason for this is not entirely clear. However, it was clear that neon offered several advantages over helium, as it provided an environment conducive to the study of trapped particle modes through its close relation to the collisional properties of helium without the problems associated with modes found in helium. Neon was therefore adopted as the working gas.

However, the switch from helium to neon did not come without its price. The experimental situation was somewhat cleaner but with respect to theory the picture had clouded over somewhat. The reason

Fig. 5-2. Electron-neutral collision rates as a function of T_e for helium, neon and argon. The collision rates of helium and neon are similar in magnitude and dependence on T_e.

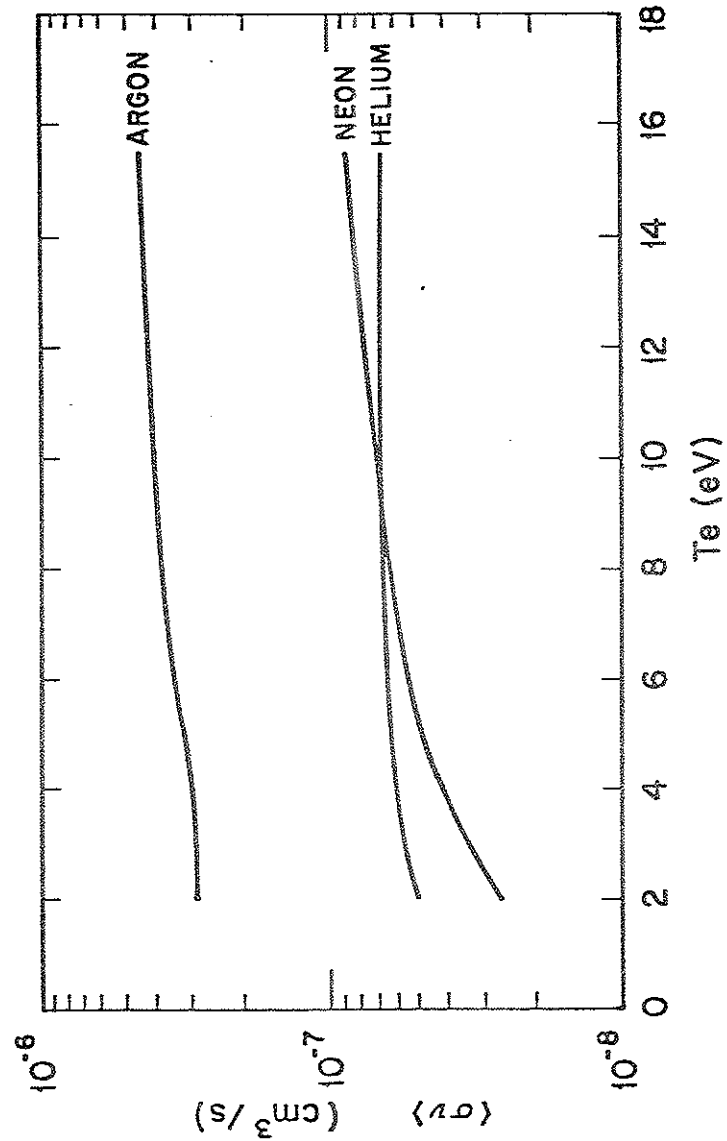

for this is the reduction of the ion cyclotron frequency by a factor of 5 when the switch from helium (A = atomic number = 4) to neon (A = 20) is made.

The low ion cyclotron frequency greatly complicates the analysis. In addition, in some instances, the ion cyclotron frequency could be below the ion diamagnetic frequency which opens the door to other instabilities besides the basic electron drift wave. In particular, the drift cyclotron instability was a possibility in a neon plasma. In helium the drift cyclotron instability could safely be ignored. Also, finite gyroradius effects are non-negligible which necessitates a kinetic treatment of the ions. This chapter is devoted to an experimental and theoretical investigation of the drift cyclotron instability in a neon plasma.

The signature of a "pure" trapped particle instability is that it have zero growth rate in the presence of a uniform field (if no trapped particles, then no instability). In this case the search for trapped particle instabilities reduces to looking for instabilities whose amplitude decreases with decreasing mirror ratio and which vanish altogether at uniform field (mirror ratio of unity).

Unfortunately, this simple picture does not hold in the present experiment. The theoretically predicted instabilities are always found to be unstable even if the field is uniform. This says that trapped particles are not necessary to insure that a mode be

unstable, as would be the case for a "pure" trapped particle instability. In the present case the trapped particles constitute a perturbation to the basic instability occuring at uniform field. Varying the mirror ratio introduces trapped particles which has the effect of altering the amplitude of the instability in a manner dependent on the particular instability. In the case of the drift cyclotron instability, the dependence on mirror ratio is weak, while that for an electron drift wave is much stronger. Perhaps a better term for these instabilities would be trapped particle modified instabilities.

It is in the sense of a trapped particle modified instability that the drift cyclotron instability will be considered. In this way the drift cyclotron mode is an extension of the previous work on trapped particle instabilities.

B. Simplified Theory of the Drift Cyclotron Instability

The statement that the above modes are trapped particle modified instabilities can be given a more precise interpretation by means of results obtained from a simplified version of the dispersion relation developed in Chapter IV. From the simplified dispersion relation it is possible to derive results which reflect the gross trends of the modes predicted from the full dispersion relation given by Eqn. (4.43).

The procedure is to examine the different response functions one at a time. The ions will be considered first. Define D^I, the ion response function, as

$$D^I = \tau \left\{1 + \left(\frac{\omega + iv_{ii} - \omega_{*i}}{k_z v_{ti}} \right) \sum_n S_n Z(\xi_{ni}) \right\}. \tag{5.1}$$

This may be simplified by retaining only the n = -1,0,1 terms in the sum over cyclotron harmonics. Next, in order to eliminate the Z-function, it is assumed that

$$\omega = \pm \Omega_i \tag{5.2a}$$

but that

$$\frac{\omega \pm \Omega}{k_z v_{ti}} \gg 1. \tag{5.2b}$$

The large argument expansion of the Z-function can then be used. Physically, Eqns. (5.2a,b) maximize the number of resonant particles interacting with the wave, and thus the growth rate is maximized. Lastly, in order to extract a growth rate from the final result it is necessary to assume

$$\frac{\nu_{ii}}{\Omega_i} \ll 1. \tag{5.3}$$

With these approximations it is possible to simplify Eqn. (5.1) to the form

$$D^I = D_r^I + iD_i^I \tag{5.4}$$

where D_r^I and D_i^I are respectively the real and imaginary parts of D^I and are given approximately by

$$D_r^I = \tau[1 - (1 - \frac{\omega_{*i}}{\omega})(S_o + \frac{2S_1\omega^2}{\omega^2 - \Omega_i^2})], \tag{5.5a}$$

$$D_i^I = -\tau \frac{\nu_{ii}}{\omega}\{\frac{\omega_{*i}}{\omega}[S_o + \frac{2S_1\omega^2(\omega^2 + \Omega_i^2)}{(\omega^2 - \Omega_i^2)^2}] - \frac{4S_1\omega^2\Omega_i^2}{(\omega^2 - \Omega_i^2)^2}\}, \tag{5.5b}$$

where $S_o = e^{-b}I_o(b)$ and $S_1 = e^{-b}I_1(b)$ are the modified Bessel functions arising from the finite gyroradius of the ions.

The treatment of the circulating electrons is less involved. Here, it is assumed that

$$\left| \frac{\omega + i\nu_e}{k_z v_{te}} \right| \ll 1 \tag{5.6a}$$

which allows the use of the small argument expansion of the Z-function. Anticipating the final result that

$$\omega_*^T = \omega_{*e} \gg \omega \tag{5.6b}$$

it is then possible to simplify the circulating electron response function D^{EC}, where

$$D^{EC} = (1-\sqrt{2\varepsilon})\{1 + (\frac{\omega+i\nu_e-\omega_*^T}{k_z v_{te}})Z(\xi_e) + \frac{\eta\omega_{*e}}{2k_z v_{te}}\xi_e Z'(\xi_e)\}$$

$$= D_r^{EC} + iD_i^{EC} \tag{5.7}$$

where D_r^{EC} and D_i^{EC} are the real and imaginary parts of D^{EC}. With the above approximations D_r^{EC} and D_i^{EC} are found to be

$$D_r^{EC} = 1 - \sqrt{2\varepsilon}, \tag{5.8a}$$

$$D_i^{EC} = (1 - \sqrt{2\varepsilon})[-\sqrt{\pi}\frac{\omega_*^T}{k_z v_{te}} + \frac{\nu_e}{k_z v_{te}}(\frac{2\omega_{*e}}{k_z v_{te}})(1 - \eta)]. \tag{5.8b}$$

Equation (5.8a) says that the response of the circulating electrons is essentially Boltzmann. The imaginary part of the response has two terms. The first is always destabilizing and results from a Landau resonance between the circulating electrons and the wave. The second term may be either stabilizing or destabilizing depending on the sign of $(1-\eta)$. Electron collisions are always stabilizing when there is no temperature gradient present ($\eta = 0$). However, for $\eta > 1$, electron collisions are destabilizing.

The trapped electrons remain to be considered. They are the easiest to treat, but this ease is only superficial since the response is buried in the averaging process. All that is necessary for the moment is to assume that

$$\mathrm{Re}\ \sqrt{2\varepsilon}\left\langle \frac{\omega + i\hat{\nu} - \omega_{*T}}{\omega - \langle k_y v_D\rangle_b + i\hat{\nu}} \right\rangle \ll 1 \tag{5.9}$$

i.e. the Maxwellian average yields a contribution only to the growth rate. Numerical computation shows that Eqn. (5.9) is true for $\hat{\nu}/2\varepsilon\omega > 1$ which is the experimental range of interest. Hence, the trapped electron response function D^{ET} given by

$$D^{ET} = \sqrt{2\varepsilon}\left\{1 - \left\langle \frac{\omega + i\hat{\nu} - \omega_{*T}}{\omega - \langle k_y v_D\rangle_b + i\hat{\nu}} \right\rangle\right\}$$

$$= D_r^{ET} + iD_i^{ET}, \tag{5.10}$$

where D_r^{ET} and D_i^{ET} are respectively the real and imaginary parts of D^{ET} and are approximately

$$D_r^{ET} = \sqrt{2\varepsilon}, \tag{5.11a}$$

$$D_i^{ET} = -\sqrt{2\varepsilon}\ \mathrm{Im}\left\langle \frac{\omega + i\hat{\nu} - \omega_{*T}}{\omega - \langle k_y v_D\rangle_b + i\hat{\nu}} \right\rangle. \tag{5.11b}$$

The above results can now be combined to give an approximate dispersion relation

$$D = D_r + iD_i = 0 \tag{5.12}$$

where $D_r = \mathrm{Re}(D)$ is

$$D_r = D_r^I + D_r^{EC} + D_r^{ET}$$

$$= 1 + \tau\left[1 - (1 - \frac{\omega_{*i}}{\omega})(S_o + \frac{2S_1\omega^2}{\omega^2 - \Omega_i^2})\right], \tag{5.13a}$$

and $D_i = \mathrm{Im}(D)$ is approximately

$$D_i = D_i^I + D_i^{EC} + D_i^{ET}$$

$$= -\tau\,\frac{\nu_{ii}}{\omega}\left\{\frac{\omega_{*i}}{\omega}\left[S_o + \frac{2S_1\omega^2(\omega^2 + \Omega_i^2)}{(\omega^2 - \Omega_i^2)^2}\right] - \frac{4S_1\omega^2\Omega_i^2}{(\omega^2 - \Omega_i^2)^2}\right\}$$

$$- \sqrt{2\varepsilon}\ \mathrm{Im}\left\langle \frac{\omega + i\hat{\nu} - \omega_{*T}}{\omega - \langle k_y v_D\rangle_b + i\hat{\nu}} \right\rangle \tag{5.13b}$$

$$- (1 - \sqrt{2\varepsilon})\left[-\sqrt{\pi}\frac{\omega_*^T}{k_z v_{te}} + \frac{\nu_e}{k_z v_{te}}\left\{\frac{2\omega_{*e}}{k_z v_{te}}\right\}(1 - \eta)\right].$$

Next assume that $D_i/D_r \ll 1$ so that $D_r = 0$ determines the real frequency of the instability. The growth rate may then be computed from

$$\gamma_j = - \frac{D_i}{\left.\frac{\partial D_r}{\partial \omega_r}\right|_{\omega_j}} . \tag{5.14}$$

Clearing fractions in Eqn. (5.13a) yields the following cubic equation in ω

$$0 = \omega^3[1+\tau(1-S_o-2S_1)]+\omega^2\tau\omega_{*i}(S_o+2S_1) - \omega\Omega_i^2[1+\tau(1-S_o)]-\tau\omega_{*i}\Omega_i^2 S_o. \tag{5.15}$$

From Eqn. (5.2a) it is already known that two approximate roots to this cubic equation are $\omega = \pm\Omega_i$. The third is root is the usual electron drift wave with finite gyroradius corrections. These initial estimates of the roots can be refined by assuming solutions of the form

$$\omega_{1,2} = \pm\Omega_i + \Delta_{1,2} \tag{5.16}$$

where Δ is a small correction such that $\Delta/\Omega_i \ll 1$. Equation (5.16) is now substituted in Eqn. (5.15) and linearized with respect to Δ.

It is then a simple matter to collect similar terms and solve for the corrections, $\Delta_{1,2}$. The results are

$$\Delta_{1,2} = \frac{-S_1\tau(\omega_{*i} \mp \Omega_i)\Omega_i}{\Omega_i[1+\tau(1-S_o-3S_1)] \pm \tau\omega_{*i}(S_o+2S_1)}. \tag{5.17}$$

Since $\tau = T_e/T_i \gg 1$ and $\Omega_i \doteq \omega_{*i}$, the magnitude of Δ is proportional to S_1 which is a small parameter yielding the Bessel function correction for finite gyroradius effects.

Now, by means of Eqn. (5.14), the growth rates of the modes of Eqn. (5.16) can be computed. The results are

$$\gamma_{1,2} = -\nu_{ii} - \frac{\Delta_{1,2}^2\omega_i^2}{\tau[S_o\omega_{*i}\Delta_{1,2}^2 + S_1\Omega_i^2(\omega_{*i}\mp\Omega_i)]} \cdot \left\{ -\sqrt{2\varepsilon}\ \mathrm{Im}\left\langle \frac{\omega_{1,2} + i\hat{\nu} - \omega_{*T}}{\omega_{1,2} - \langle k_y v_D\rangle_b + i\hat{\nu}} \right\rangle + (1-\sqrt{2\varepsilon})\left[\sqrt{\pi}\,\frac{\omega_*^T}{k_z v_{te}} - \frac{\nu_e}{k_z v_{te}}\left(\frac{2\omega_{*e}}{k_z v_{te}}\right)(1-\eta)\right]\right\}. \tag{5.18}$$

Several facts are evident from Eqn. (5.18). Most obvious is that ion-ion collisions are a stabilizing influence. However, the simple analysis used to arrive at this result is not adequate. This will be discussed further below.

To proceed it necessary to examine the sign of the factor multiplying both the circulating and trapped electron contributions to the growth rate. Specializing this factor to the first root, ω_1, it is seen that since $\omega_{*i} < 0$ (ω_{*i} is a signed quantity) the denominator of the electron coefficient is negative while the numerator is positive. Hence,

$$-\frac{\Delta_1^2\omega_i^2}{\tau[S_o\omega_{*i}\Delta_1^2 + S_1\Omega_i^2(\omega_{*i}-\Omega_i)]} > 0, \qquad (5.19)$$

for all values of magnetic field strength.

For the second root, ω_2, the situation is slightly different. Note that $\Delta_2 \propto (\Omega_i + \omega_{*i})$ which vanishes when $\Omega_i = -\omega_{*i}$. Hence, at least when $\Omega_i < -\omega_{*i}$, the sign of the electron coefficient is the same as found above for the first root. Equation (5.19) then also holds for the second root as long as $\Omega_i < -\omega_{*i}$. However, since Δ_2 can vanish, Eqn. (5.18) predicts stability for the ω_2 at large enough magnetic fields. Of course, the assumptions used to arrive at Eqn. (5.18) (namely Eqn. (5.2b)) are violated when $\Omega_i = -\omega_{*i}$, but a marginal stability point ($\gamma = 0$) is nevertheless also predicted from the full dispersion relation, Eqn. (4.43). This result enforces the notion that the simple dispersion relation predicts trends. Accurate calculation of the marginal stability

point for the second root requires the full dispersion but its existence is predicted by both dispersion relations.

The sign of the electron coefficient is then positive with the exception of the second root when $\Omega_i > -\omega_{*i}$, where the approximations break down. The sign of the factors inside the curly brackets then determine whether the contribution is stabilizing or not. The circulating electron contribution is as discussed above. Without collisions the circulating electrons are destabilizing. The effect of electron collisions is stabilizing when $\eta < 1$ and destabilizing when $\eta > 1$. This results from the presence of a temperature gradient without which ($\eta = 0$) electron collisions would always be stabilizing.

This leaves the trapped electron contribution to consider. First note that in the limit $\varepsilon \to 0$ the trapped electron contribution vanishes while the circulating electron term remains essentially unaltered. In the absence of collisions ($\nu_e = \nu_{ii} = 0$) the $\omega_{1,2}$ modes would both be destabilized by the circulating electrons alone (at least for $\Omega_i < -\omega_{*i}$). The trapped electron contribution is in general destabilizing (this will be discussed in more detail below). Thus, in a uniform magnetic field the instability should be observed. Altering the mirror ratio will modify the growth rate, but by itself the mirror ratio does not completely determine the stability of the mode. This is the reason for terming these instabilities trapped particle modified instabilities.

The trapped particle contribution may be broken into three terms (after Dixon[4]). One part contains the effect of the temperature gradient and the second contains the effect of finite gyroradius (or the effect of shifting the frequency below ω_{*e} for any reason whatsoever). The Maxwellian average may be written in the form

$$\mathrm{Im}\left\langle \frac{\omega + i\hat{\nu} - \omega_{*T}}{\omega - \langle k_y v_D \rangle_b + i\hat{\nu}} \right\rangle = \frac{\omega_{*e}}{\omega} [A_1 + A_2 + A_3] \tag{5.20}$$

where

$$A_1 = -\left(1 - \frac{\omega}{\omega_{*e}}\right) \mathrm{Im}\left\langle \frac{1}{B} \right\rangle, \tag{5.21a}$$

$$A_2 = -\eta\, \mathrm{Im}\left\langle \frac{v^2 - \frac{3}{2}}{B} \right\rangle, \tag{5.21b}$$

$$A_3 = \frac{\omega}{\omega_{*e}} \mathrm{Im}\left\langle \frac{i\hat{\nu}/\omega}{B} \right\rangle, \tag{5.21c}$$

where $v^2 = v^2/v_t^2$ is the normalized velocity and where

$$B = 1 + \frac{i\hat{\nu}}{\omega} - \frac{\langle k_y v_D \rangle_b}{\omega}. \tag{5.21d}$$

It is found that A_1 is the largest term of the three when $\omega < \omega_{*e}$ and is a destabilizing effect. A_2 follows in magnitude and can be either stabilizing or destabilizing depending on the magnitude of the normalized effective collision frequency, $\nu_e/2\varepsilon\omega$. Finally, A_3 is quite small in comparison to both A_1 and A_2 and can safely be neglected in computations of the growth rate. Figure 5-3 shows the relative magnitude of the three terms A_1, A_2, and A_3 versus the collision frequency parameter $\nu_e/2\varepsilon\omega$. It is easily seen that for the frequencies of interest the A_1 and A_2 terms are the most important.

In general, Eqn. (5.20) yields a net destabilizing effect over a wide range of collision frequencies. In the classic trapped particle instability predicted by Kadomstev and Pogutse[5] in which $\omega = \omega_{*e}$, growth resulted from the A_2 term only. This instability depends on both a temperature gradient and a velocity dependent collision frequency to achieve growth. However, these effects are not necessary for instability in general. As soon as the frequency shifts below ω_{*e}, the A_1 term will contribute to the growth of the mode even in the absence of a temperature gradient. Further, the velocity dependence is not needed either since the bracket in A_1 will average to a constant when all velocity dependencies are removed (as opposed to A_2 which vanishes when the velocity dependence of the collision frequency is removed). In this last case (in which the temperature gradient and velocity dependent collision frequency are removed) instability is achieved solely by a

Fig. 5-3. Relative magnitudes of A_1, (dotted curve), A_2, (dashed curve), A_3, (dot-dash curve), and the sum of the three (solid curve) versus the collision parameter $\nu_e/2\varepsilon\omega$. A_1 is seen to be always destabilizing (> 0) and larger than either of the other terms.

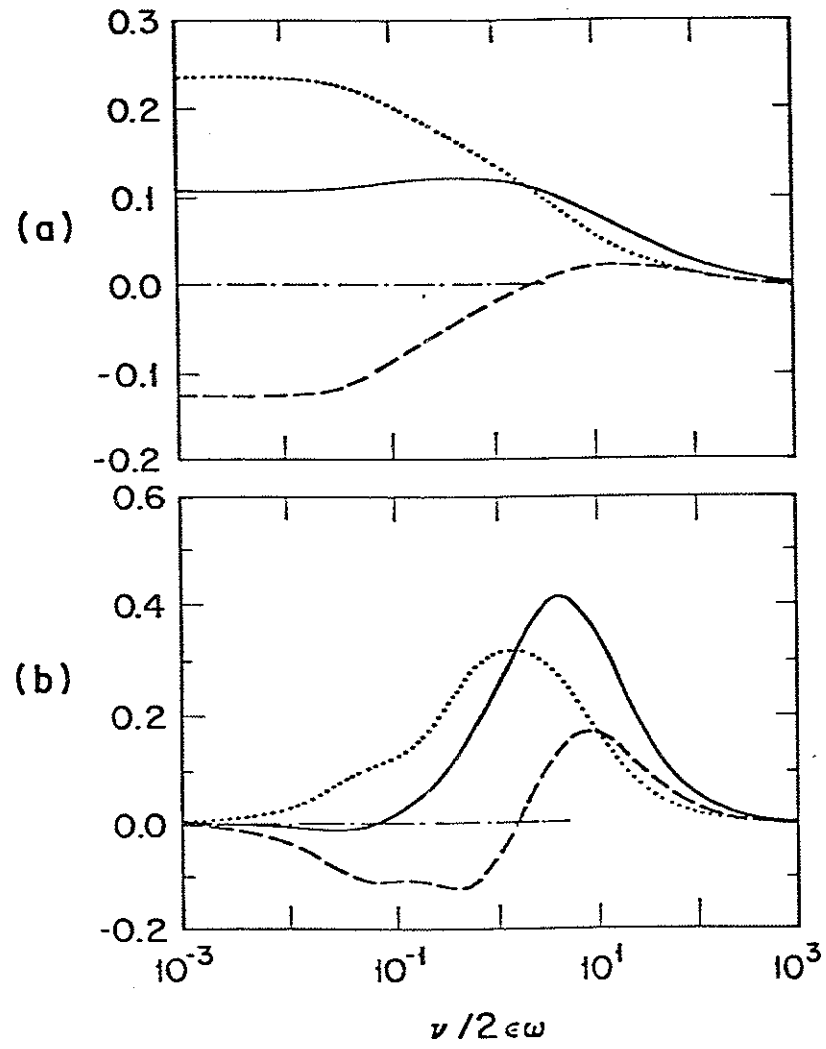

shift of the frequency to somewhere below ω_{*e}. A shift of the mode frequency to below ω_{*e} is actually a general criteria for instability of drift waves[6]. A mode destabilized by A_1 alone is far removed from the original instability first proposed by Kadomstev and Pogutse[5].

The electron drift wave can be destabilized by finite gyroradius effects which can shift the mode frequency well below ω_{*e}. In the case of the drift cyclotron instability the mode frequency is $\leq -\omega_{*i}$ which is a factor of $\tau = T_e/T_i$ below ω_{*e}. Hence, trapped particles tend to drive both these types of instabilities through both the A_1 and A_2 terms.

Finally, the topic of collisions, both ion-ion and electron neutral, remains to be considered. The results above indicate that ion-ion collisions are always stabilizing. This, however, is not the result obtained from more elaborate analyses. Rather, it is found that ion-ion collisions can be destabilizing[7,8] but for parameters typical of the Linear Multiple Mirror it is most likely that ion-ion collisions are stabilizing. Further, it is found that electron-neutral collisions are particularly effective at destabilizing the drift cyclotron instability[8] and since $\nu_{ii} \leq \nu_{en}$ the electron-neutral collisions are capable of cancelling out the stabilizing influence of the ion-ion collisions. The price paid to achieve these results is an exceedingly complicated derivation. The net result of the combination of ion-ion and electron-neutral collisions, when properly accounted for, is a destabilizing effect

(for parameters typical of the Linear Multiple Mirror). Therefore it is sufficient to carry out the analysis with no collisions (except by trapped particles) since this will lead to a pessimistic estimate of the growth rate. In subsequent references to theory no collisions (except those of trapped particles) will be included.

C. Experimental Results

This section is divided into two parts. The first presents the experimental results obtained at uniform field. In the next section the results of varying the mirror ratio are reported. Here trapped particles now play a role and modify the characteristics of the wave. The experimental results of both sections are also compared to the theory of Chapter IV.

1. Uniform Field Results

a. Experimental Observations

At low magnetic field strengths ($B \leq 100$ G) with a mirror ratio of unity a drift-type instability is observed. As the magnetic field strength is increased (at constant mirror ratio) an abrupt transition occurs to a second, distinct instability. The transition may be seen in Fig. 5-4 which shows the fluctuation amplitude as a function of the magnetic field strength. The transition is also apparent in Fig. 5-5 which is a plot of the measured mode frequency as a function of the magnetic field strength. The mode occuring for $B < 100$ G is characterized by a low fluctuation level and a frequency which decreases with increasing magnetic field strength.

Fig. 5-4. Fluctuation level versus magnetic field strength at constant mirror ratio (M = 1). An abrupt transition occurs at B = 100 G. Also shown is the predicted growth rate (in arbitrary units) of the $-\Omega_i$ cyclotron mode corrected by the experimental value measured value of the Doppler shift.

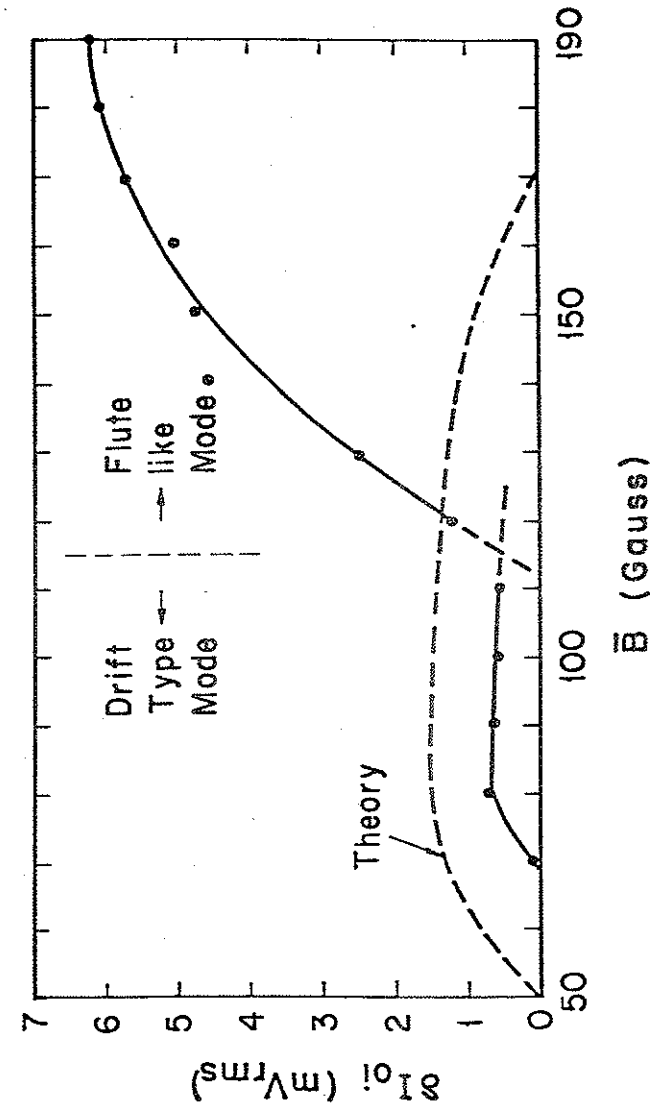

Fig. 5-5. Mode frequency versus magnetic field strength at constant mirror ratio (M = 1). The transition between modes seen in Fig. 5-1 is also evident in this plot. Also shown is the theoretically predicted mode frequency of the $-\Omega_i$ cyclotron mode corrected by the experimentally measured Doppler shift.

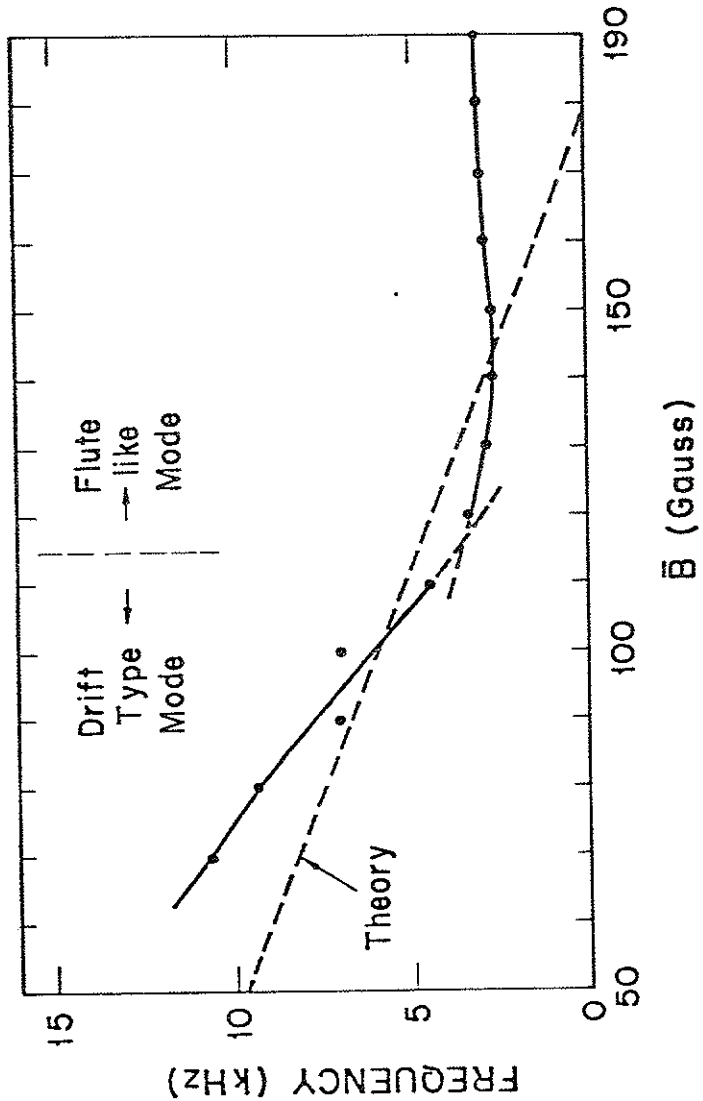

In addition to the transition the two modes are further distinguished from one another by different values of k_ℓ and by distinct radial profiles of the fluctuation level. The mode found for B < 100 G has a finite k_ℓ with $\lambda_\ell = 2\pi/k_\ell$ = machine length. The mode found above 100 G is a flute mode. Figure 5-6 shows two pairs of ion saturation current traces used to determine the k_ℓ of the observed waves. The probes used to measure the saturation current were located (refer to Fig. 2-1) i) above the 6" diffusion pump, ii) at the center of the tank and, iii) at the end of the tank. Figure 5-6a corresponds to the low field mode. In this case trace i) is 180° out phase with the signals of probes ii) and iii) which indicates an axial phase inversion and thus a finite k_ℓ. Figure 5-6b corresponds to the high field mode. Here, all the probe signals are in phase and of the same magnitude, which indicates a flute-type perturbation. Figures 5-7 and 5-8 show radial profiles of the fluctuation levels of the modes found below and above 100 G respectively. The lower field mode amplitude peaks at about r = 2 cm while the higher field mode peaks at about r = 4 cm. the magnitude of the fluctuation levels differ by over a factor of 10.

For the above reasons the two modes are regarded as physically distinct entities. Attention will now be focused on the mode which occurs below 100 G. All other data shown in this section will refer only to this instability.

Fig. 5-6. Two pairs of ion saturation signals from probes located i) above the 6" diffusion pump, ii) at the center of the tank and, iii) at the end of the tank. a) Signals for the low field mode indicate a finite k_ℓ while those for the high field mode, b), indicate a flute-type perturbation.

Fig. 5-7. Radial profiles of fluctuation level of mode found below 100 G. This instability has a relatively small fluctuation level with a peak amplitude occuring at r ≈ 2 cm.

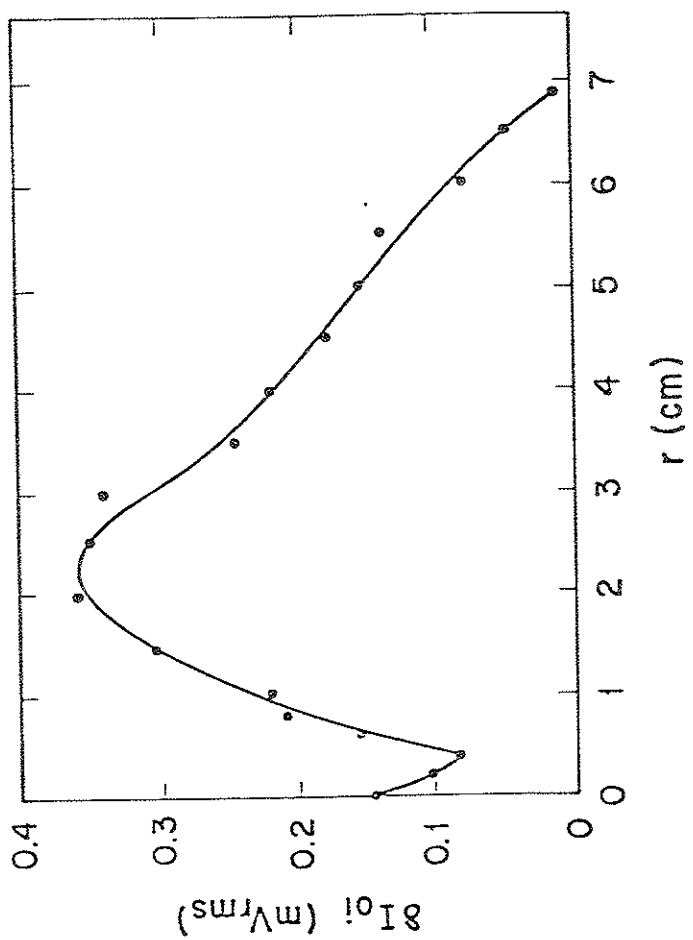

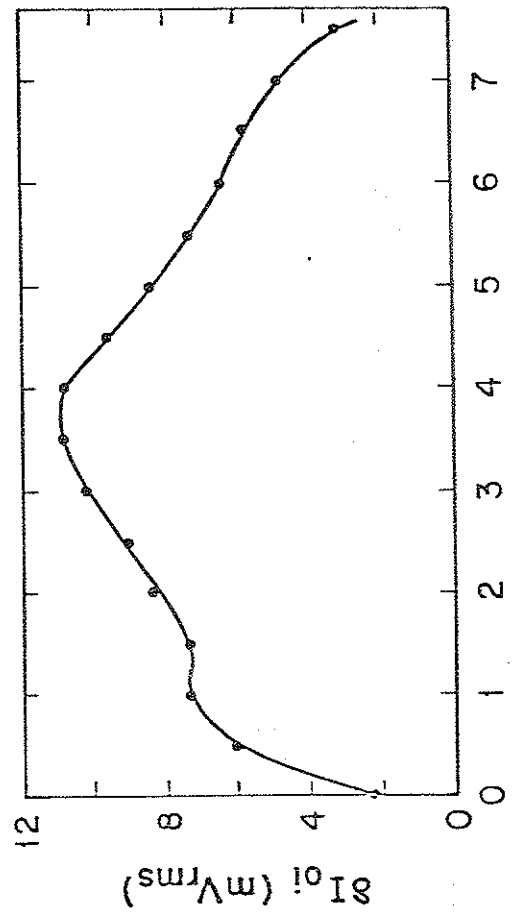

Fig. 5-8. Radial profile of fluctuation level of mode found above 100 G. The fluctuation is much larger than that of the mode shown in Fig. 5-6 and peaks further out in radius.

Figure 5-9 shows radial profiles of temperature and density. Clearly there are gradients in both these quantities. By comparing Fig. 5-9 to Fig. 5-7 the peak fluctuation level is seen to occur near the region of steepest density gradient. However, the same region shows only a small to moderate gradient of the electron temperature.

Other measured wave properties are listed in Table 5-1. Items 1 through 5 of this table suggest that the plasma should be strongly unstable to drift-type oscillations. A heuristic argument based on the results of theory would predict that the mode amplitude should peak in a region of steep density gradient because the growth rate is proportional to ω_*. Also, the peak amplitude should occur away from regions of steep temperature gradients since this is a stabilizing influence ($\eta = 0$ is the most unstable situation for non-trapped particle modes). This is precisely what the observed peak fluctuation level does. While this is clearly not a proof, the above argument does support the notion that the instability is a type of drift wave.

Finally, item 6 of Table 5-1 implies that the ion cyclotron frequency may not be neglected in any theory developed to describe the instability. Condition 6 is what gives rise to the drift cyclotron instability. Thus the drift cyclotron wave must be considered as a possible candidate for what the observed instability might be.

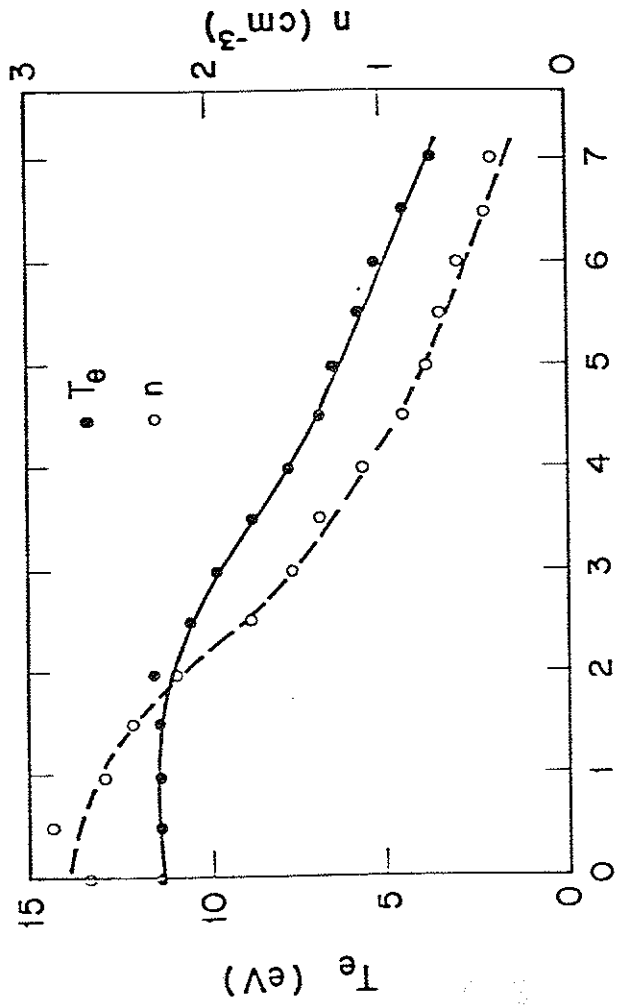

Fig. 5-9. Radial profiles of temperature and density.

Table 5-1.

1. Finite $k_\parallel$. ($\lambda_\parallel$ = 2.1 m = machine length)

2. $v_{te} \gg \frac{\omega}{k_\parallel} \gg v_{ti}$.

3. Propagation in the electron diamagnetic direction.

4. $\omega < \omega_{*e}$.

5. Azimuthal mode number of 2 with $k_\perp \rho_i \cong 1$.

6. $\Omega_i < \omega_{*i}$.

One final experimental observation is that a steady state radial electric field exists in the plasma. This gives rise to a Doppler shift of the mode frequency which must be taken into account when making comparisons between theory and experiment. Figure 5-10 shows the measured ExB drift velocity as a function of the magnetic field strength. It is seen to be constant over the range of magnetic field strengths in which the instability is observed.

b. Comparison of Experiment to Theory

In this section the experimental observations will be compared to the predictions of theory. A correspondence will hopefully be established between one of the theoretically predicted instabilities and the observed instability. Plots derived from theory used for the purpose of comparison are obtained from the full dispersion relation given by Eqn. (4.43) rather than from the approximate results of section B of this chapter.

Of the three modes predicted by theory only one has a frequency which decreases with increasing magnetic field strength. This holds true whether an ExB drift is included in the analysis or not. The mode which has this behaviour is the $-\Omega_i$ drift cyclotron branch. For purposes of comparison Fig. 5-5 shows also shows the predicted mode frequency corrected by the experimentally measured value of the Doppler shift from the ExB drift. The agreement is quite good. Without a Doppler shift the mode is predicted to propagate in the ion diamagnetic direction, but when the Doppler shift is included

Fig. 5-10. ExB drift velocity as a function of magnetic field strength. The drift velocity is constant over the range of magnetic field strength which the low field mode is observed.

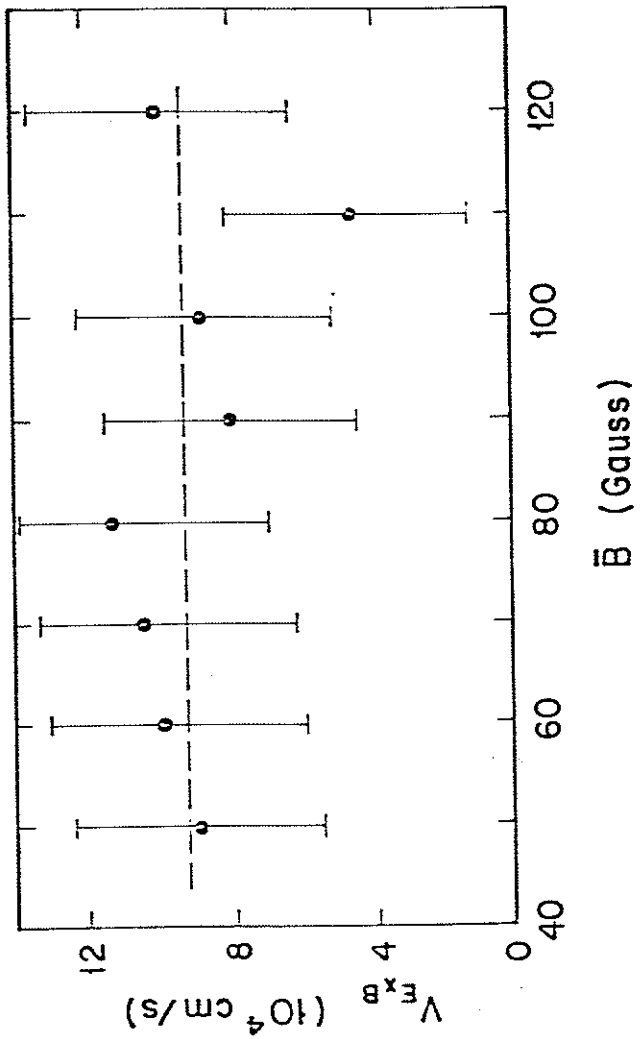

the direction of propagation is in the electron diamagnetic direction which is in agreement with experiment.

The electron drift branch can be eliminated as a candidate on two counts. First, the frequency is predicted to increase strongly with increasing magnetic field strength, contrary to the experimental results. Second, the predicted frequency is an order of magnitude larger than the observed frequency and when corrected for the Doppler shift it is moved even further from the observed frequency. For these reasons the electron drift wave will be excluded from further consideration.

The third candidate is the $+\Omega_i$ drift cyclotron wave. It is subject to the same criticism as the electron drift branch although the predicted frequency is much closer to the experimentally measured frequency than the electron drift wave.

Based essentially on a process of elimination, the only predicted instability which is in agreement with all the experimental facts is the $-\Omega_i$ drift cyclotron branch. There is no apparent way to reconcile either of the other two predicted modes with the fact that the measured frequency decreases with increasing magnetic field strength, even though both the other modes are predicted to unstable and to propagate in the appropriate direction.

One other comparison that can be made is between the saturated fluctuation level and the linear growth rate. According to strong turbulence theory[9,10] a linear relationship exists between the linear growth rate and the saturated fluctuation level. While

perhaps this is not the strongest possible evidence for mode identification it does provide at the very least a consistency check. The results of this comparison can be seen by reference back to Fig. 5-4. In addition to the experimental data, a curve labeled "theory" is also plotted. The scale of the theory curve is arbitrary. There is qualitative agreement between theory and experiment in that the fluctuation level is small, decreases slightly with increasing magnetic field strength, and that the mode is ultimately stabilized at high enough magnetic field strengths. These are the trends predicted from theory. If the same comparison is made with the predicted growth rate of the $+\Omega_i$ drift wave there is disagreement in that the predicted growth rate increases strongly with increasing magnetic field strength with no stabilization of the mode.

The strongest evidence presented in favor of the $-\Omega_i$ drift cyclotron instability is the dependence of the frequency on the magnetic field strength. While perhaps not totally conclusive by itself, a number of other facts are in support of the identification of the experimentally observed instability as the $-\Omega_i$ drift cyclotron mode predicted from theory. These facts are the agreement between the predicted and measured direction of propagation and the appropriate scaling of the fluctuation level with the linear growth rate. Also, theory predicts a critical magnetic field for which stability is achieved which is in qualitative agreement with the fact that the mode stabilizes, although experimentally it is unclear

whether the mode actually stabilizes or is simply swamped out by the flute mode at higher magnetic field strengths.

2. Trapped Particle Effects

Trapped electrons primarily influence the growth rate of the instability and only sightly influence the real frequency of the mode. For small enough mirror ratios the trapped electrons constitute a perturbation to the uniform field results. The effect of the presence of the trapped electrons is expected to be small for this reason.

The general results predicted from theory are that the mode frequency and to a lesser extent, the growth rate, are weak functions of the mirror ratio. The trends observed in the measured frequency and fluctuation level are in qualitative agreement with these predictions.

Figure 5-11 shows the measured frequency as a function of the magnetic field strength for several values of the mirror ratio. A nearly linear decrease with increasing magnetic field strength is observed for each value of the mirror ratio. Another clear trend is that the frequency decreases slightly with increasing mirror ratio. This is more clearly seen in Fig. 5-12 which shows the measured frequency as a function of the mirror ratio for two values of the magnetic field. The decrease in frequency with both increasing magnetic field and increasing mirror ratio are evident. The dependence of frequency on the mirror ratio is weak. The frequency

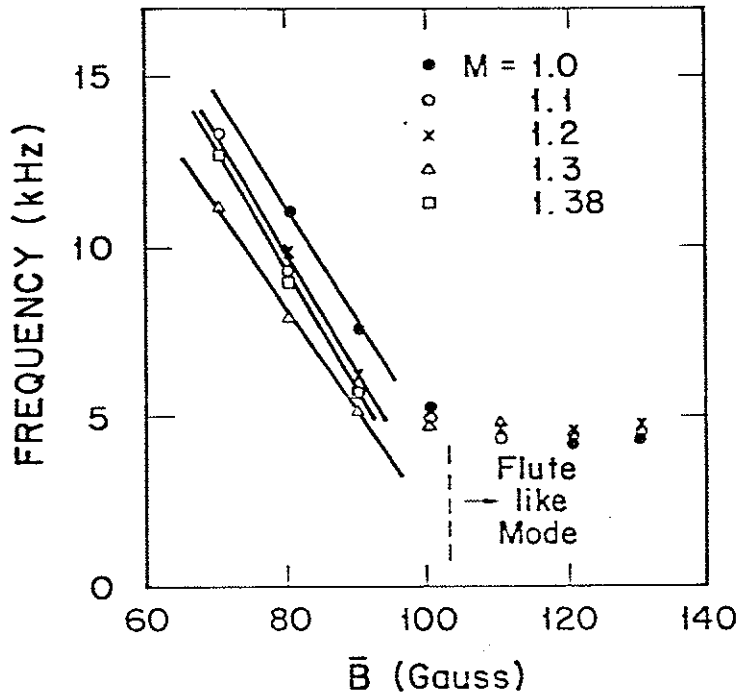

Fig. 5-11. The measured frequency as a function of the magnetic field strength for several values of the mirror ratio.

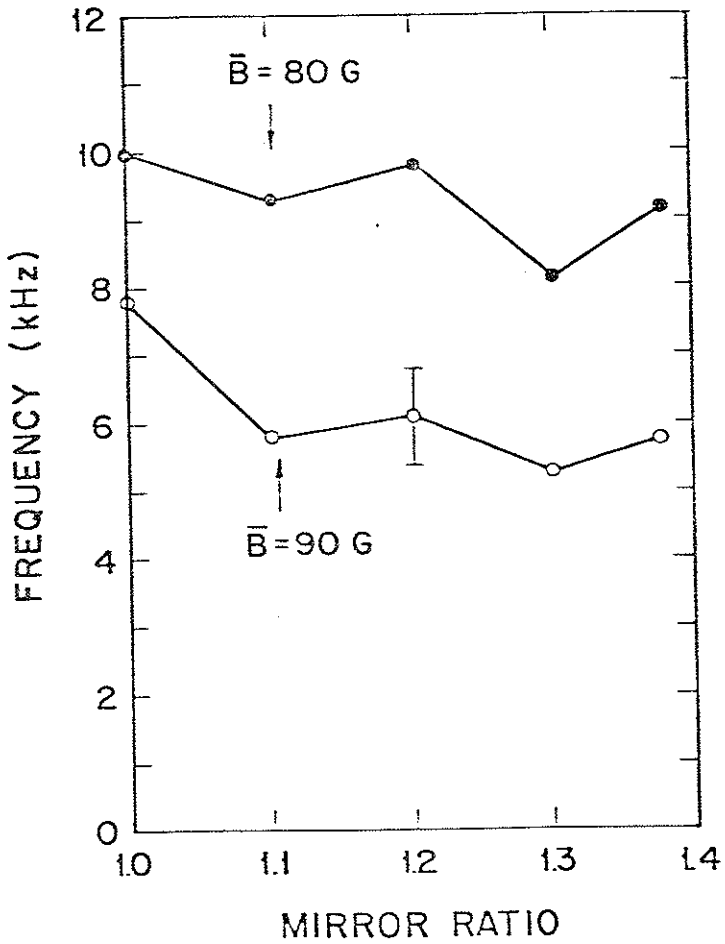

Fig. 5-12. The measured frequency as a function of the mirror ratio for two values of the magnetic field strength.

changes by about 1-2 kHz as the mirror ratio is varied from 1.0 to 1.4.

The last trend is predicted by theory. Figure 5-13 shows the predicted frequency of both the $+\Omega_i$ and $-\Omega_i$ modes (corrected by the experimentally measured value of the Doppler shift) as a function of the mirror ratio. The predicted frequency variation is rather weak, being on the order of 0.5 kHz (note the scale on the frequency axis). This holds for both the $+\Omega_i$ and $-\Omega_i$ modes. The predicted effect of the trapped electrons is both small and nearly identical for the two cyclotron waves. The trapped electrons apparently do not provide a means to discriminate between the two modes.

Figure 5-14 shows the fluctuation level as a function of the mirror ratio for two values of the magnetic field strength. The observed trend is that the fluctuation level increases quickly at low mirror ratios ($M < 1.1$) and levels off at higher mirror ratios. The agreement with theory in this case is only partial as may be seen by reference to Fig. 5-15 which shows the linear growth rate for both the $+\Omega_i$ and $-\Omega_i$ modes as a function of the mirror ratio. The growth rate initially increases rapidly with the mirror ratio as the measured fluctuation level does. However, the growth rate peaks and ultimately decreases with increasing mirror ratio in contrast to the fluctuation level which remains nearly constant.

Fig. 5-13. Predicted frequency as a function of the mirror ratio for the a) $+\Omega_i$ and b) $-\Omega_i$ modes. The basic trend in both cases is a frequency which decreases with increasing mirror ratio.

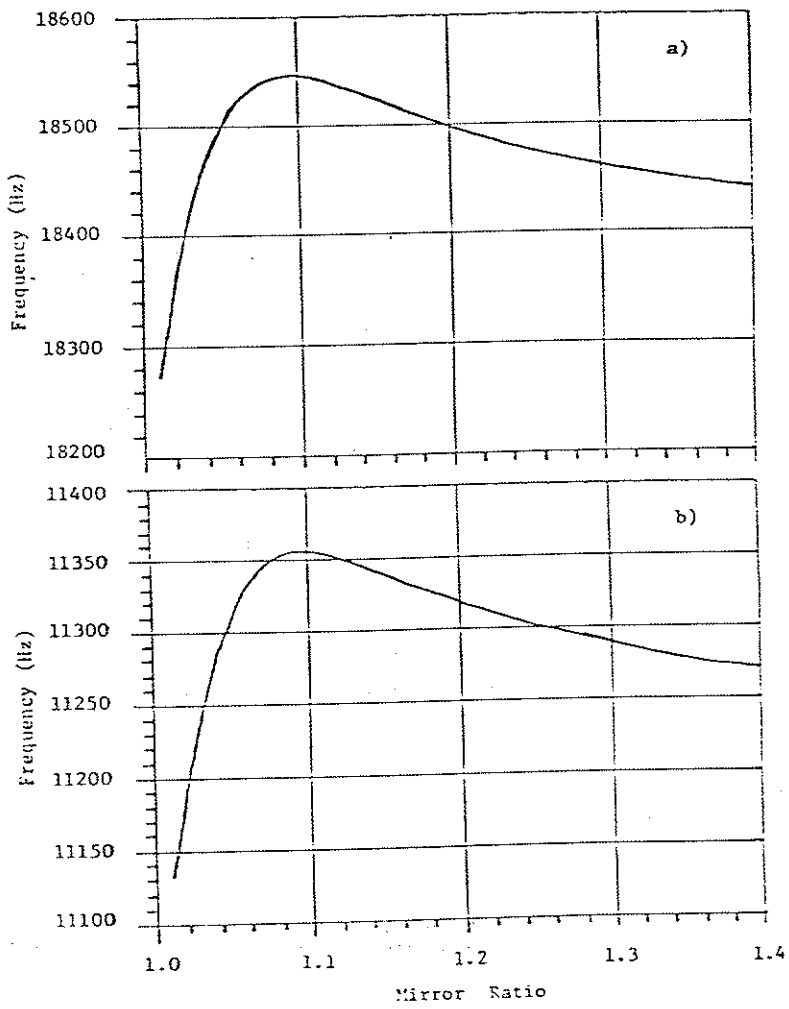

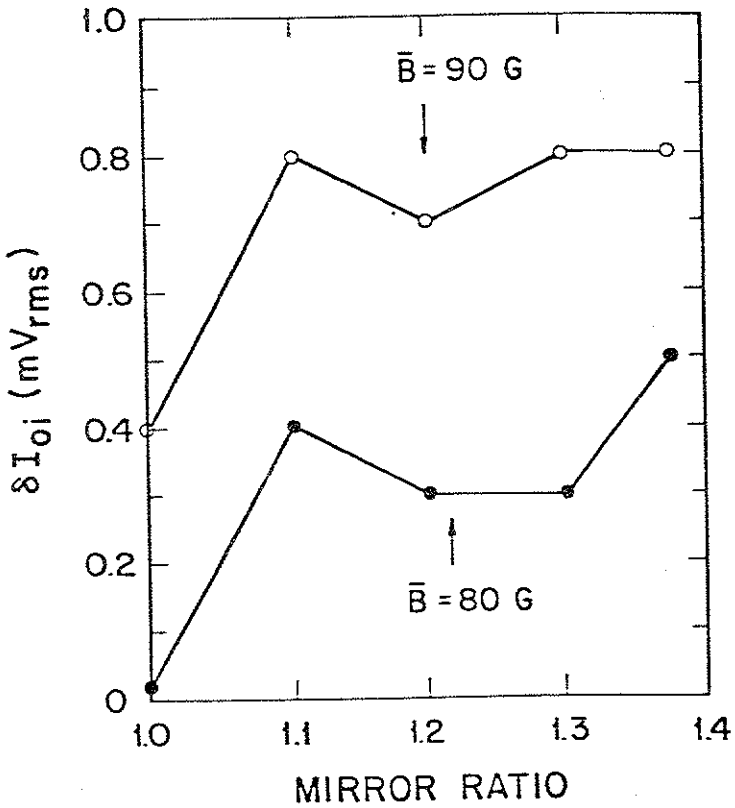

Fig. 5-14. The fluctuation level as a function of the mirror ratio for two values of the magnetic field strength.

Fig. 5-15. The predicted growth rate as a function of the mirror ratio for the a) + Ω_i and b) - Ω_i modes.

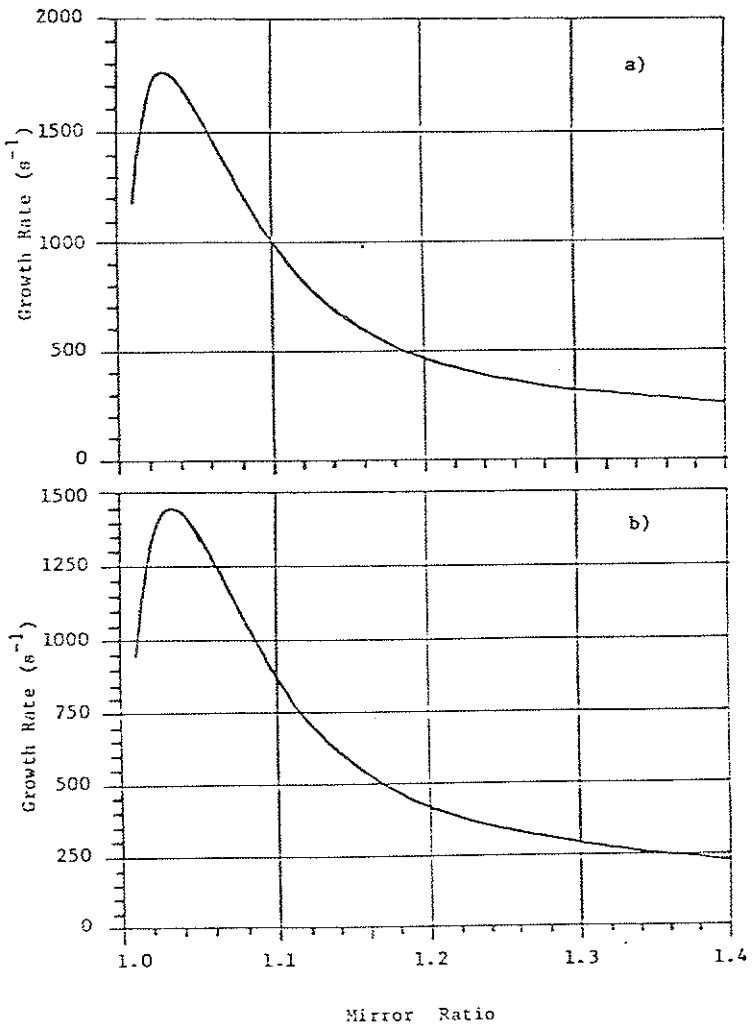

Note again that the growth rates of both the + Ω_i and - Ω_i modes are very similar in their dependence of the mirror ratio (but differ in magnitude of the frequency). This apparently results from the weak dependence on ω of the trapped particle contribution to the growth rate. This is especially true for the case of Doppler shifted mode frequencies which are positive for both the + Ω_i and - Ω_i modes. In this case the frequencies of both cyclotron modes are similar in magnitude. In addition, $\omega/\omega_{*e} \ll 1$ which eliminates much of the dependence on the mode frequency itself. The net result is that the contribution to the growth rate by the trapped electrons does not depend on the mode frequency and hence is the same for both of the cyclotron modes.

D. Discussion and Conclusions

Theory predicts three modes to be unstable over the range of magnetic field strength and mirror ratio for which a drift wave is experimentally observed. Of the three predicted modes only one is in agreement with a majority of the experimental measurements made in both uniform and nonuniform magnetic fields.

Only one predicted instability has a frequency which decreases with increasing magnetic field strength. This mode is the - Ω_i Doppler shifted drift cyclotron instability. In addition to the having the appropriate scaling of frequency with magnetic field strength there is agreement between theory and experiment with respect to the direction of propagation and the scaling of the

linear growth rate with the saturated fluctuation level in both uniform and nonuniform field configurations. Less direct, but still supportive is the fact that the mode stabilizes at or below the critical magnetic field predicted from theory.

With respect to mirror ratio there is basic agreement between theory and experiment. The predicted and measured mode frequencies both decrease slightly with increasing mirror ratio and are of a similar magnitude. The predicted growth rate and measured fluctuation level are in only partial agreement. There is agreement at low mirror ratio ($M < 1.1$) but disagreement at larger mirror ratios where the fraction of trapped particles can be substantial ($\sqrt{2\varepsilon} = 0.5$ at $M = 1.4$). At large mirror ratios the trapped particles are no longer a perturbation and the tacit assumption $\varepsilon \ll 1$ is violated. The disagreement between theory and experiment at large mirror ratios is not looked upon as a serious discrepancy.

All these experimental observations are consistent with only the $-\Omega_i$ drift cyclotron mode. No one correspondence between theory and experiment is completely convincing, but all the data taken together make a strong case for the identification of the observed instability as a Doppler shifted ion cyclotron mode.

Experimentally, the drift cyclotron mode appears to be more difficult than most to "pin down." This results from the real frequency being very nearly equal to a harmonic of the ion cyclotron frequency, $\pm n\Omega_i$. There are only two experimentally variable parameters in Ω_i, the magnetic field (which has been reported on)

and the ion mass. The ion mass can be varied by using different gases but care must be taken in the choice of gas. If molecular gases are used the ratio of ionized molecules to ionized atoms must be known in order to compute an average ion mass. The determination of this ratio is difficult. This problem may be circumvented by the use of monatomic gases. In particular, experiments of the Linear Multiple Mirror have been confined to the noble gases helium, neon, and argon.

Helium is not useful in directly verifying the properties of the drift cyclotron instability because the condition $\Omega_i < -\omega_{*i}$ can only be met at unreasonably low magnetic field strengths. The observation that no mode observed in helium corresponds to the instability seen in neon does provide yet more indirect evidence for the identification of the neon mode as the drift cyclotron instability.

In the direction of higher mass, argon may be used. The problems now are that of large gyroradius and the ion cyclotron frequency being so low as to make the theory invalid. There then appears to be no simple, direct, and unambiguous method of varying the mode frequency besides varying the magnetic field strength.

All other parametric dependencies arise through the growth rate of the instability. Here again direct evidence is not easy to obtain. To make comparisons at all, strong turbulence theory must be invoked in the form of assuming that the linear growth rate is

proportional to the saturated fluctuation level. This is neither easily justified nor verified.

One perplexing result that remains unexplained is that theory predicts three unstable modes but only one mode is experimentally observed. A strictly speculative argument for this result involves collisions which were neglected in the theory. The neglect of collisions was based on the argument that the strong destabilizing influence of the electron-neutral collisions was offset by the stabilizing influence of ion-ion collisions. Since $\nu_{en} > \nu_{ii}$ it was assumed that to first order the two effects cancelled. The theory on which this is based was developed for the $-\Omega_i$ mode only. It is not known whether it also holds for the $+\Omega_i$ mode of for the electron drift wave. Fluid theory predicts that electron-neutral collisions are a stabilizing influence on ordinary drift waves and thus collisions could completely damp out the electron drift wave. The proper treatment of collisions is difficult and for this reason it has been sidestepped in the above theory with a resulting increase in the ambiguity of the results.

Despite these shortcomings it is believed that a strong case has been made for the identification of the observed instability as a Doppler shifted ion cyclotron mode.

References

1. D.P. Grubb and G.A. Emmert, Phys. Fluids 22, 770 (1979).
2. D.P. Grubb and G.A. Emmert, Phys. Fluids 22, 1825 (1979).
3. M.A. Makowski and G.A. Emmert, Bull. Am. Phys. Soc. 25, 844 (1980).
4. D.P. Dixon, Ph.D. thesis, Columbia University, (1977).
5. B.B. Kadomstev and O.P. Pogutse, Sov. Phys. JETP 24, 1172, (1967).
6. A.B. Mikhailovskii, Reviews of Plasma Physics, M.A. Leontovich, Ed., Consultants Bureau, New York, Vol. 3 (1967).
7. A.A. Rukhadze and V.P. Silin, Sov. Phys. USPEKHI 11, 659 (1969).
8. O.P. Pogutse, Sov. Phys. JETP 20, 630 (1965).
9. B.B. Kadomstev and O.P. Pogutse, Reviews of Plasma Physics, M.A. Leontovich, Ed., Consultants Bureau, New York, Vol. 5 (1970).
10. T.H. Dupree, Phys. Fluids 10, 1049 (1967).

VI. OTHER OBSERVATIONS

In this chapter the observations of a low frequency instability in a helium plasma are reported. This is in contrast to the results of the previous chapter which were obtained with a neon plasma. The low frequency instability was one of the motivations for switching to neon as discussed in the previous chapter.

The basic observation is that two drift waves with frequencies within 20% of one another are observed to be simultaneously unstable under the same plasma parameters (see Fig. 5-1). The modes are distinct below a critical magnetic field strength. By varying the mirror ratio and magnetic field strength the frequencies of the two modes can be made to coalesce. As the critical magnetic field is exceeded the two modes again separate in frequency, but in addition, a large amplitude low frequency (< 1 kHz) flute type mode is also observed. Previous to coalescence the two drift waves maintained distinct radial profiles of fluctuation level, having different relative amplitudes and peaking at different radii. After coalescence, the radial profiles of the fluctuation level of the two drift waves was nearly identical in both amplitude and structure.

Low frequency modes have previously been studied in the Linear Multiple Mirror[1] but in a slightly different context. Low frequency oscillations were observed to occur in the presence of two trapped particle modes of different azimuthal mode numbers. This occured at magnetic fields in the range of 200-300 G. In contrast, the present

study works at lower magnetic fields (80-150 G) and where only one of the modes is found to be a trapped particle mode. Here the low frequency mode does not appear to result from a coupling of modes of different azimuthal mode numbers but rather is due to a coupling of a drift and trapped electron mode of the same mode number ($m = 1$). The two cases are similar in some respects. First, the the low frequency oscillations arise only when the frequencies of the two drift waves are close enough to one another. Second, in both cases, the low frequency mode is observed to be flutelike ($k_{\parallel} = 0$).

A. Observations of Drift Waves

As mentioned above, at low enough magnetic field strengths the plasma is initially observed to be unstable to two distinct drift waves. A brief description of the properties of these two drift modes will now be given.

1. Trapped Electron Drift Mode

The trapped electron mode reported here was first observed by Grubb[2]. The identification of this mode as a trapped electron instability follows from the close agreement between the experimental observations reported by Grubb and those seen in this series of experiments.

Figure 6-1 shows the fluctuation amplitude of the trapped electron mode versus mirror ratio at constant magnetic field strength. It is seen that the fluctuation level is a strong function of the mirror ratio and vanishes at a mirror ratio of 1.0

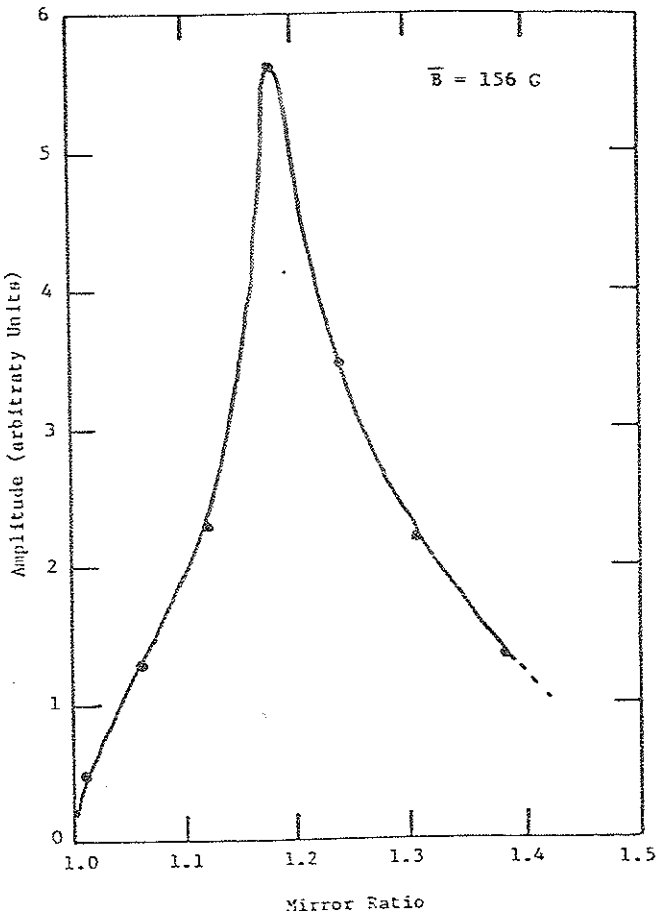

Fig. 6-1. Amplitude of the trapped electron mode as a function of the mirror ratio at constant magnetic field strength. The peak in amplitude corresponds to the coalescence of the trapped electron and dissipative drift waves.

(i.e. at uniform field). The large peak in the graph occuring at M = 1.18 is due to the coalescence of the two drift waves. Of course at the point of coalescence the two modes are indistinguishable so that attributing the amplitude peak to one or the other of the two drift waves should not be taken too literally.

The measured frequency and fluctuation level as a function of the magnetic field strength are shown in Figs. 6-2 and 6-3 respectively. Note that in the range of magnetic field strengths from 100-150 G the mode frequency increases by about 5 kHz. The change in frequency of this mode with magnetic field leads to the coalescence of the two modes since the frequency of the second drift wave does not change as the magnetic field strength is varied. The trapped electron mode has an azimuthal mode number of 1 and rotates in the direction of the electron diamagnetic current. The observations made here agree well with those made by Grubb on the trapped particle drift wave.

2. Dissipative Drift Wave

The second mode of interest is the dissipative drift wave. It is distinct from the trapped electron drift wave since it exists in a uniform magnetic field where the trapped electron mode vanishes. The dissipative mode possesses a finite $k_{\parallel}$ with $\lambda_{\parallel} = L$ = machine length. The phase velocity of the wave satisfies the drift wave condition $v_{ti} < \omega/k_{\parallel} < v_{te}$ and for this reason has been termed a

Fig. 6-2. Measured frequency of the trapped electron drift wave as a function of the magnetic field strength. Between $\bar{B}$ = 100 G and $\bar{B}$ = 150 G the frequency of the mode changes rapidly.

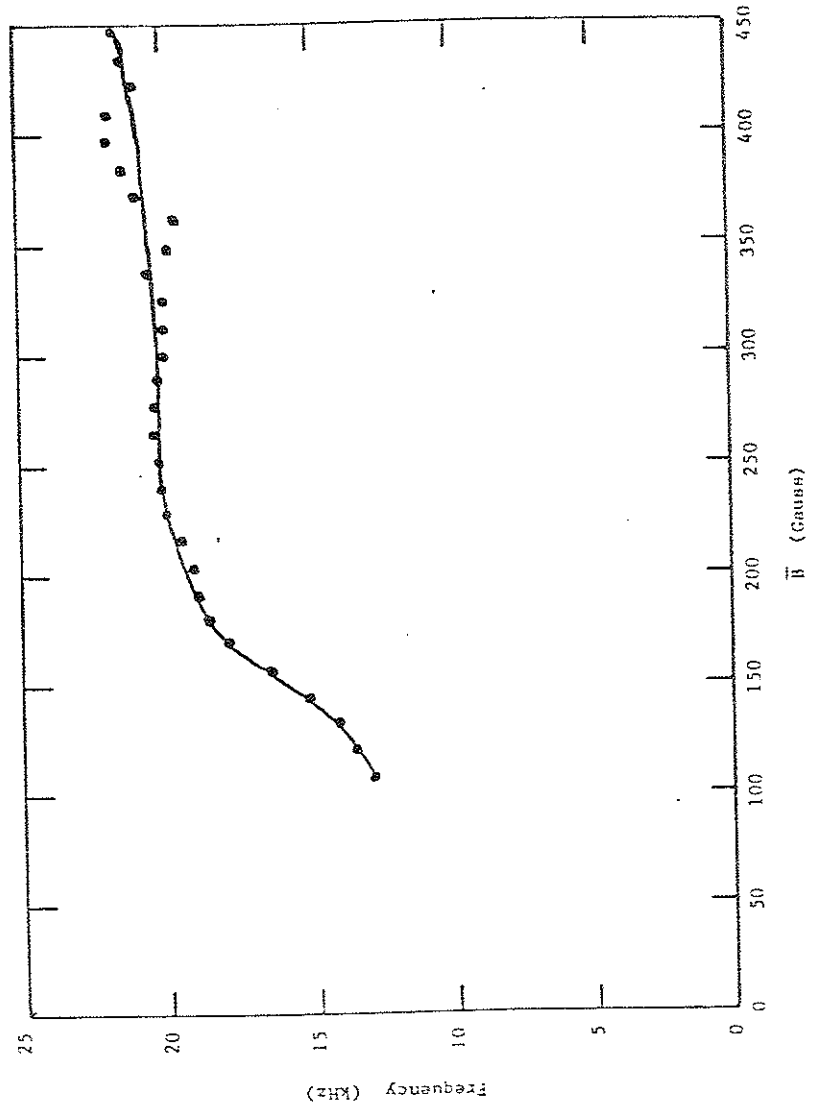

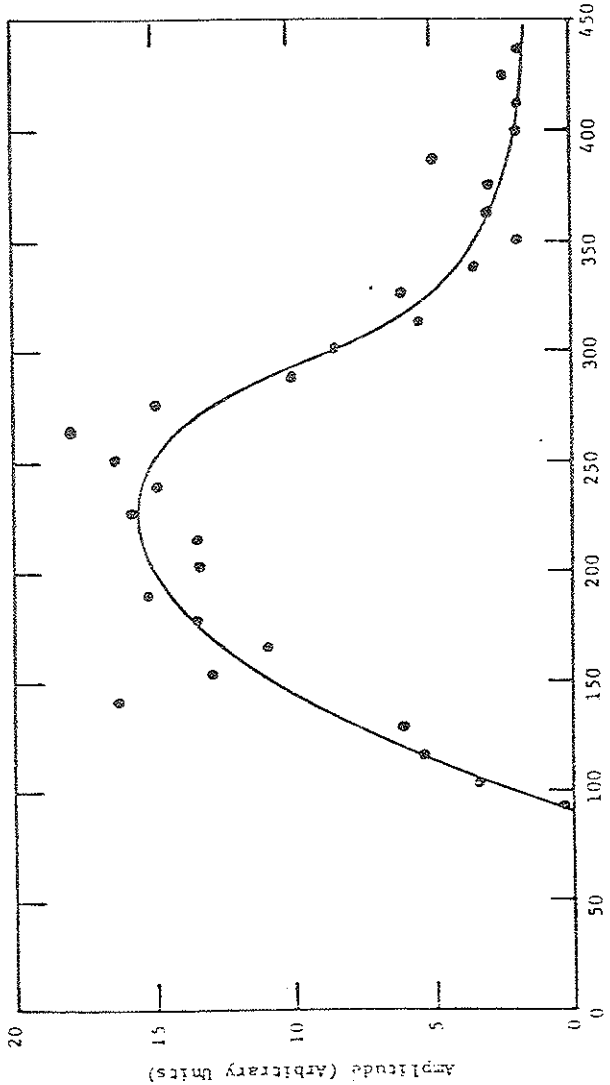

Fig. 6-3. Fluctuation level of the trapped electron mode as a function of the magnetic field strength.

drift wave. The wave possesses an azimuthal mode number of 1 and rotates in the direction of the electron diamagnetic current.

The dissipative nature of the mode has been confirmed using a technique called transfer function analysis[3,4]. In this method the plasma is essentially treated as a circuit element with unknown gain and phase characteristics as a function of frequency. The gain and phase characteristics are determined by the dielectric response function of the plasma. Figure 6-4 shows how these characteristics are experimentally probed. A signal is applied to the input of the circuit and into the reference channel of a lock-in amplifier. When the plasma is marginally stable to the particular mode of interest the response of the plasma to the applied signal will be indicative of the type of instability present. The response is measured by taking the output and feeding it into the second channel of the lock-in amplifier.

Instabilities are classified as either reactive or dissipative depending on whether the zero of the dielectric function to which the instability corresponds is one of a pair of conjugate complex roots (reactive instability) or is not one of a pair of conjugate roots, i.e. occurs as an isolated root (dissipative instability). Physically, the classification is based on the method by which the instability taps energy from the plasma. In a reactive instability the conjugate roots have the same real frequency but one is stable and the other is unstable. One of the roots is a postive energy wave and the other is a negative energy wave. Energy is dissipated

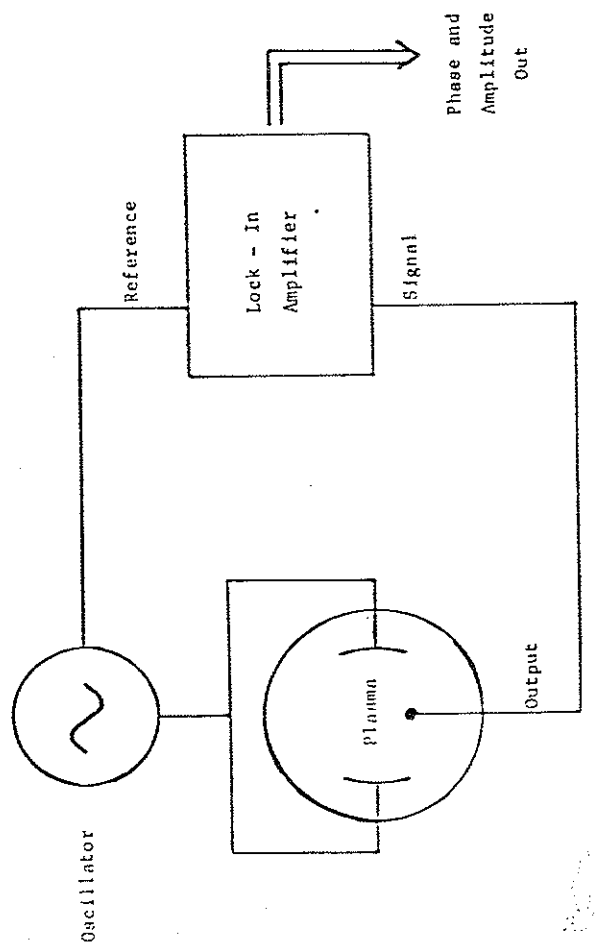

Fig. 6-4. Schematic of circuit used of obtain the transfer function of a marginally stable plasma.

(and one of the modes destabilized) by transfering energy from the positive energy wave to the negative energy wave. In the case of a dissipative wave the energy sink results from true dissipation of plasma energy by some physical process such as collisions.

The experimental technique for determining the transfer function is to measure the amplitude and phase of the output relative to applied input signal as a function of the frequency of the applied signal. For damped modes the transfer function will show a peak at each zero of the dielectric function. In the case of a dissipative instability the transfer function analysis shows a peak at the zero of the dielectric function and an asymptotic phase change of 180°. For a reactive instability a peak is also observed but the asymptotic phase change is 360°.

At uniform field the magnetic field strength was lowered until the fluctuation level of drift wave vanished. At this point an m = 1 sinusoidal signal was applied to the plasma by means of a pair of grids and the response of the plasma was measured with a Langmuir probe biased to collect ion saturation current. The phase and amplitude of the detected signal were measured with respect to the applied signal by means of a lock-in amplifier. The result is shown in Fig. 6-5. Here the phase and amplitude of the detected signal are plotted as a function of the applied frequency. The total phase shift across the mode is ~ 180° while that across the -3 db points of the amplitude curve is ~ 105°. Theory would predict a 180°

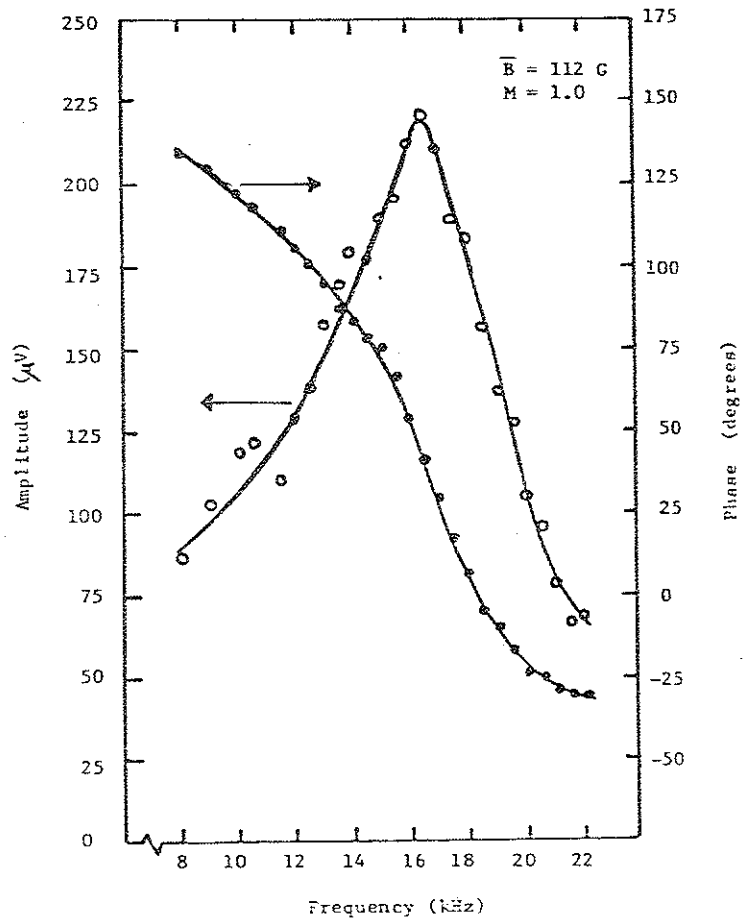

Fig. 6-5. Phase and amplitude of the detected signal relative to the reference signal as a function of the frequency of the reference signal.

asymptotic phase shift and a 90^{o} phase shift across the -3 db points.

Further, the mode frequency and amplitude are dependent upon the background neutral pressure. This indicates a dependence on the electron-neutral collision frequency which would also lead one to conclude that the wave is dissipative.

B. Observation of the Low Frequency Mode

Figure 6-6 depicts the mirror ratio (M), and average magnetic field strength ($\bar{B}$) parameter space for the data presented below. The data were taken by varying only $\bar{B}$ and M and holding all other parameters constant.

At point A of Fig. 6-6 the plasma is unstable only to the dissipative drift wave. Figure 6-7 shows the radial profiles of the fluctuation level in the ion saturation current, δI_{oi}, and the fluctuation level normalized to the ion saturation current, I_{oi}, for parameters corresponding to point A of Fig. 6-6. At this point neither the trapped electron nor the low frequency mode are present, but as one proceeds along a line from A to D in Fig. 6-6 (i.e. as one changes the mirror ratio holding the magnetic field constant) the amplitudes of both the trapped electron and low frequency modes increase.

At lower magnetic fields (point B of Fig. 6-6) there are two drift waves: the trapped electron and dissipative modes. Figure 6-8 shows the radial profiles of the fluctuation levels of both these

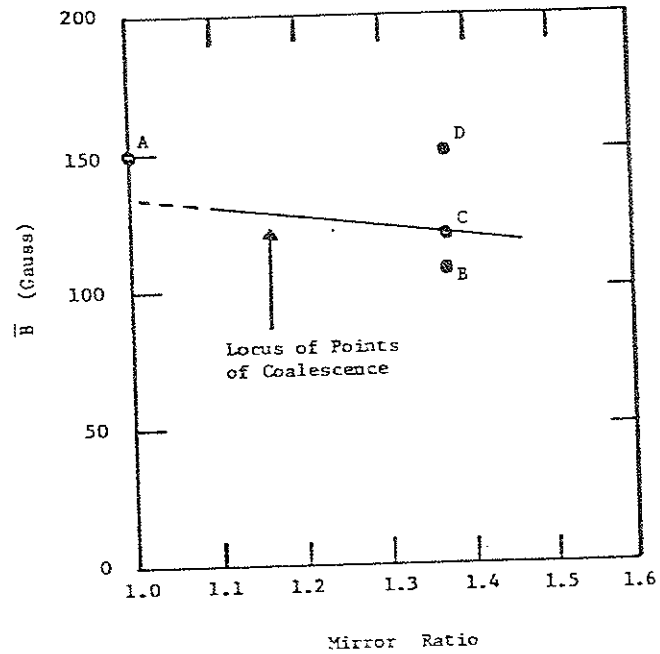

Fig. 6-6. Schematic of the mirror ratio - magnetic field strength parameter space showing the points where the dissipative drift wave is alone unstable (A), the two drift waves are unstable (B), coalescence occurs (C), and where the low frequency mode is strongly unstable (D).

Fig. 6-7. Profiles of the fluctuation level and the fluctuation level normalized to the ion saturation current for the dissipative drift wave for parameters corresponding to point A of Fig. 6-6.

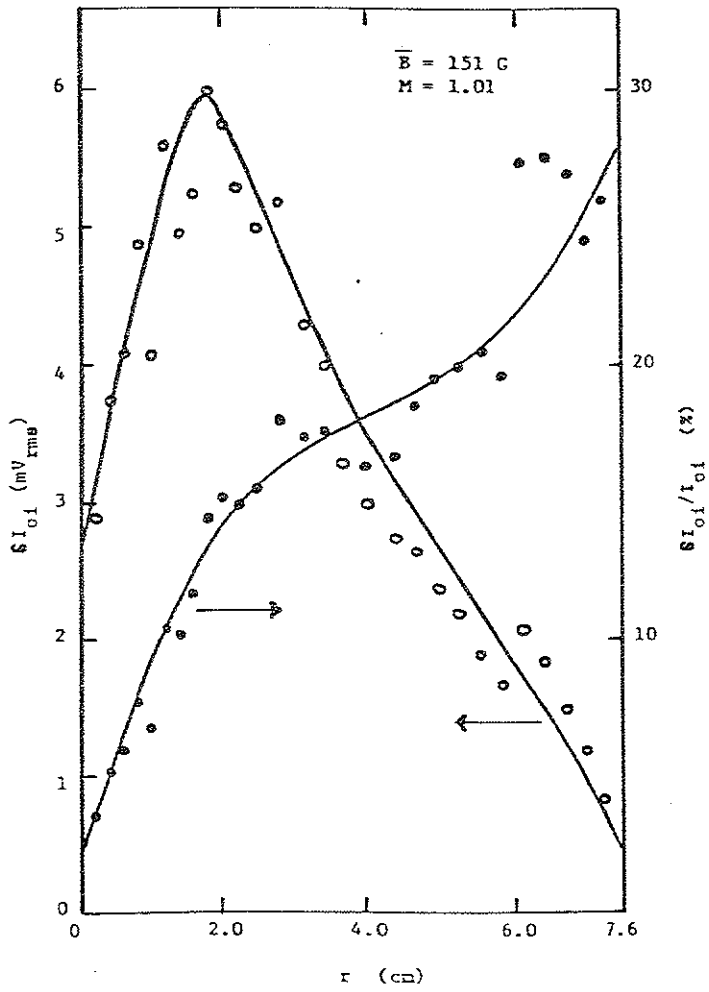

Fig. 6-8. Profiles of the fluctuation levels of both drift waves for parameters corresponding to point B of Fig. 6-6.

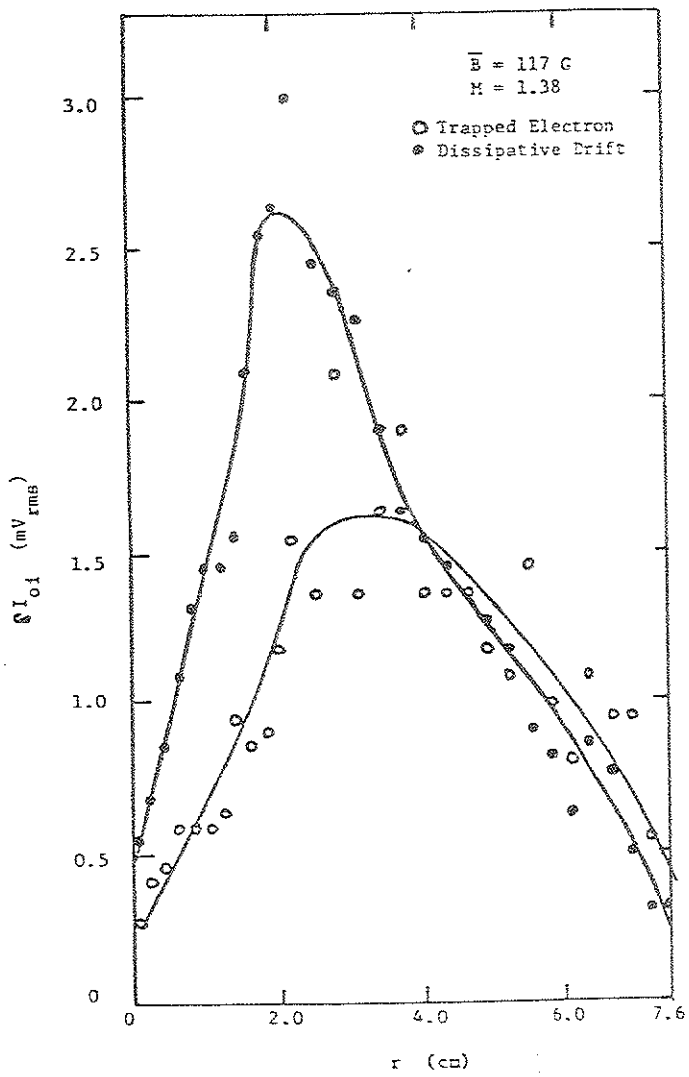

modes. As one now proceeds from B to C (changing the magnetic field strength while holding the mirror ratio constant) the frequencies coalesce. The fluctuation profile at point C is shown in Fig. 6-9. Finally, as one moves from C to D in Fig. 6-6 the frequencies again become distinct, but in addition, the magnitude of the low frequency mode rapidly increases. Figure 6-10 shows the relative amplitudes of all three modes versus radius at point D. The above phenomena is not confined to the particular value of mirror ratio for which the data is shown. Similar behaviour is observed at other mirror ratios as long as the amplitude of the trapped electron instability is sufficiently large (i.e. the mirror ratio is not too small). This is demonstrated in Fig. 6-6 which also shows the locus of points of coalescence in $\bar{B}$ - M space.

Attention will now be focused on Figs. 6-8, 6-9, and 6-10. In Fig. 6-8 the radial fluctuation profiles of the two drift modes are seen to be distinct. The dissipative drift wave's fluctuation level peaks near r = 2.0 cm while that of the trapped electron mode has a broader radial structure and peaks near r = 4.0 cm. At coalescence, shown in Fig. 6-9, only a peak at r = 3.0 cm is observed. In Fig. 6-10 it is seen that the two drift wave possess a similar radial structure and amplitude all the way across the plasma column. There are no clear peaks, the profiles being broad and flat and of a much smaller amplitude than previous to coalescence. It is in this last situation that the low frequency mode arises. It is concluded that the low frequency mode is in some way associated with a coupling of

Fig. 6-9. Profiles of the fluctuation level and fluctuation level normalized to the ion saturation current for parameters corresponding to point C of Fig. 6-6 (coalescence).

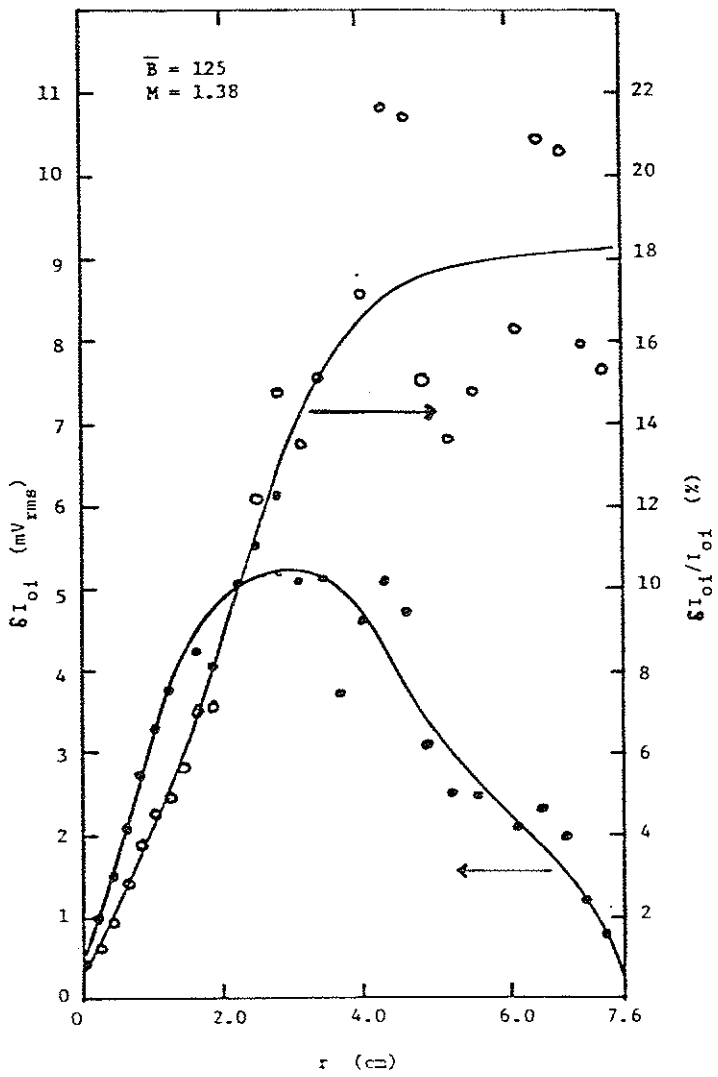

Fig. 6-10. Radial profiles of the fluctuation level of both drift waves together with that of the low frequency mode for parameters corresponding to point D of Fig.6-6. The amplitude and radial structure of the two drift waves is nearly identical. The amplitude of the low frequency mode is very large.

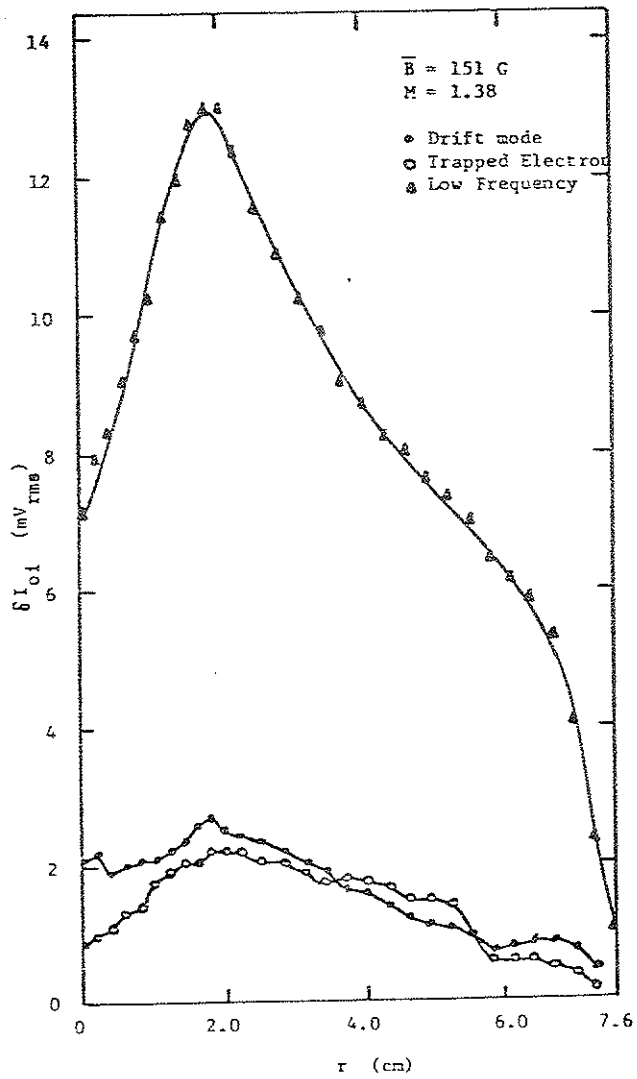

the two drift waves. It is not clear whether the overlapping of the radial profiles is a condition necessary to produce the low frequency mode or is a consequence of the presence of the low frequency mode.

Figure 6-11 shows a sequence of frequency spectrums taken at different magnetic field strengths with the mirror ratio held fixed at M = 1.38. The second, third, and forth spectrums correspond to points B, C, and D respectively of Fig. 6-6. Beginning at the left of Fig. 6-11 one sees that as the magnetic field strength is increased the two peaks approach one another and increase in amplitude until at $\bar{B}$ = 131 G they merge to form one amplitude peak. Beyond the coalescence the two modes again become distinct and the low frequency mode (not shown) sets in. At still higher magnetic field strengths the individual character of the two drift waves is washed out into one continuous broad frequency peak which decreases in amplitude.

The temperature and density profiles corresponding to the parameters of points A and D of Fig. 6-6 are shown in Figs. 6-12 and 6-13 respectively. Comparing them one sees that both the temperature and density are lower at the higher mirror ratio. The temperature profiles are very similar in shape whereas the density profiles are quite different. The M = 1.38 density profile is much broader than at uniform field. This broadening might be due to the low frequency mode causing enhanced radial transport.

Fig. 6-11. Sequence of frequency spectrums showing the fluctuation amplitude of the two drift waves as the magnetic field strength is varied at constant mirror ratio. The middle three spectrums correspond to points B, C, and D of Fig. 6-6.

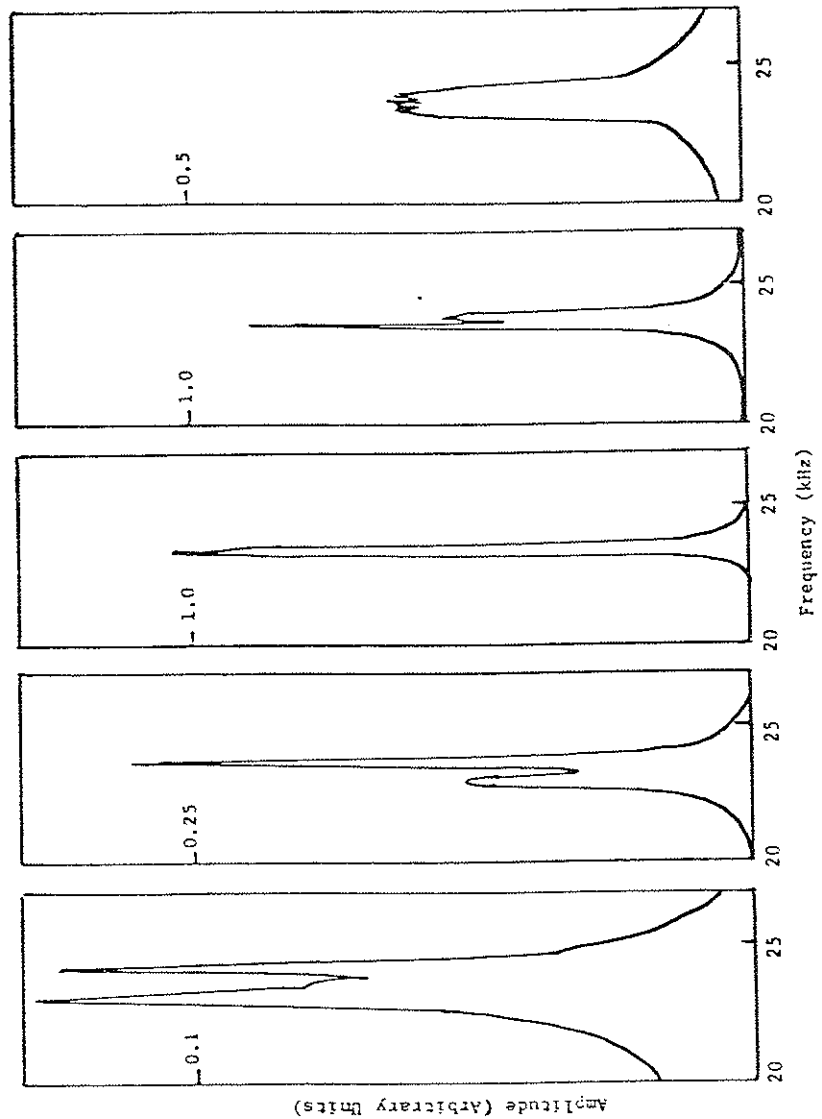

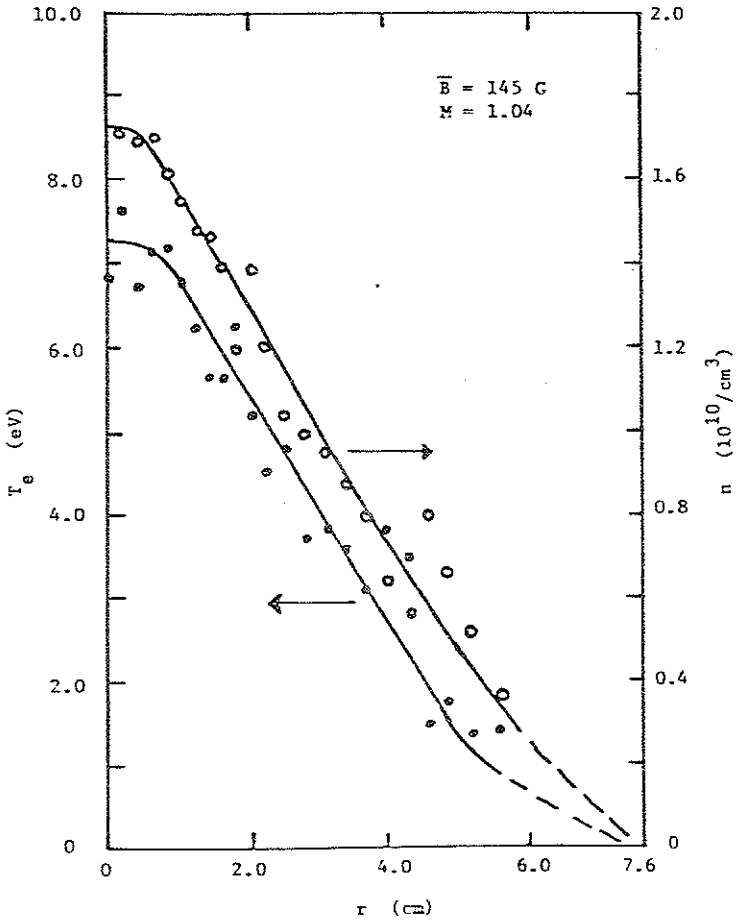

Fig. 6-12. Radial profiles of temperature and density when the plasma is unstable to only the dissipative drift wave (point A of Fig. 6-6).

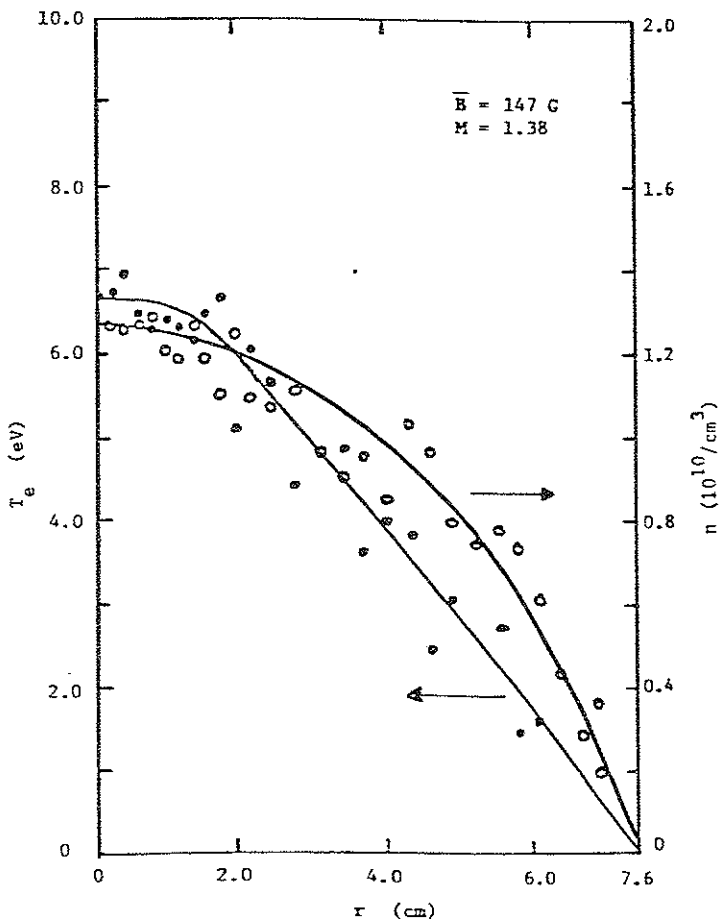

Fig. 6-13. Radial profiles of temperature and density when the plasma is unstable to all three modes (point D of Fig. 6-6). The density is both smaller in magnitude and broader in space than that shown in Fig. 6-12.

C. Conclusions

It seems unlikely that the low frequency mode can be attributed to anything but the coalescence of the two drift waves. First of all it would mean that its appearence upon the coalescence of the two drift waves is merely coincidental which does not appear reasonable at all. Second, a reason for its appearence must be given. The only other time flute modes are observed in the Linear Multiple Mirror is when an interchange mode is driven unstable due to excessive bad curvature (large mirror ratio). That the above flute mode falls into this category can be dismissed on three counts. The first is that the observed frequency (< 1 kHz) is too low in comparison to either the diamagnetic frequency (~ 50 kHz) or the magnetic curvature drift frequency (~ 5 kHz). The second is that as the mirror ratio is increased to higher values or as the magnetic field is raised the amplitude of the low frequency mode diminishes or disappears altogether. This is not typical of an interchange mode. The third is that the flute mode appears at very small values of the mirror ratio which are insufficient to drive an interchange mode unstable.

Many interesting questions are raised by the above observations. For instance, why does the low frequency mode only appear above a certain magnetic field strength? This and other questions can only be answered with both a very detailed understanding of the drift waves involved as well as with a complete nonlinear model of the interaction of drift waves. Interestingly,

the low frequency mode does not occur at the difference frequency of the two drift waves. Rather its frequency is nearly constant as a function of the magnetic field strength which might imply that it is a usually stable normal mode of the plasma which is driven unstable when two modes are close enough together in frequency. This would then make the present low frequency mode the same as the one observed by Grubb[1] but driven by a different mechanism.

References

1. D.P. Grubb and G.A. Emmert, Phys. Fluids 22, 1825 (1979).

2. D.P. Grubb and G.A. Emmert, Phys. Fluids 22, 770 (1979).

3. R.K. Richards and G.A. Emmert, Nucl. Fusion 17, 205 (1977).

4. D.P. Grubb and G.A. Emmert, Nucl. Fusion 18, 977 (1978).

APPENDIX

Chapter IV made reference to the numerical solution of Eqn. (4.43). The following is a description of the computer program used to generate the solutions and a listing of the program itself.

The program begins by accepting the 15 experimental inputs necessary to compute the quantities listed in Table 4-1. These are T_e, T_i, L_n, L_T, $k_\perp$, $k_\parallel$, B, n, A_{ion} (ion atomic number), $\langle\sigma v\rangle_{en}^{Neon}$ (average-electron neutral collision rate for neon), v_E (ExB drift velocity), n_{Bessel} (index for the Bessel function sum), M, P_n (neutral pressure), and L_C (mirror cell length). Since many of these quantities never change (for instance L_C) all of them are defaulted to typical values at the start of the program. Any, none, or all can be changed at each loop through the program.

In order to investigate the effect of different terms in the dispersion relation (in particular collisions) a number of flags were defined which enable or disable particular terms in the dispersion relation. Any, all, or none of the flags can be changed at each loop through the program.

Once the inputs have been entered a choice is made between finding a single root at one set of parameters, or solving the dispersion relation functionally (for instance finding a root as a function of the magnetic field strength). The single point mode is useful for just finding roots in the complex ω-plane. Once one or

more roots have been found they serve as an initialization data for the functional mode.

In the single point mode a call is first made to PARAMS which computes parameters (such as Ω_e, Ω_i, ...) for the current set of experimental values. Next a call to ROOTFIND is made. This is a subprogram that uses a secant method in the complex plane to iteratively find a root to the dispersion relation.

To find a root it is necessary to know the function for which one is trying to compute the root. The function, which in this case is the dispersion relation, is contained in the subprogram TE_DISPER. In order to evaluate the dispersion relation at a particular value of ω, the complex frequency, a number of special functions are required. The subprogram ZFUNC evaluates the plasma dispersion function. BESMOD computes the S_n functions for index up to $n_{Bessel} = 5$ by means of analytic approximations to the first two modified Bessel functions, I_o and I_1, and through a recursion formula for higher order functions. In addition, the Maxwellian average for the trapped electron term must be computed. This is done by MAXAVE which uses a Gaussian quadrature formula rather than a Simpson rule type evaluation of the integral. This is done for sake of numerical efficiency. The quadrature formula requires 10 function evaluations whereas the Simpson rule requires at least 100 function evaluations to compute the integral to the same accuracy. Since MAXAVE is called once at each iteration of ROOTFIND, efficiency at the inner nest containing MAXAVE is important.

At the onset it was not known whether the velocity dependent electron-neutral collision cross section was important with respect to stability or not. To answer this question the velocity dependence of the collision frequency was explicitly taken into account through the subprogram NEON which contains a table of the electron-neutral cross section as a function of energy. At each function evaluation in MAXAVE, NEON is called. Additionally, MAXAVE accounts for the velocity dependence of the curvature drift.

To compute the roots functionally all that is needed in addition to the programs listed above is a routine to increment the variable. This is done by the program VARYPARAM which allows the choice of varying the mirror ratio, the magnetic field strength, of the neutral pressure. The routine requires an initial guess (found by use of the single point mode). If the variable step is kept small enough the previously found root is sufficient for an initial guess after the parameter is incremented.

The last few subroutines are concerned with ouputting data generated by the program. PRINTALL lists the current value of all inputs, flags, and parameters. PLOTO allows the plotting of graphs (generated from the functional mode) on Tektronix 4000 series terminals. This requires linking the main program to the Plot-10 software library available of the VAX computer. DUMP creates a data file from functionally generated roots. This is useful in conjunction with the TOPDRAWER plot generating software package also available on the VAX. TOPDRAWER is a very flexible package written

by physicists (at SLAC) for use by physicists to plot things physicists like to see plotted. With TOPDRAWER it is possible with a simple set of comands to plot experimental data (with error bars), theory curves from data files, text (both Latin and Greek characters), and comes complete with a set of special scientific symbols.

A listing of the Fortran program follows.


```
      IMPLICIT INTEGER (I-N)
      IMPLICIT DOUBLE PRECISION (A-H,O-Z)
      INTEGER STARTFLAG,FLAGFLAG,FLAG,FLAGRESET
      COMPLEX OMEGA,ZERO
      REAL RANGE,FREQ,GROWTH
      DIMENSION EX(15),FLAG(8),RANGE(4),FREQ(402),GROWTH(402)
      COMMON /E_AND_F/ EX,FLAG
      COMMON /DISPARAMS/ BION,CYCE,CYCI,EPSILON,ETA,GNU_EC,GNU_EE,
     1 GNU_EI,GNU_EN,GNU_ET,GNU_II,TAU,VTHE,VTHI,WDE,WDET,WDET1,WDET2,
     2 WDEC,WDI
      COMMON /VARIER/ RANGE,FREQ,GROWTH
      DATA EX/6.0D0,0.1D0,-1.0D0,-1.25D0,1.0D0,0.03D0,100.0D0,5.0D10,
     1        20.0D0,5.4D-08,0.0D0,1:0D0,1.11D0,1.0D-04,35.0D0/
      DATA FLAG/1,1,1,1,1,1,1,1/
      TYPE *, ' DEFAULT INPUTS (= 0) OR NEW INPUTS (= 1)?'
      ACCEPT *, IDEFAULT
      IF (IDEFAULT.EQ.1) THEN
      GOTO 45
      ELSE
      STARTFLAG = 1
      FLAGFLAG = 1
      GOTO 20
      END IF
   45 STARTFLAG = 0
      FLAGFLAG = 0
    1 TYPE *, ' ELECTRON TEMPERATURE:'
      ACCEPT *, EX(1)
      IF (STARTFLAG.NE.0) GOTO 20
    2 TYPE *, ' ION TEMPERATURE:'
      ACCEPT *, EX(2)
      IF (STARTFLAG.NE.0) GOTO 20
    3 TYPE *, ' DENSITY SCALE LENGTH:'
      ACCEPT *, EX(3)
      IF (STARTFLAG.NE.0) GOTO 20
    4 TYPE *, ' TEMPERATURE SCALE LENGTH:'
      ACCEPT *, EX(4)
      IF (STARTFLAG.NE.0) GOTO 20
    5 TYPE *, ' PERPENDICULAR WAVENUMBER:'
      ACCEPT *, EX(5)
      IF (STARTFLAG.NE.0) GOTO 20
    6 TYPE *, ' PARALLEL WAVENUMBER:'
      ACCEPT *, EX(6)
      IF (STARTFLAG.NE.0) GOTO 20
    7 TYPE *, ' MAGNETIC FIELD STRENGTH:'
      ACCEPT *, EX(7)
      IF (STARTFLAG.NE.0) GOTO 20
    8 TYPE *, ' PLASMA DENSITY:'
      ACCEPT *, EX(8)
      IF (STARTFLAG.NE.0) GOTO 20
    9 TYPE *, ' ION ATOMIC NUMBER:'
```

```
      ACCEPT *, EX(9)
      IF (STARTFLAG.NE.0) GOTO 20
10    TYPE *, ' AVERAGE ELECTRON NEUTRAL COLLISION RATE:'
      ACCEPT *, EX(10)
      IF (STARTFLAG.NE.0) GOTO 20
11    TYPE *, ' E X B DRIFT VELOCITY:'
      ACCEPT *, EX(11)
      IF (STARTFLAG.NE.0) GOTO 20
12    TYPE *, ' INDEX FOR ION BESSEL FUNCTION SUM:'
      ACCEPT *, EX(12)
      IF (STARTFLAG.NE.0) GOTO 20
13    TYPE *, ' MIRROR RATIO:'
      ACCEPT *, EX(13)
      IF (STARTFLAG.NE.0) GOTO 20
14    TYPE *, ' NEUTRAL PRESSURE:'
      ACCEPT *, EX(14)
      IF (STARTFLAG.NE.0) GOTO 20
15    TYPE *, ' MIRROR CELL LENGTH:'
      ACCEPT *, EX(15)
      IF (STARTFLAG.NE.0) GOTO 20
20    STARTFLAG = 1
      TYPE *, ' CHANGE A PARAMETER? (0 = NO, 1-15 = PARAMETER TO CHANGE)'
      ACCEPT *, IPARAM
      GOTO (49,1,2,3,4,5,6,7,8,9,10,11,12,13,14,15) IPARAM+1
49    IF (FLAGFLAG.EQ.1) GOTO 50
31    TYPE *, ' ION COLLISIONS ON (1) OR OFF (0)?'
      ACCEPT *, FLAG(1)
      IF (FLAGFLAG.NE.0) GOTO 50
32    TYPE *, ' CIRCULATING ELECTRON COLLISIONS ON (1) OR OFF (0)?'
      ACCEPT *, FLAG(2)
      IF (FLAGFLAG.NE.0) GOTO 50
33    TYPE *, ' TRAPPED ELCTRON-NEUTRAL COLLISIONS ON (1) OR OFF (0)?'
      ACCEPT *, FLAG(3)
      IF (FLAGFLAG.NE.0) GOTO 50
34    TYPE *, ' TRAPPED ELEC. COULOMB COLLISIONS ON (1) OR OFF (0)?'
      ACCEPT *, FLAG(4)
      IF (FLAGFLAG.NE.0) GOTO 50
35    TYPE *, ' DENSITY CONSERVING COLLISION TERMS ON (1) OR OFF (0)?'
      ACCEPT *, FLAG(5)
      IF (FLAGFLAG.NE.0) GOTO 50
36    TYPE *, ' TRAPPED ELECTRON CURVATURE DRIFT ON (1) OR OFF (0)?'
      ACCEPT *, FLAG(6)
      IF (FLAGFLAG.NE.0) GOTO 50
37    TYPE *, ' TRAPPED ELEC. DENSITY CONS. TERMS ON (1) OR OFF (0)?'
      ACCEPT *, FLAG(7)
      IF (FLAGFLAG.NE.0) GOTO 50
38    TYPE*, ' TRAPPED ELECTRONS ON (1) OR OFF (0)?'
      ACCEPT *, FLAG(8)
      IF (FLAGFLAG.NE.0) GOTO 50
50    FLAGFLAG = 1
```



```
      DO 51 I = 1,8
      IF ((FLAG(I).EQ.0).OR.(FLAG(I).EQ.1)) GOTO 51
      FLAG(I) = 1
51    CONTINUE
      TYPE *, ' RESET ANY FLAG? (0 = NO, 1-8 FOR FLAG TO RESET)'
      ACCEPT *, FLAGRESET
      GOTO (30,31,32,33,34,35,36,37,38) FLAGRESET+1
30    TYPE *, ' SOLVE DISP. REL. ONCE (= 0) OR FUNCTIONALLY (= 1)?'
      ACCEPT *, IMODE
      ERR = 1.0D-03
      IF (IMODE.EQ.1) GOTO 60
      TYPE *, ' ENTER RE AND IM PARTS OF INITIAL GUESS FOR ROOT:'
      ACCEPT *, OMRE,OMIM
      OMEGA = CMPLX(OMRE,OMIM)
      CALL PARAMS
      CALL ROOTFIND(OMEGA,ERR,IMODE,ZERO)
      TYPE *, ' THE ROOT IS:',ZERO
      CALL PRINTALL
67    TYPE *, ' ANOTHER CASE? (0 = NO, 1 = YES)'
      ACCEPT *, ICASE
      IF (ICASE.EQ.0) GOTO 100
      GOTO 20
60    TYPE *, ' SOLVE DISPERSION RELATION AS A FUNCTION OF:'
      TYPE *, '     1. MAGNETIC FIELD'
      TYPE *, '     2. NEUTRAL PRESSURE'
      TYPE *, '     3. MIRROR RATIO'
      ACCEPT *, IFUNC
      IF (IFUNC.EQ.1) THEN
      NVARY = 7
      ELSE IF (IFUNC.EQ.2) THEN
      NVARY = 14
      ELSE
      NVARY = 13
      END IF
      CALL VARY_PARAM(NVARY,IMODE)
      CALL PRINTALL
      TYPE *, ' PLOT RESULTS? (0 = NO, 1 = YES)'
      ACCEPT *, IPLOT
      IF (IPLOT.NE.1) GOTO 66
65    CALL PLOTO(RANGE,FREQ)
      CALL PLOTO(RANGE,GROWTH)
      TYPE *, ' REPLOT? (0 = NO, 1 = YES)'
      ACCEPT *, IREPLOT
      IF (IREPLOT.EQ.1) GOTO 65
66    TYPE *, ' SAVE FOR TOPDRAWER PLOTTING? (0 = NO, 1 = YES)'
      ACCEPT *, ITD
      IF (ITD.EQ.0) GOTO 67
      CALL DUMP
      GOTO 67
100   END
```

```
      SUBROUTINE PARAMS
      IMPLICIT INTEGER (I-N)
      IMPLICIT DOUBLE PRECISION (A-H,O-Z)
      INTEGER FLAG
      DIMENSION EX(15),FLAG(8)
      COMMON /DISPARAMS/ BION,CYCE,CYCI,EPSILON,ETA,GNU_EC,GNU_EE,
     1 GNU_EI,GNU_EN,GNU_ET,GNU_II,TAU,VTHE,VTHI,WDE,WDET,WDET1,WDET2,
     2 WDEC,WDI
      COMMON /E_AND_F/ EX,FLAG
      COMMON /MAX_NUMS/ H2,H3,H4,H5,WW,ETA1
      EPSILON = (EX(13)-0.99999999D0)/(EX(13)+1.0D0)
      BION = 1.0454D4*EX(2)*EX(9)*(EX(5)/EX(7))**2.0D0
      WDE = -1.0D08*EX(5)*EX(1)/(EX(7)*EX(3))
      TAU = EX(1)/EX(2)
      VTHI = 1.385D06*SQRT(EX(2)/EX(9))
      VTHE = 5.935D07*SQRT(EX(1))
      CYCE = 1.7575D07*EX(7)
      CYCI = 9.5727D03*EX(7)/EX(9)
      DEN_NEU = 3.218D16*EX(14)
      GNU_EN = DEN_NEU*EX(10)
      COULGI = 23.1D0+0.5D0*LOG(EX(2)**3.0D0/EX(8))
      COULGE = 23.1D0+0.5D0*LOG(EX(1)**3.0D0/EX(8))
      GNU_EI = 1.713D-06*EX(8)*COULGI/(EX(1)**1.5D0)
      GNU_EE = 3.005D-06*EX(8)*COULGE/(EX(1)**1.5D0)
      GNU_II = 7.014D-08*EX(8)*COULGI/(EX(2)*SQRT(EX(2)*EX(9)))
      GNU_EC = GNU_EN+GNU_EE+GNU_EI
      GNU_ET = GNU_EN+(GNU_EE+GNU_EI)/(2.0D0*EPSILON)
      ETA = EX(3)/EX(4)
      ETA1 = ETA
      WDET = WDE*(1.0D0-ETA/2.0D0)
      WDI = EX(5)*EX(11)
      WDEC = WDI
      WDET1 = WDI
      WDET2 = 3.1415926535D0*EPSILON*EX(5)*VTHE*VTHE/(CYCE*EX(15))
      H2 = WDET1/WDE
      H3 = WDET2/WDE
      H4 = 0.323D-16*DEN_NEU*VTHE/WDE
      H5 = (GNU_EE+GNU_EI)/(2.0D0*EPSILON*WDE)
      WW = WDE
      RETURN
      END



      SUBROUTINE ROOTFIND(GUESS,ERROR,MODE,ROOT)
      IMPLICIT INTEGER (I-N)
      IMPLICIT DOUBLE PRECISION (A-H,O-Z)
      INTEGER FLAG
      COMPLEX GUESS,ROOT,G1,G2,D1,D2,GTEMP
      DIMENSION EX(15),FLAG(8)
```



```
      COMMON /E_AND_F/ EX,FLAG
      CALL TE_DISPER(GUESS,D1)
      G1 = GUESS
      G2 = 1.05D0*GUESS
3     DO 1 NLOOP = 1,20
      CALL TE_DISPER(G2,D2)
      IF ((ABS(1.0D0-G2/G1)).LE.ERROR) GOTO 2
      GTEMP = G2
      IF (MODE.EQ.1) GOTO 5
      TYPE *, G2,D2
5     G2 = (G1*D2-G2*D1)/(D2-D1)
      G1 = GTEMP
1     D1 = D2
      TYPE *, ' DID NOT CONVERGED.'
      IF (MODE.EQ.1) GOTO 4
      TYPE *, ' MORE ITERATIONS? (0 = NO, 1 = YES)'
      ACCEPT *, IREIT
      IF (IREIT.EQ.1) GOTO 3
2     IF (MODE.EQ.1) GOTO 4
      TYPE *, ' ERROR =',ERROR,' CHANGE ERROR? (0 = NO, 1 = YES)'
      ACCEPT *, I_CHG_ERR
      IF (I_CHG_ERR.NE.1) GOTO 4
      TYPE *, ' ENTER NEW ERROR'
      ACCEPT *, ERROR
      GOTO 3
4     ROOT = G2
      RETURN
      END



      SUBROUTINE TE_DISPER(OM,DEE)
      IMPLICIT INTEGER (I-N)
      IMPLICIT DOUBLE PRECISION (A-H,O-Z)
      INTEGER FLAG
      COMPLEX OM,DEE,UNIT,C13,C14,C16,C19,C20,C21,ZE,ZEDER,ZI,ZIDER,
     1 CET,TET,IT,AVE1,AVE2,SUM
      DIMENSION EX(15),FLAG(8),SI(0:5)
      COMMON /DISPARAMS/ BION,CYCE,CYCI,EPSILON,ETA,GNU_EC,GNU_EE,
     1 GNU_EI,GNU_EN,GNU_ET,GNU_II,TAU,VTHE,VTHI,WDE,WDET,WDET1,WDET2,
     2 WDEC,WDI
      COMMON /E_AND_F/ EX,FLAG
      UNIT = CMPLX(0.0D0,1.0D0)
      C12 = EX(6)*VTHE
      C13 = UNIT*FLAG(2)*GNU_EC/C12
      C14 = C13+(OM-WDEC)/C12
      C15 = ETA*WDE/(2.0D0*C12)
      C16 = C13*FLAG(5)+(OM-WDET)/C12
      CALL ZFUNC(C14,ZE,ZEDER)
      C17 = FLAG(8)*SQRT(2.0D0*EPSILON)
```

```
      CET = (1.0D0-C17)*(1.0D0+C16*ZE+C15*C14*ZEDER)
      CET = CET/(1.0D0+C13*FLAG(5)*ZE)
      CALL MAXAVE(OM,AVE1,AVE2)
      TET = C17*(1.0D0-AVE1)/(1.0D0-AVE2)
      NBES = EX(12)
      SUM = 0.0D0
      NZEE = 2*NBES+1
      C18 = EX(6)*VTHI
      C19 = UNIT*FLAG(1)*GNU_II/C18
      C20 = C19*FLAG(5)+(OM+WDE/TAU)/C18
      C21 = C19+(OM-WDI-EX(12)*CYCI)/C18
      C22 = CYCI/C18
      CALL BESMOD(BION,SI)
      ND = NBES+1
      DO 2 NN = 1,NZEE
      CALL ZFUNC(C21,ZI,ZIDER)
      SUM = SUM+SI(ABS(ND-NN))*ZI
    2 C21 = C21+C22
      IT = TAU*(1.0D0+C20*SUM)/(1.0D0+C19*FLAG(5)*SUM)
      DEE = IT+TET+CET
      RETURN
      END



      SUBROUTINE MAXAVE(OME,AV1,AV2)
      IMPLICIT INTEGER (I-N)
      IMPLICIT DOUBLE PRECISION (A-H,O-Z)
      INTEGER FLAG
      COMPLEX OME,AV1,AV2,AV11,DEN,TOP1,W1,H1,H6,UNIT
      DIMENSION X(10),W(10),EX(15),FLAG(8)
      COMMON /MAX_NUMS/ H2,H3,H4,H5,WW,ETA1
      COMMON /E_AND_F/ EX,FLAG
      DATA X/ 0.13779347054ODO, 0.72945454950 3DO, 1.808342901740DO,
     1         3.401433697855DO, 5.552496140064DO, 8.3301527467 64DO,
     2        11.84378583790 0DO,16.279257831378DO,21.996585811981DO,
     3        29.920697012274DO/
      DATA W/ 3.08441115765D-01,4.01119929155D-01,2.18068287612D-01,
     1         6.20874560987D-02,9.50151697518D-03,7.53008388588D-04,
     2         2.82592334960D-05,4.24931398496D-07,1.83956482398D-09,
     3         9.91182721961D-13/
      AL = 1.12837916709551 2DO
      UNIT = CMPLX(0.0D0,1.0D0)
      H1 = OME/WW
      NLAST = 1
      SIG = 1.0D0
      AV11 = 0.0D0
      AV2 = 0.0D0
      DO 1 III = 1,10
      S = X(III)
```



```
      SS = SQRT(S)
      IF (FLAG(3).EQ.0) GOTO 2
      CALL NEON(S,NLAST,SIG,NL)
      NLAST = NL
    2 H6 = UNIT*((FLAG(3)*H4*SIG)+FLAG(4)*H5/(S*S))*SS
      DEN = H1-H2-S*H3*FLAG(6)+H6
      TOP1 = H1-1.0D0-ETA1*(S-1.5D0)
      W1 = SS*W(III)/DEN
      AV2 = AV2+H6*W1
    1 AV11 = AV11+TOP1*W1
      AV2 = AL*FLAG(5)*FLAG(7)*AV2
      AV1 = AV2+AV11*AL
      RETURN
      END



      SUBROUTINE NEON(EN,NOLD,SIGMA,NEW)
      IMPLICIT INTEGER (I-N)
      IMPLICIT DOUBLE PRECISION (A-H,O-Z)
      INTEGER FLAG
      DIMENSION EX(15),FLAG(8),ENTBL(25),CRSSEC(25)
      COMMON /E_AND_F/ EX,FLAG
      DATA ENTBL/3.0D0,4.0D0,  6.0D0,  8.0D0, 10.0D0, 12.0D0,  14.0D0,
     1            16.0D0, 18.0D0, 20.0D0, 30.0D0, 40.0D0,  50.0D0,
     2            60.0D0, 70.0D0, 80.0D0, 90.0D0,100.0D0, 150.0D0,
     3           200.0D0,300.0D0,400.0D0,500.0D0,700.0D0,1000.0D0/
      DATA CRSSEC/2.30D0,2.56D0,2.88D0,3.16D0,3.33D0,3.45D0,3.55D0,
     1            3.60D0,3.62D0,3.63D0,3.56D0,3.56D0,3.74D0,
     2            3.73D0,3.69D0,3.62D0,3.54D0,3.44D0,2.73D0,
     3            2.35D0,1.95D0,1.63D0,1.41D0,1.14D0,0.87D0/
      EN = EN*EX(1)
      IF (EN.GT.3.0D0) GOTO 1
      SIGMA = 0.323D0+1.583D0*SQRT(EN)+0.0845D0*EN*LOG(EN)-0.346D0*EN
      SIGMA = SIGMA/0.323D0
      NEW = 1
      RETURN
    1 NTAB = 0
      DO 2 NA = NOLD,24
    2 IF ((ENTBL(NA).LT.EN).AND.(ENTBL(NA+1).GE.EN)) GOTO 3
    3 NEW = NA
      IF (NEW.EQ.1) THEN
      NTAB = 1
      ELSE IF (NEW.EQ.24) THEN
      NTAB = -1
      ELSE IF (NEW.EQ.25) THEN
      NTAB = -2
      END IF
      N1 = NEW+NTAB
      NO = N1-1
```

```
      N2 = N1+1
      N3 = N1+2
      X0 = EN-ENTBL(N0)
      X1 = EN-ENTBL(N1)
      X2 = EN-ENTBL(N2)
      X3 = EN-ENTBL(N3)
      X01 = X1-X0
      X02 = X2-X0
      X03 = X3-X0
      X12 = X2-X1
      X13 = X3-X1
      X23 = X3-X2
      Y0 =  X1*X2*X3/(X01*X02*X03)
      Y1 = -X2*X3*X0/(X12*X13*X01)
      Y2 =  X3*X0*X1/(X23*X02*X12)
      Y3 = -X0*X1*X2/(X03*X13*X23)
      SIGMA = Y0*CRSSEC(N0)+Y1*CRSSEC(N1)+Y2*CRSSEC(N2)+
     1Y3*CRSSEC(N3)
      SIGMA = SIGMA/0.323D0
      RETURN
      END



      SUBROUTINE VARY_PARAM(NIN,NMODE)
      IMPLICIT INTEGER (I-N)
      IMPLICIT DOUBLE PRECISION (A-H,O-Z)
      INTEGER FLAG
      COMPLEX OMEG,ANSER
      REAL RANGE,FREQ,GROWTH
      DIMENSION EX(15),FLAG(8),RANGE(4),FREQ(402),GROWTH(402)
      COMMON /E_AND_F/ EX,FLAG
      COMMON /VARIER/ RANGE,FREQ,GROWTH
      TWOPI = 6.28318530717958647692D0
      TYPE *, ' ENTER LOWER AND UPPER LIMITS ON VARIABLE:'
      ACCEPT *, VDN,VUP
      TYPE *, ' ENTER VARIABLE INCREMENT:'
      ACCEPT *, VINCR
      NOUT = 1+(VUP-VDN)/VINCR
      EX(NIN) = VDN
      TYPE *, ' ENTER RE AND IM PARTS OF INITIAL ROOT:'
      ACCEPT *, AAA,BBB
      OMEG = CMPLX(AAA,BBB)
      ERRO = 1.0D-03
      DO 88 IV = 2,NOUT+1
      CALL PARAMS
      CALL ROOTFIND(OMEG,ERRO,NMODE,ANSER)
      FREQ(IV)   = REAL(ANSER)/TWOPI
      GROWTH(IV) = AIMAG(ANSER)
      OMEG = ANSER
```



```
88    EX(NIN) = EX(NIN)+VINCR
      RANGE(1) = -1.0
      RANGE(2) = NOUT
      RANGE(3) = VDN
      RANGE(4) = VINCR
      FREQ(1) = NOUT
      GROWTH(1) = NOUT
      RETURN
      END



      SUBROUTINE BESMOD(FLR,ESS)
      IMPLICIT DOUBLE PRECISION (A-H,O-Z)
      IMPLICIT INTEGER (I-N)
      DIMENSION ESS(0:5),ESSP(0:5)
      IF (FLR.NE.0.0D0) GOTO 1
      DO 2 I = 0,5
2     ESS(I) = 0.0D0
      ESS(0) = 1.0D0
      RETURN
1     ESS(0) = BESMOD0(FLR)
      ESS(1) = BESMOD1(FLR)
      DO 3 N = 2,5
      ENN = N
3     ESS(N) = ESS(N-2)-2.0D0*(ENN-1.0D0)*ESS(N-1)/FLR
      RETURN
      END
      FUNCTION BESMOD0(FLR)
      IMPLICIT DOUBLE PRECISION (A-H,O-Z)
      IMPLICIT INTEGER (I-N)
      DIMENSION POLY1(7),POLY2(9)
      DATA POLY1/ .0045813D0, .0360768D0, .2659732D0,1.2067492D0,
     1            3.0899424D0,3.5156229D0,1.000000000/
      DATA POLY2/ .00392377D0,-.01647633D0, .02635537D0,
     1           -.02057706D0, .00916281D0,-.00157565D0,
     2            .00225319D0, .01328592D0, .39894228D0/
      T = FLR/3.75D0
      IF (T.GE.1.00D0) GOTO 1
      T2 = T*T
      BESMOD0 = POLY1(1)
      DO 2 I = 2,7
2     BESMOD0 = BESMOD0*T2+POLY1(I)
      BESMOD0 = BESMOD0*DEXP(-FLR)
      GOTO 3
1     TINV = 1.00D0/T
      BESMOD0 = POLY2(1)
      DO 4 J = 2,9
4     BESMOD0 = BESMOD0*TINV+POLY2(J)
      BESMOD0 = BESMOD0/DSQRT(FLR)
```

```
3     END
      FUNCTION BESMOD1(FLR)
      IMPLICIT DOUBLE PRECISION (A-H,O-Z)
      IMPLICIT INTEGER (I-N)
      DIMENSION POLY1(7),POLY2(9)
      DATA POLY1 /.00032411D0,.00301532D0,.02658733D0,
     1 .15084934D0,.51498869D0,.87890594D0,.50000000D0/
      DATA POLY2 /-.00420059D0, .01787654D0,-.02895312D0,
     1             .02282967D0,-.01031555D0, .00163801D0,
     2            -.00362018D0,-.03988024D0, .39894228D0/
      T = FLR/3.75D0
      IF (T.GE.1.0D0) GOTO 1
      T2 = T*T
      BESMOD1 = POLY1(1)
      DO 2 I = 2,7
2     BESMOD1 = BESMOD1*T2+POLY1(I)
      BESMOD1 = BESMOD1*DEXP(-FLR)*FLR
      GOTO 3
1     TINV = 1.0D0/T
      BESMOD1 = POLY2(1)
      DO 4 I = 2,9
4     BESMOD1 = BESMOD1*TINV+POLY2(I)
      BESMOD1 = BESMOD1/DSQRT(FLR)
3     END



      SUBROUTINE ZFUNC(ARG,ZEE,ZEEP)
      IMPLICIT DOUBLE PRECISION (A-H,O-Z)
      IMPLICIT INTEGER (I-N)
      DIMENSION ABSCIS(10),WEIGHT(10)
      COMPLEX ARG,ZEE,ZEEP,ARG1,UNIT,W,A2,A22,SUM,TERM,GAUSS,
     1 FNC1,FNC2
      DATA ABSCIS/      0.2453407083009D0,0.7374737285454D0,
     1 1.2340762153953D0,1.7385377121166D0,2.2549740020893D0,
     2 2.7888060584281D0,3.3478545673832D0,3.9447640401156D0,
     3 4.6036824495507D0,5.3874808900112D0/
      DATA WEIGHT/       4.622436696006D-01,2.866755053628D-01,
     1 1.090172060200D-01,2.481052088746D-02,3.243773342238D-03,
     2 2.283386360163D-04,7.802556478532D-06,1.086069370769D-07,
     3 4.399340992273D-10,2.229393645534D-13/
      ROOTPI = 1.772453850900
      PI = 3.14159265358979300
      UNIT = CMPLX(0.0D0,1.0D0)
      AR = ABS(REAL(ARG))
      AI = ABS(AIMAG(ARG))
      ARG1 = CMPLX(AR,AI)
      IF (((AR.GE.2.0D0).AND.(AR.LE.3.9D0)).AND.(AI.LE.3.0D-01))
     1 GOTO 12
      BOUND = (AR/2.6D0)**2.0D0+(AI/2.0D0)**2.0D0
```



```
      IF (BOUND.LE.1.0D0) GOTO 1
      IF ((AR.GE.3.9D0).OR.(AI.GE.3.0D0)) GOTO 2
      COEF = 13.5D0
      W = ARG1-14.0D0
      DO 3 K = 1,27
      W = ARG1-COEF/W
3     COEF = COEF-.5D0
      W = UNIT/(W*ROOTPI)
      GOTO 4
2     A2 = ARG1*ARG1
      W = .4613135D0/(A2-.1901635D0)
      W = W+.09999216D0/(A2-1.7844927D0)
      W = W+.002883894D0/(A2-5.5253437D0)
      W = W*UNIT*ARG1
      GOTO 4
12    GAUSS = 0.0D0
      DO 13 L = 1,10
      FNC1 = 1.0D0/(ARG1-ABSCIS(L))
      FNC2 = 1.0D0/(ARG1+ABSCIS(L))
13    GAUSS = GAUSS+WEIGHT(L)*(FNC1+FNC2)
      W = GAUSS*UNIT/PI
      GOTO 4
1     A2 = -ARG1*ARG1
      A22 = 2.0D0*A2
      SUM = CMPLX(1.0D0,0.0D0)
      TERM = CMPLX(1.0D0,0.0D0)
      DO 5 J = 1,30
      TERM = TERM*A22/(2.0D0*J+1.0D0)
      SUM = SUM+TERM
      TR = REAL(TERM)
      TI = AIMAG(TERM)
      TMOD = DSQRT(TR*TR+TI*TI)
      IF (TMOD.LE.1.0D-06) GOTO 6
5     CONTINUE
      PRINT 7
7     FORMAT (' SERIES FOR W NOT CONVERGENT')
6     SUM = 2.0D0*SUM*UNIT*ARG1/ROOTPI
      W = EXP(A2)+SUM
4     AQR = REAL(ARG)
      AQI = AIMAG(ARG)
      IF ((AQR.LE.0.0D0).AND.(AQI.GE.0.0D0)) GOTO 8
      IF ((AQR.LE.0.0D0).AND.(AQI.LE.0.0D0)) GOTO 9
      IF ((AQR.GE.0.0D0).AND.(AQI.LE.0.0D0)) GOTO 10
      GOTO 11
8     W = CONJG(W)
      GOTO 11
9     W = 2.0D0*EXP(-ARG1*ARG1)-W
      GOTO 11
10    W = CONJG(2.0D0*EXP(-ARG1*ARG1)-W)
11    ZEE = ROOTPI*UNIT*W
```

```
      ZEEP = -2.0D0*(1.0D0+ARG*ZEE)
      RETURN
      END



      SUBROUTINE DUMP
      IMPLICIT INTEGER (I-N)
      IMPLICIT REAL (A-H,O-Z)
      DIMENSION RANGE(4),FREQ(402),GROWTH(402)
      COMMON /VARIER/ RANGE,FREQ,GROWTH
      NDEL = RANGE(2)/25
      OPEN (UNIT=1,NAME='BIGDISP',TYPE='NEW',
     1  CARRIAGECONTROL='LIST')
      DO 77 LL = 2,RANGE(2)+1,NDEL
      A = RANGE(3)+(LL-2)*RANGE(4)
77    WRITE (1,51) A,FREQ(LL)
      DO 78 LM = 2,RANGE(2)+1,NDEL
      B = RANGE(3)+(LM-2)*RANGE(4)
78    WRITE (1,51) B,GROWTH(LM)
51    FORMAT (8F10.2)
      CLOSE (UNIT=1)
      END



      SUBROUTINE PLOTO(XD,YD)
      DIMENSION XD(4),YD(402)
      CALL INITT(480)
      CALL BINITT
      CALL CHECK(XD,YD)
      CALL DSPLAY(XD,YD)
      CALL TINPUT(I)
      RETURN
      END



      SUBROUTINE PRINTALL
      IMPLICIT INTEGER (I-N)
      IMPLICIT DOUBLE PRECISION (A-H,O-Z)
      INTEGER FLAG
      DIMENSION EX(15),FLAG(8)
      COMMON /E_AND_F/ EX,FLAG
      COMMON /DISPARAMS/ BION,CYCE,CYCI,EPSILON,ETA,GNU_EC,GNU_EE,
     1  GNU_EI,GNU_EN,GNU_ET,GNU_II,TAU,VTHE,VTHI,WDE,WDET,WDET1,WDET2,
     2  WDEC,WDI
      COMMON /MAX_NUMS/ H2,H3,H4,H5,WW,ETAI
      TYPE *, 'LIST INPUTS AND PARAMETERS? (0 = NO, 1= YES)'
      ACCEPT *, ILIST
```



```
      IF (ILIST.EQ.0) GOTO 99
      PRINT 1, (FLAG(J),J=1,8)
1     FORMAT (' FLAGS ARE:',10I2,/)
      PRINT 2, EX(1),EX(2),EX(3)
2     FORMAT (' OTHER INPUTS:',/,/,'  ELEC TEMP =',D11.3,
     1  '  ION TEMP  =',D11.3,'  DEN SCALE =',D11.3)
      PRINT 3, EX(4),EX(5),EX(6)
3     FORMAT ('  TMP SCALE =',D11.3,'  K PERP     =',D11.3,
     1  '  K PARALLE =',D11.3)
      PRINT 4, EX(7),EX(8),EX(9)
4     FORMAT ('  MAG FIELD =',D11.3,'  PLAS DENS =',D11.3,
     1  '  ION ATOM =',D11.3)
      PRINT 5, EX(10),EX(11),EX(12)
5     FORMAT ('  EN COL RT =',D11.3,'  VXB VELOC =',D11.3,
     1  '  N BESSEL  =',D11.3)
      PRINT 6, EX(13),EX(14),EX(15)
6     FORMAT ('  MIR RATIO =',D11.3,'  NEUT PRES =',D11.3,
     1  '  MIRR LNGT =',D11.3,/)
      PRINT 8, EPSILON,BION,WDE
8     FORMAT (' PARAMTERS:',/,/,'  EPSILON    =',D11.3,
     1  '  FLR PARAM ='D11.3,'  DIMG FREQ =',D11.3)
      PRINT 9, TAU,VTHE,VTHI
9     FORMAT ('  TAU        =',D11.3,'  E THM VEL =',D11.3,
     1  '  I THM VEL =',D11.3)
      PRINT 10, CYCE,CYCI
10    FORMAT ('  E CYC FRQ =',D11.3,'  I CYC FRQ =',D11.3)
      PRINT 11, GNU_EN,GNU_EI,GNU_EE
11    FORMAT ('  EN COL FQ =',D11.3,'  EI COL FQ =',D11.3,
     1  '  EE COL FQ =',D11.3)
      PRINT 12, GNU_II,GNU_EC,GNU_ET
12    FORMAT ('  II COL FQ =',D11.3,'  EC COL FQ =',D11.3,
     1  '  ET COL FQ =',D11.3)
      PRINT 13, ETA,WDET,WDI
13    FORMAT ('  ETA        =',D11.3,'  T DMG FRQ =',D11.3,
     1  '  I DRFT FQ =',D11.3)
      PRINT 14, WDEC,WDET1,WDET2
14    FORMAT ('  EC DFT FQ =',D11.3,'  ET DF FQ1 =',D11.3,
     1  '  ET DF FQ2 =',D11.3,/)
      PRINT 15, H2,H3,H4,H5
15    FORMAT (' NUMBERS LAST PASSED TO MAXAVE: H2, H3, H4, H5',/,/,
     1  4D11.3,/)
99    RETURN
      END
```